REPUBLIC OF TURKEY YILDIZ TECHNICAL UNIVERSITY GRADUATE SCHOOL OF NATURAL AND APPLIED SCIENCES

THE CORRELATIONS OF SPACE WEATHER AND SATELLITE ANOMALIES: RASAT

MEHMET KAPLAN

MSc. THESIS DEPARTMENT OF PHYSICS

ADVISER
ASSOC. PROF. MURAT HUDAVERDI

İSTANBUL, 2014

REPUBLIC OF TURKEY YILDIZ TECHNICAL UNIVERSITY GRADUATE SCHOOL OF NATURAL AND APPLIED SCIENCES

THE CORRELATIONS OF SPACE WEATHER AND SATELLITE ANOMALIES: RASAT

A thesis submitted by Mehmet KAPLAN in partial fulfillment of the requirements for the degree of **MASTER OF SCIENCE** is approved by the committee on 15.07.2014 in Department of Physics, Physics Program.

Thesis Adviser	
Assistant Prof. Dr. Murat Hudaverdi	
Yıldız Technical University	
Approved By the Examining Committee	
Assistant Prof. Dr. Murat Hudaverdi	
Yıldız Technical University	
Assoc. Prof. Dr. Taylan Yetkin	
Yıldız Technical University	
Prof. Dr. Ali Kaya	
Bogazici University	



ACKNOWLEDGEMENTS

I would like to express my deepest gratitude to my advisor, Dr. Murat Hudaverdi, for his excellent guidance, caring, patience, and providing me with an excellent atmosphere for doing this research, and for his financial support. I would like to thank Dr. Tulun Ergin, for prodiving me with RASAT data from TUBITAK, who also corrected my mistakes many times. I also would like to acknowledge TUBITAK UZAY for sharing the RASAT data. I would also like to thank my parents and my brother. They were always supporting me and encouraging me with their best wishes.

July, 2014 Mehmet KAPLAN

TABLE OF CONTENTS

P	age
LIST OF SYMBOLS	viii
LIST OF ABBREVIATIONS	ix
LIST OF FIGURES	X
LIST OF TABLES	xi
ABSTRACT	xiv
ÖZET	. xv
CHAPTER 1	
INTRODUCTION	1
1.1 Literature Review	4
WHAT IS SPACE WEATHER?	6
2.1 The Sun 2.1.1 The Solar Wind 2.1.2 Solar Flares 2.1.3 Coronal Mass Ejections 2.1.4 Solar Spots 2.2 Solar Energetic Particles 2.2.1 Solar Protons 2.2.2 Low Energetic Solar Electrons 2.2.3 High Enegetic Solar Electrons 2.3 Galactic Cosmic Rays	9 .13 .16 .22 .27 .31 .34 .36
2.4 Van Allen Radiation Belts	.41

CHAPTER 3

SPACE WI	EATHER INDEXES	44
3.1	Solar Radio Flux (SRF)	44
3.2	K Index	45
3.3	Dst Index	48
3.4	Geomagnetic Storms	49
3.5	Solar Radiation Storms	52
3.6	Radio Blackouts	54
CHAPTER	4	
EFFECTS (ON SPACECRAFTS & SATELLITES	56
4.1	Surface Charging	57
4.2	Deep Electric (Bulk Charging)	
4.3	Single Event Upset (SEU)	
4.4		
4.5	Solar Radio Frequency and Scintillations	
4.6	Background Noise in Sensors	
4.7	Spacecraft Orientation	
4.8	Faulty Hardware or Design	
4.9	•	
CHAPTER	5	
METHODS	S OF ANALYSES	66
F 1		
5.1	1 1 11	
5.2	1	68
CHAPTER	6	
TURKISH	REMOTE SENSING SATELLITE: RASAT	70
6.1	Technical Properties of RASAT	73
CHAPTER	7	
ANOMAL	IES OF RASAT	78
7.1	Anomalies of Rasat	79
	Incidents Dates Between the Years of 2011-2012	
7	.2.1 September 29 th - October 8 th , 2011	82
7	.2.2 November 29 th , 2011	89
7	.2.3 February 4 th , 2012	94
7	.2.4 July 12 th , 2012	98
7	.2.5 December 16 th , 2012	103
7.3	Incidents Dates Between the Years of 2013-2014	108
7	.3.1 June 3 rd , 2013	111
7	.3.2 July 9 th and July 10 th , 2013	114
	.3.3 July 25 th , 2013	

7.3.4	August 8 th , 2013	120
7.3.5	August 8 th , 2013 October 11 th , 2013	123
7.3.6	January 8 th , 2014	127
CHAPTER 8		
RESULTS ANI	DISCUSSION	131
REFERENCES		136
CURRICULUM	I VITAE	141

LIST OF SYMBOLS

Βφ

Magnetic Field Solar Radio Frequency Geomagnetic Storm Index F10.7 $\mathbf{K}_{\mathbf{p}}$

 A_p

Average of Kp Disturbance Storm Time Dst

LIST OF ABBREVIATIONS

В Boron Be Beryllium C Carbon CME **Coronal Mass Ejection EMIC** Electromagnetic Ion Cyclotron EP **Explosive Phase ESD** Electrostatic Discharge **EUV** Extreme Ultra Violet Fe GCR Galactic Cosmic Rays GEO Geosynchronous Orbit He Helium HEO High Earth Orbit HP Hot Phase HSS **High Speed Stream** Impulsive Phase IΡ LEO Low Earth Orbit LET Linear Energy Transfer Li Lithium NASA National Aeronautics and Space Administration NOAA The National Oceanic and Atmospheric Administration Oxygen O **PFU** Particle Flux Unit PH **Preheating Phase** SEP Solar Energetic Particles SEU Single Event Upset SF Solar Flare Si Silicon Solar Radio Frequency SRF

Solar Sector Boundary Crossing

Very Low Frequency

Al

ΑU

SSBC

VLF

Aluminium

Astronomical Unit

LIST OF FIGURES

		Page
Figure 2.1	Layers of The Sun	8
Figure 2.2	The Solar Wind Hitting the Earth's Magnetosphere	
Figure 2.3	A Coronal Mass Ejection Event	
Figure 2.4	Azimuthally-Symmetric Flux Rope Model	
Figure 2.5	Sun Spot Classification	
Figure 2.6	Early Work on Sunspots	
Figure 2.7	Solar Energetic Particle Mechanism	
Figure 2.8	Solar Energetic Protons	
Figure 2.9	A Schematic of How Relativistic Electron Paths	
Figure 2.10	Van Allen Radiation Belts	42
Figure 3.1	Dst Values Since the Year 1900	
Figure 3.2	Manetosphere in the Near-Earth Space Environment	
Figure 3.3	Space Weather Scales: Geomagnetic Storms	
Figure 3.4	Space Weather Scales: Solar Radiation Storms	
Figure 3.5	Space Weather Scales: Radio Blackouts	
Figure 4.1	Charge Control Mechanism for a Satellite	
Figure 6.1	Rasat is Ready for its Transportation to Russia	
Figure 6.2	Rasat is on Its Way for Launching	
Figure 6.3	Rasat is Being Tested by TUBITAK Scientists and Engineers	
Figure 6.4	Turkish Remote Sensing Satellite of RASAT	
Figure 6.5	An Image of Istanbul, Taken by RASAT	
Figure 7.1	Measured SEU Incidents in RASAT	
Figure 7.2	Sunspot Numbers vs Days	80
Figure 7.3	Radio Flux vs Days	81
Figure 7.4	A _p Values vs Days	81
Figure 7.5	Geosynchronius Satellite Environment	90
Figure 7.6	Goes 13 Proton flux	91
Figure 7.7	Geosynchronius Satellite Environment plot	95
Figure 7.8	Proton Flux	95
Figure 7.9	7-day Satellite Data	100
Figure 7.10	Proton Flux	100
Figure 7.11	7-day Satellite Data	104
Figure 7.12	Proton Flux	105
Figure 7.13	Measured SEU Incidents in RASAT	108
Figure 7.14	Measured SEU Incidents in RASAT	109
Figure 7.15	Sunspot Numbers vs Days	. 109
Figure 7.16	Radio Flux vs Days	. 110
Figure 7.17	A _p Values vs Days	. 110

LIST OF TABLES

		Page
Table 2.1	Solar-Wind Flux Densities near the Orbit of the Earth	10
Table 2.2	Some Derived Properties of the Solar Wind near the Orbit of Earth	12
Table 2.3	The Classification of the Solar Flares	15
Table 2.4	Low Energetic Solar Electron Events in an Active Year	34
Table 3.1	The Conversion Table for the Boulder Magnetometer	46
Table 3.2	K-index equivalent of a-index	47
Table 3.3	Average Kp to determine Geomagnetic Storm Level	48
Table 6.1	Technical Properties of Rasat	73
Table 6.2	Technical Properties of Rasat	74
Table 7.1	Radio Flux, Sunspot Numbers, Sunspot Area	84
Table 7.2	Proton Flux Values, Taken from NOAA	85
Table 7.3	Proton, Peak 5-minute-averaged fluxes Values at Spacecraft,	
	Generated by SPENVIS	86
Table 7.4	Electron Flux Values	
Table 7.5	Electron Flux Values at Spacecraft, Generated by SPENVIS	88
Table 7.6	Radio Flux, Sunspot Numbers, Sunspot Area	91
Table 7.7	Proton Flux Values	92
Table 7.8	Proton, Peak 5-minute-averaged fluxes Values at Spacecraft,	
	Generated by SPENVIS	92
Table 7.9	Electron Flux Values	93
Table 7.10	Electron Flux Values at Spacecraft, Generated by SPENVIS	93
Table 7.11	Radio Flux, Sunspot Numbers, Sunspot Area	96
Table 7.12	Proton Flux Values	96
Table 7.13	Proton, Peak 5-minute-averaged fluxes Values at Spacecraft,	
	Generated by SPENVIS	97
Table 7.14	Electron Flux Values	97
Table 7.15	Electron Flux Values at Spacecraft, Generated by SPENVIS	98
Table 7.16	Radio Flux, Sunspot Numbers, Sunspot Area	101
Table 7.17	Proton Flux Values	101
Table 7.18	Proton, Peak 5-minute-averaged fluxes Values at Spacecraft,	
	Generated by SPENVIS	102
Table 7.19	Electron Flux Values	
Table 7.20	Electron Flux Values at Spacecraft, Generated by SPENVIS	103
Table 7.21	Radio Flux, Sunspot Numbers, Sunspot Area	105

Table 7.22	Proton Flux Values	106
Table 7.23	Proton, Peak 5-minute-averaged fluxes Values at Spacecraft,	
	Generated by SPENVIS	106
Table 7.24	Electron Flux Values	107
Table 7.25	Electron Flux Values at Spacecraft, Generated by SPENVIS	107
Table 7.26	Radio Flux, Sunspot Numbers, Sunspot Area	112
Table 7.27	Proton Flux Values	
Table 7.28	Proton, Peak 5-minute-averaged fluxes Values at Spacecraft,	
	Generated by SPENVIS	113
Table 7.29	Electron Flux Values	
Table 7.30	Electron Flux Values at Spacecraft, Generated by SPENVIS	114
Table 7.31	Radio Flux, Sunspot Numbers, Sunspot Area	
Table 7.32	Proton Flux Values	
Table 7.33	Proton, Peak 5-minute-averaged fluxes Values at Spacecraft,	
	Generated by SPENVIS	116
Table 7.34	Electron Flux Values	116
Table 7.35	Electron Flux Values at Spacecraft, Generated by SPENVIS	117
Table 7.36	Radio Flux, Sunspot Numbers, Sunspot Area	
Table 7.37	Proton Flux Values	
Table 7.38	Proton, Peak 5-minute-averaged fluxes Values at Spacecraft,	
	Generated by SPENVIS	119
Table 7.39	Electron Flux Values	119
Table 7.40	Electron Flux Values at Spacecraft, Generated by SPENVIS	120
Table 7.41	Radio Flux, Sunspot Numbers, Sunspot Area	121
Table 7.42	Proton Flux Values	121
Table 7.43	Proton, Peak 5-minute-averaged fluxes Values at Spacecraft,	
	Generated by SPENVIS	122
Table 7.44	Electron Flux Values	122
Table 7.45	Electron Flux Values at Spacecraft, Generated by SPENVIS	123
Table 7.46	Radio Flux, Sunspot Numbers, Sunspot Area	124
Table 7.47	Proton Flux Values	125
Table 7.48	Proton, Peak 5-minute-averaged fluxes Values at Spacecraft,	
	Generated by SPENVIS	125
Table 7.49	Electron Flux Values	126
Table 7.50	Electron Flux Values at Spacecraft, Generated by SPENVIS	126
Table 7.51	Radio Flux, Sunspot Numbers, Sunspot Area	
Table 7.52	Proton Flux Values	

Table 7.53	Proton, Peak 5-minute-averaged fluxes Values at Spacecraft,	
	Generate by SPENVIS	129
Table 7.54	Electron Flux Values	129
Table 7.55	Electron Flux Values at Spacecraft, Generated by SPENVIS	130

THE CORRELATIONS OF SPACE WEATHER AND SATELLITE ANOMALIES: RASAT

Mehmet KAPLAN
Department of Physics
MSc. Thesis

Adviser: Assoc. Prof. Dr. Murat HUDAVERDI

The needs of modern human for remote sensing and information transfer have been increasing rapidly. To meet that, also the number of the modern spacecrafts has been increasing along with their capabilities and complexities. However as the capabilities of their electronics go up, the sensitivity to radiation effects also go up, which means the hardness of the electronics inside the spacecrafts decreases.

Space weather is a term which refers to the dynamic, highly variable conditions in near-Earth space and the space from the sun's atmosphere to the earth's. The quick changes in the magnetosphere, ionosphere and thermosphere affect the performance of the space electronics negatively and induce malfunctions.

In most cases the effects can be disregarded, but occasionally they can have severe results leading to data loss, communication breakdowns, system failure or in worse the total loss of satellite. Beside the fact that the ecomic impacts are crucial, They can be even life threatening for manned space missions. Therefore, space weather elements have to be properly identified in order to assign each possible system anomaly and accurate assessment of cause and effect.

The main focus of this work is to review documented operational anomalies for Turkish Remote Sensing Satellites of RASAT, by assessing the identification and estimation of potential source of space weather agents. So that more qualified, more secured, more resistant against space weather satellites will be able to be produced in the future.

Keywords: Space Weather, RASAT, Hidden Agents of the Space Weather	Satellite	Anomalies,	Solar	Energetic	Particles,
Tridden rigerits of the Space Weather					
	· ·	ILDIZ TEO	THNIC	TAT TIMIX	FRCITV
GRADUATE SCHOO					
				~~	. 323

UZAY HAVASI VE UYDU ANORMALLİKLER ARASI İLİŞKİLER RASAT

Mehmet KAPLAN

Fizik Anabilim Dalı Yüksek Lisans Tezi

Tez Danışmanı: Y. Doç. Dr. Murat HÜDAVERDİ

Uzay teknolojileri, modern hayatın iletişim, navigasyon ve veri transferine olan ihtiyaç artışından ötürü her geçen gün hızla gelişmektedir. Buna bağlı olarak uydu içi elektronik bileşenleri, bu ihtiyaçları karşılamak adına daha hızlı ve daha kompleks hale gelmektedirler. Bunun sonucunda bu bileşenlerin kapasitelerinin ve uzay havası radyasyonu duyarlılıklarının artması beklenebilir. Uydu içindeki bileşenlerin çok daha çabuk bozulabileceği anlamını taşımaktadır.

Uzay havası, dinamik çevresel koşulların varolduğu, yakın-Dünya uzayı ile Güneş atmosferi arasında kalan alan için bir kavramdır. Magnetosfer, iyonosfer ve termosferdeki ani değişimler sonucunda uyduların ve uydu bazlı yer sistemlerinin performansları negatif yönde etkilenebilir. Çoğu durumda etkiler görmezden gelinse dahi, bazı özel hallerde veri kayıpları, iletişim kanallarının bozulması, sistem çökmesi ya da en kötü senaryo olarak uydunun tamamiyle bozulması gözlemlenebilir. Ekonomik bakımdan çok ağır sonuçlar doğurmasının yanısıra insanlı uzay görevlerinde insan hayatını tehdit edebilecek etkenler varolmaktadır. Bu sebeplerden ötürü uzay havası unsurları, tam anlamıyla anlaşılmalı ve anomali sebepleri tam olarak belirlenmelidir.

Bu tez çalışması ile, Türk uzaktan algılama RASAT (2011) uydularında, uzay havasına bağlı olarak görülen anomalilerin incelenmesi ve arkasında yatan spesifik etkenler ile potansiyel uzay havası elemanlarının kaynağının tayini, istatistiksel yöntemler ve korrelasyon analizleri kullanılarak amaçlanmaktadır. Bu sayede daha kaliteli, korunaklı, uzay havası durumlarına karşı dayanaklı uydular üretelebilmesinin önü açılacaktır.

Anahtar Kelimele İlişkileri, Solar En	e r: Uzay Havası, RASA nerjitik Parçacıklar, Giz	AT, Uydu Anomali zli Uzay Havasi Ele	ileri, Uydu-Uzay emanları	Havasi
V	LDIZ TEKNİK ÜNİ	VERSITESI EEN	RİLİMLEDİ EN	VSTİTÜS

CHAPTER 1

INTRODUCTION

1.1 Literature Review

The recent studies show that the dynamic, harsh conditions of space weather are affecting the stability and the health of the satellites orbiting Earth negatively. It is known that Space Weather involves high energetic particles with different frequencies. When one investigates satellite anomalies in depth, it can be clearly seen that these energetic particles are the cause of some of the incidents. Yet the hidden agents of most of the satellite anomalies are still unknown. Interest in the ability to predict space weather, and its effects on Earth, really began during World War II. For the first time, electronic technologies, such as radars and radio communications, were heavily relied on, and it soon became clear that these technologies could be seriously disrupted by solar activity. After the war, more uses were developed for electronic technologies, including the start of the space program. Since then, our need to be able to forecast solar activity has continued to increase as technology becomes more widespread.

Under disturbed conditions, satellite and ground based technological systems, e.g. communications networks, electric power grids and satellites, can suffer harmful effects. Such systems are particularly vulnerable during severe geomagnetic storms. Large storms are relatively infrequent but, when they occur, they can stress the susceptible systems for prolonged periods of time over large geographic areas. Secure operation of systems can still be maintained and hazards can be minimized if the

occurrence, duration and severity of impending storms can be accurately predicted in a timely manner. Thus, space weather forecasting is important for protecting national assets in both the commercial and military sectors. In the early days of solar forecasting, it was assumed that when a large flare occurred on the Sun there would be a very predictable geomagnetic disturbance on Earth within a few hours or days. Later it was realized that it was the solar coronal ejections (CMEs) that had a greater effect on Earth. It was therefore believed that improved forecasting was just a matter of making better observations of the Sun so that flares and CMEs could be detected immediately after they occurred. Experience, however, soon showed that the effects on Earth did not correlate so simply with events on the Sun and, moreover, not all mass ejections had a noticeable effect on Earth. Sometimes geomagnetic storms occurred when there was no apparent eruptive activity on the Sun. We now know that how the Sun's magnetic field connects with the geomagnetic field makes a big difference in how solar activity affects Earth. When a mass of plasma is ejected from the Sun, the plasma travels outward in the solar wind. These plasma bursts have their own magnetic fields, which are carried along with the plasma. How these fields are oriented when they arrive at Earth determines whether or not the event will be effective. When the direction of the solar wind field is opposite the direction of Earth's field, magnetic reconnection occurs, and the magnetosphere essentially becomes joined to the solar magnetic field. In this condition, Earth is much more prone to the effects of the solar wind. Solar wind particles can enter the magnetosphere more easily, and those already within the magnetosphere are energized. If the magnetic field of the solar wind is in the same direction as the Earth's field, then magnetic reconnection does not occur and the magnetosphere is much more separated and protectedfrom the solar wind. Under these conditions, the effects of CMEs are much less significant. In order to know what is going to happen on Earth it is important to know not only what happened on the Sun but also the characteristics of the magnetic fields that are carried along with the solar wind. Accurate forecasts of large storms are difficult to achieve because the propagation of solar disturbances to the Earth and magnetic field characteristics are difficult to predict with high accuracy. Using the solar wind and interplanetary magnetic field quantities measured upstream from the Earth as input, however, can warn of the impending arrival of solar wind structures and, therefore, predict their geoeffectiveness, that is to say, their effect on the Earth. Forecasters have reviewed large amounts of historical solar wind data and have found

that they can identify and predict the occurrence of large storms, with accuracy in the range 70–80%.

The space technology is evolving rapidly with the increasing dependency of modern society to the space technology by means of communication, broadcasting and navigation, GPS systems. To meet that, modern satellites have been increasing along with their capabilities and complexities. However as the capabilities of the electronics increase, they become more susceptible to the radiation effects. Radiation damage, the susceptibility of charging effects, single event effects, surface charging and resulting electro static discharge (ESD), internal charging resulting again electrostatic discharge (ESD) is increasing, and it's clear that the trend will continue.

In most cases the effects can be disregarded, but occasionally they may have severe results leading to data loss, communication breakdowns, system failure or in worse the total loss of satellite and cost several \$100M budget. As May of 1999 there were over 600 operating spacecrafts orbiting with a total value of \$100 billion. And 226 of them were insured at a value of \$18 billion. Today those numbers are rolling to a higher ground, and one can expect to be a growing market for spacecraft services over the next years. Not to mention they can be even life threatening for manned space missions. Therefore, space weather elements have to be properly identified in order to assign each possible system anomaly and accurate assessment of cause and effect. The spacecraft designers must take into the account that there are hazardous elements in space environment and they must consider these in their executions. The solar-terrestrial environment must be understood fully by the means of its average and its extreme states. The evolution of the satellites against the conditions of space is progressing with these anomalies. Because of the economic results and the social impacts are strong and they cannot be ignored. Estimating the space weather conditions is so crucial that the forecasting systems must be ameliorated. With revealing the hidden specific agents of space weather, the performance and life spans of the future generation satellites and space crafts can be improved. Responding as fast as possible to the emergent incidents can be achieved by understanding the conditions of space weather at full capacity. This would be the only way to evade post-apocalyptic events.

The reasons behind the anomalies of Turkish Satellite: RASAT were investigated in order to obtain common elements for the satellites orbiting Earth. The models developed so far for Space weather and the space environment are valid yet they don't

hold all of the answers. Despite the fact that the assumptions and some information from earlier researches for the reasons behind the spacecraft anomalies, one cannot be sure about the fraction of the anomalies, which can be related to the space weather. Also, one cannot rely on purely physics based models to pinpoint the reasons, which are composing these anomalies. Due to the numbers of the unknown parameters in space environment depending on purely extreme value statistics cannot hold a solution by itself as well. However combining physics based models and statistical methods can give some answers.

1.2 Objective of the Thesis

In this study, Turkish remote sensing satellite of RASAT was investigated in order to understand the main reasons and specific hidden agents of its anomalies when a space weather event had occurred. Furthermore within the trace of the acquired data, a correlation between other satellites orbiting Earth and the space weather was targeted to strengthen the proof of anomaly agents' existence.

Understanding underlying mechanism of failure and anomalies will hopefully enable Turkish engineers, designers and scientists to eliminate the risk, minimize the cost, and optimize the design for future national space missions. In order to achieve that, Turkish Satellite: RASAT was monitored regularly and all key parameters were logged in order to track operational values and alert if anything goes beyond the thresholds. Both tables were compared by superposed epoch analysis technique. Possible similarities or dissimilarities in fluctuations were interpreted for better understanding of space environment and its effects on electronics.

1.3 Hypothesis

The dates in which RASAT performed severe corrections were investigated. Space weather conditions for the dates were checked by mainly focusing on the solar energetic particle flux variations, solar storms, geomagnetic storms, solar flares, coronal mass ejections. In analyzing log files of RASAT and the anomalies, A correlation between the number of corrections and the space weather events can be clearly seen.

According to some information gathered from earlier researches, in the following two years after the launch, the majority of anomalies are associated with the launching and maneuvering errors. Despite this information the reasons behind RASAT's anomalies are

related with the intense space weather events. On the dates of RASAT anomalies there were lots of malfunctioning reports for other GEO and LEO satellites. The hidden specific agents of Space Weather, the reasons behind the satellite anomalies are shown in chapter 7.

WHAT IS SPACE WEATHER?

Space weather is a term, which refers to the dynamic, and highly variable conditions in near-Earth space and the space from the sun's atmosphere to the Earth's, also including the conditions in the magnetosphere, ionosphere, thermosphere system. From the analysis of some scientific researches and recent space weather models, one can see supportive evidences for the rapid changes in the geospace environment, and their negative effects on spacecraft systems. There are many examples of the operational failures during periods of strong hazardous geomagnetic storms, intense particle flux variations were reported in the past.

There has been a major preoccupation in space researches to understand the effects of the space weather on human technological systems. To figure out the specific agents behind the spacecraft anomalies has become more popular recently. This is not a surprising development when one considers the costs of space-based missions. The social and economic impacts are crucial. Beside the financial problems large space environment events may harm human health.

In the following sections space weather elements, events and some basic information will be given.

2.1 The Sun

The nearest star to the Earth and central body of the solar system. A main-sequence, yellow dwarf of spectral type G2 V, mass 1.989×10^{30} kg, diameter 1.392.000 km, luminosity 3.83×10^{26} W and absolute visual magnitude +4.82, the Sun is the only star

whose surface and outer layers can be studied close up. From the Earth, a mere 149.600.000 km away, the Sun's disk subtends an angle of about 30' and its apparent visual magnitude is -26.78 [1].

The Sun is composed mainly of hydrogen (about 70% by mass) and helium (about 28%), with a small proportion (about 2%) of heavier elements (Fe, Ni, O, Si, S, Mg, C, Ne, Ca, Cr). In its central core, which is thought to be about 200.000 km in diameter, the maximum density is about 148.000 kg m⁻³. Here the temperature is about 15.000.000 K and hydrogen nuclei fuse together to form helium nuclei in the proton–proton (p–p) chain reaction. The energy liberated by the 4.4 × 10⁹ kg of mass lost per second in this reaction is radiated through the radiative zone to within about 200.000 km of the surface, where, the temperature having fallen to about 1.000.000 K, convection takes over. The convective zone extends to just below the surface, or photosphere, which is an opaque layer several hundred kilometers thick that represents the boundary between the solar interior and solar atmosphere [2].

The innermost layer of the sun is the core. With a density of 160 g/cm³, the core might be expected to be solid. However, the core's temperature of 15 million kelvins keeps it in a gaseous state. Recent researches support the gas theory with the help of the evidence the propagation direction of electromagnetic radiation.

In the core, fusion reactions produce energy in the form of gamma rays and neutrinos. Gamma rays are photons with high energy and high frequency. The gamma rays are absorbed and re-emitted by many atoms on their journey from the envelope to the outside of the sun. When the gamma rays leave atoms, their average energy is reduced. However, the first law of thermodynamics (which states that energy can neither be created nor be destroyed) plays a role and the number of photons increases. Each high-energy gamma ray that leaves the solar envelope will eventually become a thousand low-energy photons [3].

The Sun's radiative zone is the section of the solar interior between the innermost core and the outer convective zone. In the radiative zone, energy generated by nuclear fusion in the core moves outward as electromagnetic radiation. The energy is conveyed by photons [4].

The convection zone is the outermost part of the inner layers of The Sun. In this layer atoms have electrons due to the fact of the temperature is being less than the lower

layers. Energy transmission is faster than the radiative zone. Atoms having electrons makes the material more opaque so that it makes harder for radiation to get through. This traps heat that ultimately makes the fluid unstable and it starts to look like boiling. This process is called granulation. The combination of granulation and The Sun's differential rotastion is called the solar dynamo. The solar dynamo is closely related to the solar cycle, because the magnetic field varies with sun's cycles [5].

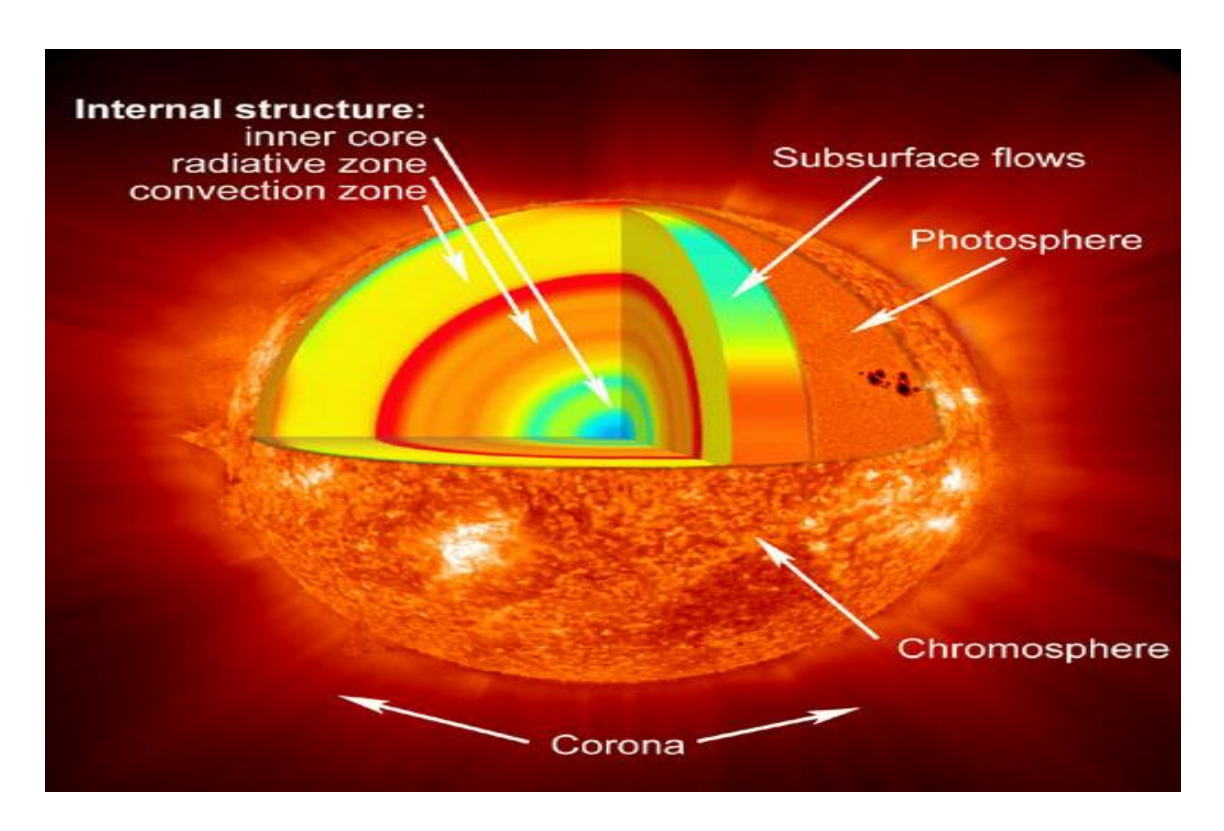


Figure 2.1 Layers of The Sun [6]

The gases of the Sun extend far beyond the photosphere, which may be considered the lowest level of the solar atmosphere. The region immediately above the photosphere is called the chromosphere. The chromosphere is 2000-3000 km thick. It glows faintly relative to the photosphere and can only be seen easily in a total solar eclipse. When it can be seen it is reddish in color (because of strong Balmer H-alpha emission) [7].

The chromosphere contains spikes of gas called spicules that rise through it. Spicules are short-lived phenomena, corresponding to rising jets of gas that move upward at about 30km/sec and last only about 10-15 minutes. There are about 300,000 active spicules at any one time on the Sun's chromosphere, amounting to about 1% of the Sun's

surface [8]. An individual spicule typically reaches 3,000-10,000 km altitude above the photosphere [9].

The transition region is a thin and very irregular layer of the Sun's atmosphere that separates the hot corona from the much cooler chromosphere. Hydrogen is ionized (stripped of its electron) at these temperatures and is therefore difficult to see. Instead of hydrogen, the light emitted by the transition region is dominated by such ions as C IV, O IV, and Si IV. These ions emit light in the ultraviolet region of the solar spectrum that is only accessible from space [10].

The outermost layer of the Sun is called the corona. The corona can be detected only during a total solar eclipse with using a coronagraph. The appearance of the corona has a very strong dependence on the solar cycle [11]. The light coming from the corona has 3 different sources. The corona is hotter than the visible surface by the factor of 200. And it is less densed than photosphere by the factor of 10^{-12} . Particles from the corona also are streamed out along the magnetic field lines of the Sun that extend into interstellar space by solar winds [12].

2.1.1 The Solar Wind

The solar wind is a flow of ionized solar plasma and a remnant of the solar magnetic field that pervades interplanetary space [13]. It is a result of the huge difference in gas pressure between the solar corona and interstellar space. This pressure difference drives the plasma outward, despite the restraining influence of solar gravity.

The solar wind contains largely of ionized hydrogen, with a small admixture of ionized helium and still fewer ions of heavier elements. Embedded in this plasma is a weak magnetic field oriented in a direction nearly parallel to the ecliptic plane (the plane of the Earth's orbit around The Sun), but at approximately 45° to a line from the sun to the observer at 1 astronomical unit (AU) (Parker, 1958). The solar wind has a speed ranging from 300 to more than 1000 km/s, with an average of about 400 km/s.

It is often useful to describe the solar wind in terms of the fluxes or flux densities of quantities that are conserved in a plasma flow. The radial-momentum flux is also often called the dynamic pressure, because of its role is confining the magnetospheric magnetic field. Most of the protons is carried by the protons; most of the energy is in the form of kinetic energy of the same particles [13].

Table 2.1 Solar-Wind Flux Densities near the Orbit of the Earth [14]

	Flux Density	Flux Through Sphere at 1 AU
Protons	$3.0 \times 10^{8} \text{ cm}^{-2}.\text{s}^{-1}$	$8.4 \times 10^{35} \text{ s}^{-1}$
Mass	5.8x10 ⁻¹⁶ g.cm ⁻² .s ⁻¹	$1.6 \times 10^{12} \mathrm{g.s^{-1}}$
Radial Momentum	2.6x10 ⁻⁹ PA	7.3x10 ¹⁴ N
Kinetic Energy	0.6 erg.cm ⁻² .s ⁻¹	$1.7 \text{x} 10^{27} \text{erg.s}^{-1}$
Thermal energy	0.02 erg.cm ⁻² .s ⁻¹	$0.05 \text{x} 10^{27} \text{erg.s}^{-1}$
Magnetic Energy	0.01 erg.cm ⁻² .s ⁻¹	$0.025 \times 10^{27} \mathrm{erg.s}^{-1}$
Radial Magnetic Flux	5x10 ⁻⁹ T	1.4x10 ¹⁵ Wb

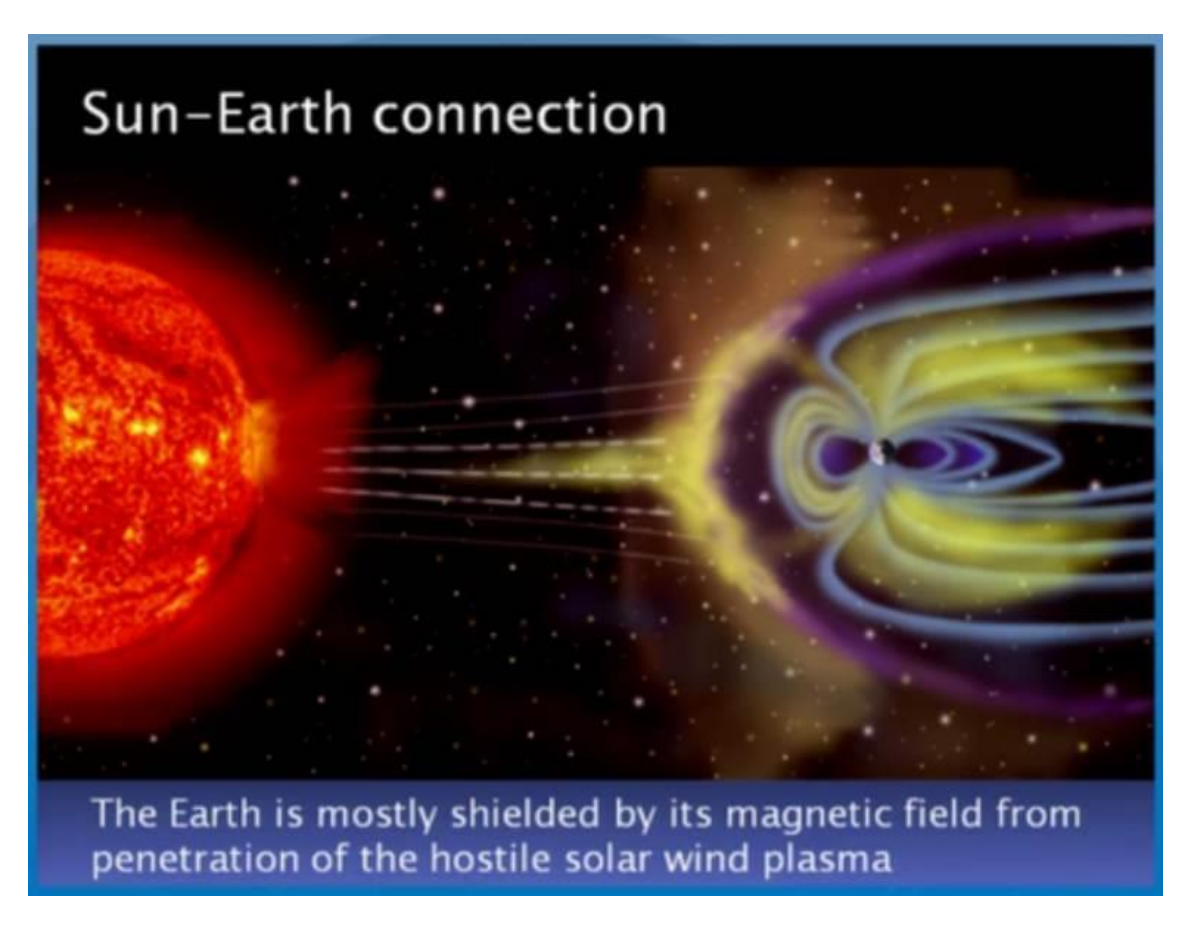


Figure 2.2 The Solar Wind Hitting the Earth's Magnetosphere [15]

Hot solar corona undergoes a steady expansion, while the low value plasma velocity near the Sun increases to a large supersonic expansion speed at large heliocentric distances. Because of the high electrical conductivity of the coronal plasma the magnetic field lines are frozen in the bulk plasma flow, which transports the magnetic field lines into the interplanetary space.

The solar wind carries mass away from the sun at a rate of $1.6x10^{12}$ g.s⁻¹, and energy at a rate of $1.8x10^{20}$ joule.s⁻¹. Even with these great rates in the present-day, solar wind is virtually negligible in the overall mass and energy balance of The Sun.

Table 2.2 Some Derived Properties of the Solar Wind near the Orbit of the Earth [14]

C. B.	20 . PA
Gas Pressure	30 pPA
Sound Speed	60 km.s ⁻¹
Magnetic Pressure	19 pPA
Alfén Speed	40 km.s ⁻¹
Taken speed	i and an an an an an an an an an an an an an
Proton Gyroradius	80 km
Proton-proton Collision Time	$4x10^{6}$ s
Electron-electron Collision Time	$3x10^{5}$ s
Time for Wind to Flow Corona to	$\sim 4 \text{ days} = 3.5 \times 10^5 \text{ s}$
1 AU	

The solar winds may have irregularities [16]. One can distinguish these kind of shocks from the quite solar winds with the help of some specific parameters such as the plasma speed, density, temperature, and magnetic field's strength. When irregular solar winds reach the earth they hit the magnetosphere, and create disturbances. The collision of ions in the solar wind produces a negligible viscosity in the flow past the geomagnetic field, but such an inviscid flow is shown to be unstable. The resulting disordered

interface between the field and the wind yields Fermi acceleration of ions and consequently a not insignificant effective viscosity.

The Fermi acceleration results in suprathermal ions which may have an energy spectrum like that observed for primary auroral protons [17]. As a result many substorms are formed. If the number of these storms increases then a greater storm will occur.

2.1.2 Solar Flares

In contrast to flares on other stars or to many analogous phenomena in the Universe, flares on the Sun are accessible to a broad variety of observational methods. Solar flares emit radiation which covers virtually the whole electromagnetic spectrum, from kilometer radio waves to hard gamma rays, and which can be detected by Earth-based, satellite borne, and interplanetary observing stations. At the same time the particles accelarated in the flare, the plasma ejected into the interplanetary space, and secondary ionospheric and geomagnetic events related to the flare are detected directly.

Flares are the most powerful of all manifestations of solar activity. The energy of a large flare can be as large as $(1-3)x10^{25}$ joule, which is almost 100 times more than the energy obtained from burning the known reserves of oil and coal on the Earth. On the Sun this gigantic amount of energy is released within several minutes to tens of minutes.

The process of energy release in a solar flare can be conventionally divided into four parts;

The violent discharge of energy in the flare is preceded by a stage of *preheating* (PH). The name of this phase is rather conventional, but its existance has a crucial significance both for an early diagnosis of flare events and for an understanding of their mechanism. During this stage one can observe small bright bands with light x-ray and radio wave radiation (Kundu and Lang). The effects of the magnetic flux can be observed. The most important feature of this stage is that during preheating the necessary conditions for flaring is prepared (Priest 1984). There are no productions of non-thermal electrons.

The preheating phase is followed by the phase with fast MHD plasma flows and the local restructuring of magnetic fields. This is called the *explosive phase* (EP). From its background one can recognize the *impulsive phase* (IP) of the flare as a sequence of

short powerful bursts. This phase is usually shorter than the explosive phase; sometimes these two phases are improperly treated as a single phase under the name of either

'explosive' or 'impulsive'. Light x-ray flux increases during the impulsive phase. With this increment, light x-ray flux profile and heavy x-ray flux profile look almost identical (R. L. F. Boyd).

During each abovementioned bursts, which are sometimes, also improperly called 'elementary', electrons and ions are rapidly accelerated to high energies within several seconds.

Then the last phase; the *hot* (HP) or *main phase* (MP) of the flare follows. It is called hot because its most prominent manifestation is the x-ray emission from high temperature and relatively dense plasmas in the corona, and main because it is apparently during this phase that the largest of the total flare energy is released; this energy has the form of an intense flow of heat. Such is the scenario of energy release in flares [18].

At some moments, in particular during the impulsive phase, the rate of energy release can be several times larger than the values given above. However, it is easy to see that even the energy release is the order of only 0.01 percent of the total output of the Sun 3.83×10^{28} joule/s (R.L.F. Boyd). Therefore no marked increase in solar luminosity can be seen during the flare. Only the largest flares can be seen in 'white light'. Flares are usually observed as marked brightness enchancements not in the photosphere, but in the chromosphere, in chromospheric lines, in particular in the H_{α} line of hydrogen.

A significant part of the energy of flares is manifested in the form of MHD ejections of plasma, which move with velocities sometimes exceeding 1000 km/s in the corona and interplanetary space, as well as in the form of streams of high-energy particles: electrons, protons and heavier nuclei. Hard electromagnetic radiation of the flare and its radio emission, different from that the quiet Sun, are also evidence of the existance of non-thermal processes in the flare mechanism. However the relative magnitude of these processes in the flare energy budget does apparently not exceed 10 % (B.V. Somov).

The data acquired from the satellites that had been sent to space under the solar maximum missions showed that the radiation bandwidth is between 20 kev and 7 MeV. These bands have a ~10 seconds pulse timers. This helps electrons and ions to accelerate as soon as impulsive phase starts. Accelerated protons and some ions

propagate into the dense layers of the solar atmosphere [19]. Secondary ionospheric and geomagnetic incidents are directly related to the solar flares. Therefore the solar flares can affect space and ground based systems negatively.

There are 5 types of solar flares, and were classified as A, B, C, M or X according to the peak flux (in watts per square meter, W/m²) of 1 to 8 ångströms X-rays near Earth, as measured by the GOES satellites. Each X-ray class category is divided into a logarithmic scale from 1 to 9. For example: B1 to B9, C1 to C9, M1 to M9. An X2 flare is twice as powerful as an X1 flare, and is four times more powerful than an M5 flare.

Table 2.3 The Classification of the Solar Flares [20]

Class	W/m² between 1 & 8 ångströms
A	<10 ⁻⁷
В	$\geq 10^{-7} < 10^{-6}$
С	$\geq 10^{-6} < 10^{-5}$
M	≥10 ⁻⁵ <10 ⁻⁴
X	$\geq 10^{-4} < 10^{-3}$
Super X	≥10 ⁻³

The *X-class*; category is slightly different and doesn't stop at X9 but continues on. These solar flares are the biggest and strongest of them all. Strong radio black-outs will occur on the day-light side of the Earth during the solar flare, long lasting solar radiation storms can occur and strong geomagnetic storming is possible when the associated Coronal Mass Ejection arrives. The X-class continues after X9 instead of getting a new letter. These are super X-class solar flares. Solar flares as strong or stronger than X10 are however very rare and it is good that these eruptions do not happen often because the consequences on Earth could be severe. One thing to note

with super X-class flares is that an X20 solar flare is not 10 times as strong as an X10 solar flare.

An X10 solar flares equals an X-ray flux of 0.001 Watts/m² while an X20 solar flare equals 0.002 Watts/m² in the 1-8 Ångstrom wavelength.

M-class flares; These are what we call the medium large flares. They cause small (R1) to moderate (R2) radio blackouts on the daylight side of the Earth. Small radiation

storms can also happen. Only strong M-class flares which are long in duration and are accompanied by an Earth-directed Coronal Mass Ejection (CME) could cause auroral storming on the middle latitudes.

C-class flares; These are small solar flares that have almost no effect on Earth. Only C-class solar flares which are long in duration might produce a produce a Coronal Mass Ejection (CME) but they are usually slow, weak and do not cause any significant geomagnetic disturbance.

A & B-class flares; Small sunspots can flare as well and they result in minor B-class eruptions. During solar minimum, solar activity doesn't go higher than the A-class.

2.1.3 Coronal Mass Ejections

The most basic definition of a CME is that it represents a discrete ejection of mass from the solar atmosphere detected as a transient feature expanding outward through a coronagraph field of view. CMEs represent a significant, rapid restructuring of a large portion of the solar atmosphere as the mass is ejected. CMEs occur in all shapes and sizes, and with many topological variations, but some basic characteristics are quite common.

Coronal mass ejections (CMEs) are the most energetic events in the solar system. They are spectacular displays representing the sudden eruption of up to 10^{16} gm of coronal material at speeds of typically several hundred kilometers per second (Hundhausen, 1999). CMEs keep accelerating when leaving the Sun. Their acceleration profiles are almost same with the normal or slow solar winds. This means even a slow CME is produced by the same forces (pressure gradients).

CMEs are also the primary cause of the largest and most damaging space weather disturbances (Gosling, 1993). Effects include the temporary and sometimes permanent

failure of satellites, the degradation or disruption of communication, navigation, and commercial power systems, and the exposure of astronauts and polar-route airline crews to harmful doses of radiation.

Some of these effects are delayed approximately by 3 days, it is the time for CMEs to propagate towards Earth and to interact with the magnetosphere.

Others begin almost immediately after the CME lifts off from the Sun due to the production of solar energetic particles (SEPs) that travel at relativistic speeds.

The solar atmosphere is an environment where the interplay between the solar plasmas and magnetic fields produces a complex hierarchy of magnetic loops containing plasmas at temperatures up to a few million kelvins.

These loops are rooted in the body of the Sun and move with the surface plasma, which is subject to differential rotation as well as the turbulent effects of the convection patterns below the surface. The net result is an environment where magnetic field systems can be driven to a great deal of complexity; the motions of the solar surface literally weaving the magnetic field lines into highly stressed patterns. Eventually, one could imagine some kind of breakdown or rapid expansion of magnetic fields, where the response to further motion actually drives magnetic fields outwards and this becomes the CME. CMEs contain mostly electrons and protons, and also some heavy ions.

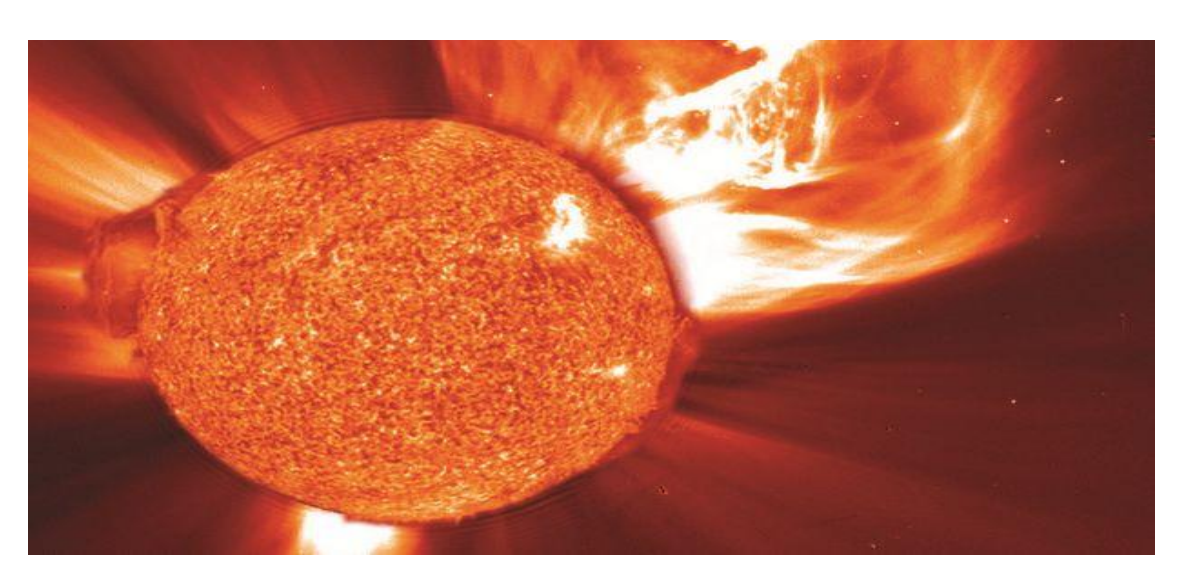


Figure 2.3 A Coronal Mass Ejection Event [21]

The CME source regions within the Sun's atmosphere can be hundreds of thousands of km across and the resulting CMEs can expand into space at many hundreds of km s⁻¹. The rate of CME eruptions varies with the solar cycle. During a solar maximum 3.5 CME events happen at average per day, and during a solar minimum this number becomes 0.1 [21].

As well as variations in the CME rate, the solar cycle sees a variation in the latitude of CME source regions. During solar minimum CMEs tend to come from regions focused at or near the solar equator. At solar maximum, CMEs come from a larger spread of solar latitudes. This appears to be a direct association with other coronal features. At solar minimum the helmet streamers are mainly confined to a single belt around the Sun which lies at low latitudes. At solar maximum the corona is far more complex with systems of streamers at all but the highest latitudes. This appears to confirm that the majority of CMEs are associated with streamers.

The life cycle of a CME encompasses a wide range of plasma processes in which the magnetic field plays a dominant role. Dynamo activity in the solar interior creates the magnetic field which builds up in the corona. Ultimately, this field erupts as a result of an instability or loss-of-equilibrium process which is yet to be identified. Once a CME is underway, a whole host of additional processes are triggered. These include magnetic reconnection, shock formation, and particle acceleration, among others [22].

The dynamics of CMEs after initiation involves several factors. These include acceleration, expansion, drag, and distortion. Although acceleration and expansion are an integral part of the initiation process, they may also play a role in the long term evolution of the CME either through a sustained operation of the forces which initiate the CME or through the interaction of the CME with the ambient solar wind. Drag and distortion result from the interaction of the CME with the ambient solar wind, corotating interaction regions (CIRs), and other CMEs [23].

Coronal mass ejections are frequently associated with prominence eruptions as well as solar flares. Prominences (called filaments when observed on the solar disk) support cool, dense chromospheric material ($\sim 10^4$ K and $10^{10}-10^{11}$ cm⁻³) against solar gravity in the surrounding hot, tenuous corona ($\sim 10^6$ K and 10^7-10^9 cm⁻³).

They are observed to lie above magnetic neutral lines in the photosphere and near the base of helmet streamers (regions of closed magnetic field that have confined the coronal plasma).

The magnetic field in the prominence often exhibits "inverse polarity," meaning that when the coronal magnetic fields embedded in the prominence cross over the neutral line, they point in the direction opposite to that indicated by the photospheric magnetic field polarity (Leroy, 1983, 1984). The prominence magnetic field is itself nearly aligned with the filament channel (Martin, 1994), indicating a highly sheared (and therefore magnetically energized) configuration. A current filament (in two dimensions) produces closed magnetic loops that can support prominence material above the photosphere. Since that time there have been a number of authors who have focused on the support of prominence material by helical field lines and/or the disruption of these configurations as the possible cause of prominence eruptions and coronal mass ejections (van Ballegooijen and Martens, 1989). The flux rope could emerge intact from below the photosphere or be formed as the result of motions at the photosphere or above. That flux ropes are first formed, and subsequently erupt, as a result of flux cancellation at the photosphere. Once a flux rope structure has formed in the corona, the susceptibility of the structure to eruption shouldn't depend on its origin.

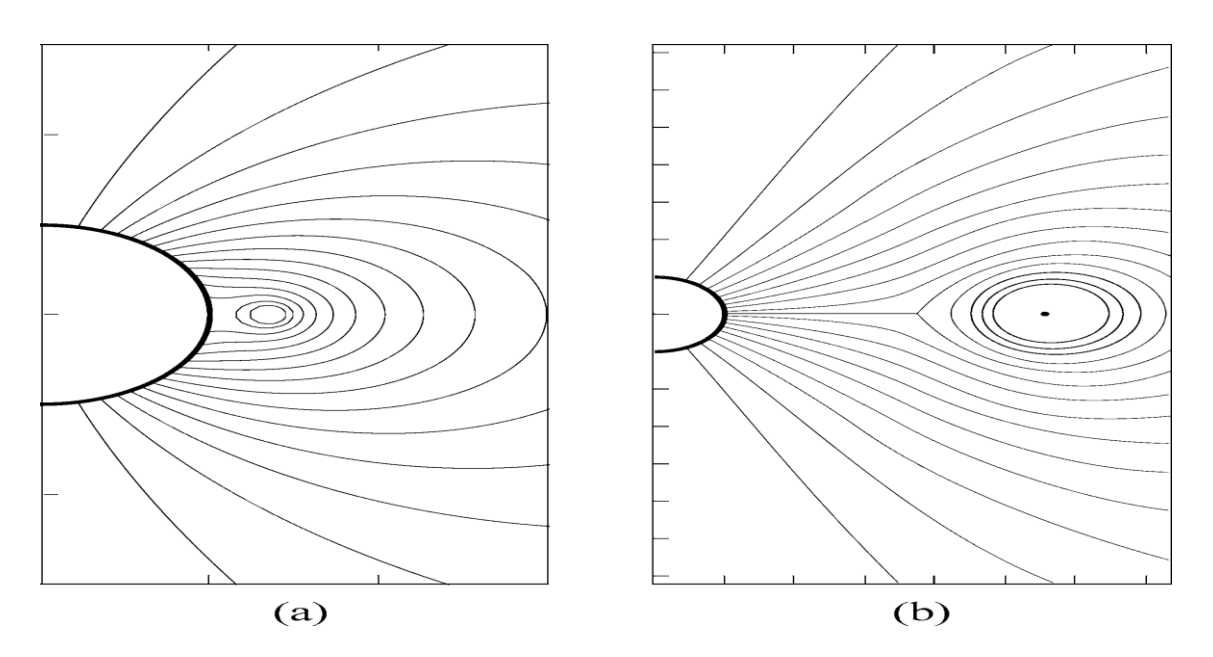


Figure 2.4 Azimuthally-symmetric flux rope model showing the ideal MHD transition from a flux rope in equilibrium close to the Sun (a) and the same flux rope at a large distance from the Sun after the transition (b). A current sheet forms as a result of this transition [24]

Observationally flux cancellation is defined as the mutual disappearance of magnetic fields of opposite polarity at the neutral line separating them (Martin, 1985). Flux cancellation occurs everywhere on the Sun, (Livi, 1985); observations have shown it to be active at filament sites (Litvinenko and Martin,1999) and in active regions as they disperse (Martin, 1985). During this time, filaments are frequently observed to form along the neutral line. At times, these filaments disappear, presumably due to eruption, and may even reform in the same location later. The recognition that flux cancellation is active at filament sites and during the eruptive process led to the interpretation that the cancellation was in fact the annihilation of magnetic flux at the photosphere through reconnection.

Once a flux rope is formed, continuation of the flux cancellation process can result in a loss of equilibrium. The new lower-energy equilibrium contains a current sheet and a higher height for the flux rope. While the energy release in this ideal process is relatively small, the new equilibrium height of the flux rope can be many solar radii from the Sun. The reason for this transition in equilibria can be understood as follows: The magnetic pressure forces in the flux rope want the rope to expand; these forces are restrained by tension in the surrounding fields. Flux cancellation converts the restraining field into magnetic flux in the rope, increasing the magnetic pressure. Eventually the system reaches a point that no nearby equilibrium is accessible. Significant magnetic energy release could then occur through magnetic reconnection at the current sheet.

The flux cancellation mechanism is an attractive explanation for both prominence formation and the initiation of CMEs with associated prominence The mechanism assumes that the frequent cancellation events that occur during the lifetime of an active region annihilate some of the surface magnetic flux and convert sheared fields in the active region into a flux rope. The flux rope, which supports the cool, dense material observed in prominences, can be stable for hours, days or weeks until cancellation increases the magnetic pressure in the flux rope to the point that it exceeds the surrounding tension, causing the violent eruption.

The most widely accepted models for CME/eruptive flares are those in which the energy for the eruption is stored in coronal magnetic fields, specifically, the strongly sheared/twisted field of a filament channel (Forbes, 2000).

The basic picture is that a CME represents the catastrophic disruption of the force balance between the upward magnetic pressure of the highly-sheared filament-channel field and the downward tension of overlying quasi-potential field. Since the upward pressure force is constrained to increase only slowly, either by flux emergence or by photospheric motions, explosive eruption must be due to the fast decrease of the downward tension. Three general types of reconnection models for CME initiation have been proposed, differing primarily in magnetic topology and in location of the reconnection. Reconnection is postulated to occur external to the filament channel, between the quasi-potential overlying flux and neighboring flux systems (Antiochos, DeVore 1999). Consequently, an essential requirement for the breakout model is that the coronal magnetic topology is due to a multipolar flux distribution at the photosphere and that it contains at least one null point where reconnection can occur.

Observations suggest that the Sun creates filament channels through some not-yet understood process involving flux emergence, cancellation, and/or post-emergence subsurface motions (Martin, 1984, 1994). Furthermore, the breakout model is expected to be insensitive to the details of the filament channel formation process. Unlike most other models, which require a particular form for the photospheric evolution and the filament field in order to obtain eruption, breakout should work for either flux emergence or cancellation and either a sheared arcade or a twisted flux rope. The effect of the photospheric shear flow is to generate a large magnetic component parallel to the neutral line, $(B\varphi)$, which produces an upward magnetic pressure. This added pressure causes the overlying potential field lines to expand outward and increase their net downward tension, leading to the basic pre-eruption force balanc. Another effect of the outward expansion is to stretch radially the field near the null so that the null region deforms into a current sheet structure As long as the width of the current sheet is large compared to the grid scale of the simulation, the effective diffusion is negligible, and the system maintains a true stable equilibrium. It should be emphasized that such a stable energy buildup phase is necessary for all explosive eruption models.

As the shearing continues, however, the width of the current sheet structure at the null eventually decreases to the grid scale, and reconnection begins. Once reconnection appears, the outward expansion rate grows exponentially, even with no further shearing, because reconnection removes the overlying flux, thereby decreasing the downward tension.

The tension decrease allows the sheared field to expand outward faster, which, in turn, drives faster reconnection. Energetically, the breakout mechanism can be considered to yield explosive eruption by minimizing the amount of flux that must open along with the sheared filament channel field. For this simulation, the trigger for the eruption is the turn-on of numerical resistivity due to its grid dependence. It is likely that a scaledependent resistivity due to collisionless effects or current-driven instabilities also operates in the Sun's corona. The important point for the model, however, is not that the breakout reconnection has a rapid turn-on, but that once it is on, the subsequent global evolution of the system causes the current sheet width to decrease and to drive the reconnection at an ever-faster rate. One consequence of the eruption is that originally low-lying field lines become so expanded radially that they begin to approach the open state and, consequently, a vertical current sheet forms deep inside the sheared field region leading to reconnection there. It should be emphasized that this reconnection is completely distinct from the breakout reconnection ahead of the eruption. The reconnection that begins deep inside the erupting field corresponds to the usual flare reconnection and is common to nearly all CME models. In the breakout model, the flare reconnection does not initiate the eruption, but it may help accelerate it. Furthermore, the twisted flux rope that forms due to this flare reconnection is a consequence of eruption, not its cause [24].

Surely these models will help to understand the mechanisms of CMEs in order to deduce their effects on the Earth. By doing so the new generation space crafts, satellites will be secured. The effects of CMEs will be discussed more briefly in chapter 3.

2.1.4 Solar Spots

The photosphere has a mottled appearance called granulation, which represents the tops of convection currents from below. Within the granulation dark markings called sunspots appear, surrounded by lighter faculae which are visible well away from the brighter central region of the Sun's disk. Sunspots and faculae mark the position of intense, localized magnetic fields, and their numbers and mean latitude change over an average period of approximately 11 years—the so-called sunspot cycle.

Sunspots are the manifestation of strong magnetic fields that erupt from below the solar surface.

Because this erupting flux is always a system of magnetic-field loops, the intersections of the two 'legs' of the loop-system with the solar surface create a bipolar group of sunspots. Thus the most meaningful descriptive record of sunspots is their appearance in groups.

The sunspot group provides clues about the potential for eruptive activity in an active region. A description of sunspot groups in a formalized system of classification provides the basis for solar flare prediction. It is also a taxonomy of the sunspot phenomenon that becomes one of the essential data in the solar climatic record.

Sunspots are like snowflakes; each one is unique but has size and structure similar to other sunspots. The similarities are the basis for classifying the groups. The periodic increase and decrease in the number of sunspots and sunspot groups on the surface of the Sun. The number of spots and groups reaches a maximum, on average, once every 11 years. At the intervening sunspot minima, the solar disk maybe devoid of spots for weeks on end. On average, the rise to maximum activity takes 4 to 5 years and the subsequent decline to the next minimum, about 6 to 7 years. The level of activity in successive cycles can vary substantially [25].

At the beginning of each cycle, spots start to appear at latitudes of about 30° (occasionally as high as 40°) north (+) and south (-) of the solar equator. As the cycle advances, the bands of sunspot activity migrate towards the solar equator. At solar maximum, the average latitude at which spots occur is about $\pm 15^{\circ}$, and by the end of the cycle, around $\pm 8^{\circ}$, by which time the first spots of the next cycle may be beginning to appear at latitudes of $30^{\circ}-40^{\circ}$ [26].

In each spot pair, the spot which is ahead, in the sense of the direction in which the Sun rotates, is called the leader, and its companion, the follower. Throughout a complete cycle, from one minimum to the next, all of the spot pairs and groups in the northern hemisphere have the same polarity pattern, and those in the southern hemisphere have the opposite. For example, in one particular cycle, all the leaders in the northern hemisphere will have positive polarity and all the followers negative, whereas all the leaders in the southern hemisphere will have negative polarity and the followers positive. At the end of that cycle, the polarity pattern reverses, so that in the subsequent cycle all northern hemisphere leaders will have negative polarity and all southern

hemisphere leaders, positive. The complete magnetic cycle consists of two successive 11-year sunspot cycles and is, therefore, 22 years long.

During the earlier part of each cycle, the leading spot in each pair (or the leading area of net magnetic polarity in each group) has the same magnetic polarity as the net polar polarity in the hemisphere within which it is located. As each spot or group decays, the polarity of the follower preferentially diffuses towards the pole. The cumulative effect of this process eventually produces a reversal of polarity at each of the solar poles. This usually occurs around the time of solar maximum, but considerable variations occur and, while the piecemeal reversal is taking place, the Sun, for a time, may have the same net polarity at both poles.

The sunspot cycle is part of an overall solar cycle whereby all forms of solar activity, including sunspots, plages, prominences, flares and coronal mass ejections, together with the shape, extent and structure of the chromosphere and corona, undergo cyclic variations with a period of about 11 years. The numbers, sizes and energies of prominences, flares and coronal mass ejections mirror the increase and decrease in sunspot numbers and the corona is brighter, more extensive and more symmetrical around solar maximum than at times of minimum activity.

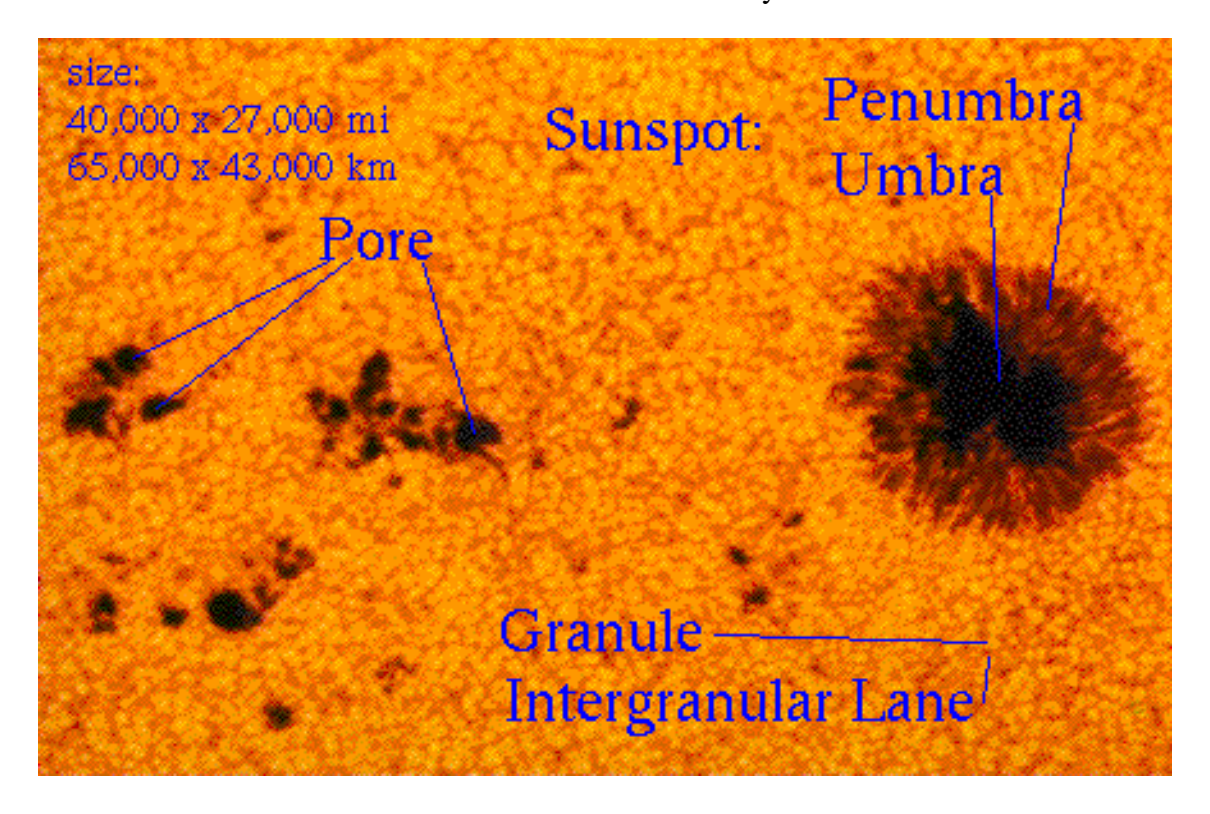


Figure 2.5 Sun Spot Classification [27]

In addition to the 11-year cycle, there is some evidence to suggest that sunspot numbers, and levels of solar activity as a whole, undergo longer-term modulations over periods of 80 years and more.

Sunspots are dark, generally roughly circular areas in the solar photosphere where there are strong magnetic fields that are approximately vertical to the solar surface in the sunspot umbra. These magnetic fields are quite strong— several thousand gauss near the center of the largest sunspots and somewhat weaker in smaller sunspots. The darkest central part (umbra) of a sunspot may have an intensity in the visible part of the spectrum that is only about 5% that of the surrounding solar surface. The outer part of a sunspot (sunspot penumbra) has an intensity much closer to that of the surrounding atmosphere.

Sunspots normally appear in groups of two or more. These are called 'sunspot groups'. Single-spot groups are rare. Sunspot groups are usually aligned along an axis that is oriented approximately (but on average not exactly) in the east—west direction on the Sun. Often the westernmost (leading, in the sense of solar rotation) and easternmost (following, in the sense of solar rotation) sunspots are clearly separated. In general, the leading and following sunspots have opposite magnetic polarities, and this orientation of polarities is predominant in one (north or south) hemisphere during a solar cycle. The polarity orientations are opposite in the other hemisphere.

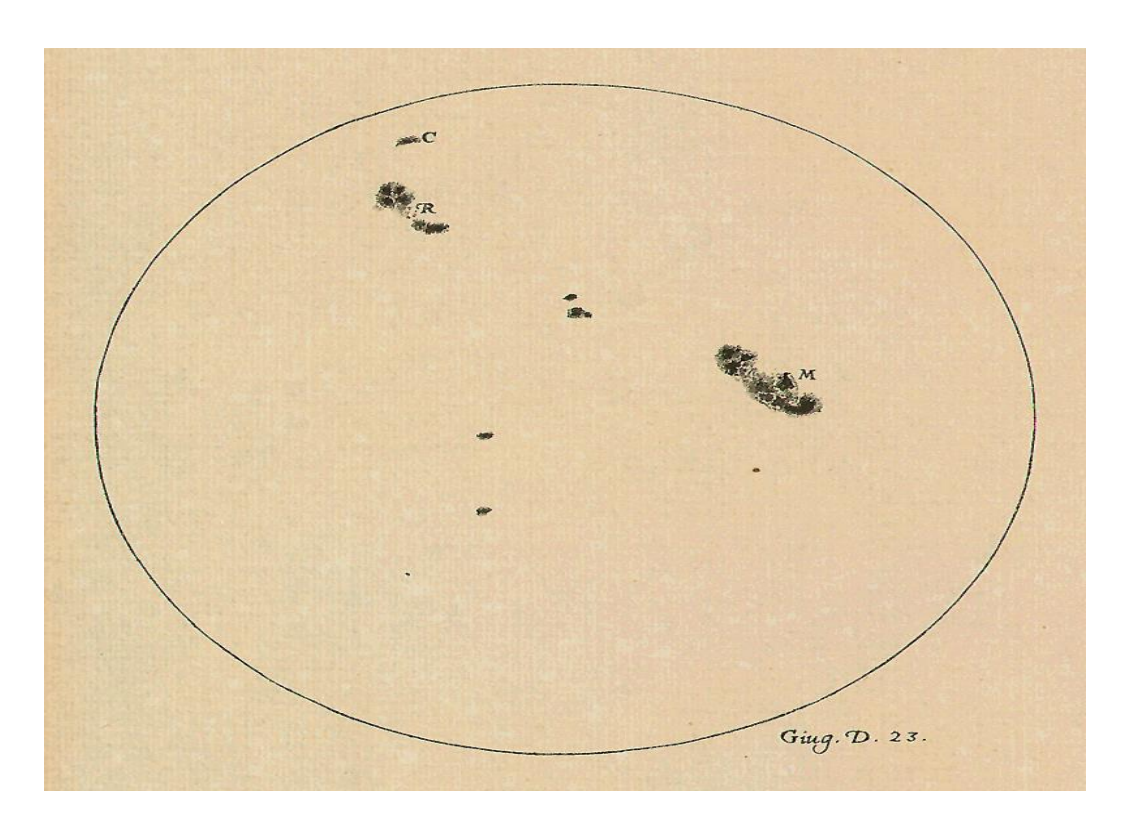


Figure 2.6 Early Work on Sunspots, This Drawing was done by Galileo Galilei [28]

Each 11 yr solar cycle has the opposite sunspot-group polarity orientation to the previous solar cycle. One can imagine an axis drawn, connecting the leading and following sunspots (or the centroids of the leading and following collections of sunspots). The angle which this axis makes with the local parallel of latitude is referred to as the 'tilt angle'. The average tilt angle is about +5°, where the plus sign indicates that the leading sunspots are (on average) equatorward of the following sunspots in each hemisphere [29].

Sunspots looks dark because of the fact that they are colder than the photosphere surrounding them, and magnetic field limits the convection current. As a result the cooling takes place locally. Magnetic field tube under the surface of the photosphere penetrates through due to the magnetic buoyancy [30].

The lifetimes of sunspots range from tens of minutes to months. More than half of sunspots have lifetimesless than 2 days. Ninety per cent of sunspots have lifetimes less than 11 days. Only a few sunspots per 11 yr solar cycle have lifetimes of more than a few months. On average, high-latitude sunspots have relatively short lifetimes. Sunspots with lifetimes of more than several months are extremely rare.

The longest-living sunspots are always large, round, single-spot groups, at least in the later stage of their lifetimes. They are generally the last survivors of large, multispot sunspot groups. It is not known why a few sunspots have very long lifetimes, whilenearly all sunspots of similar size do not live nearly as long.

There isn't a direct relationship between the sunspots and the man made technological devices, yet according to the latest researches sunspots are covering some roles on solar flare incidents and the solar wind mechanisms [31].

2.2 Solar Energetic Particles

SEPs play important role in the present day society. Our modern life is strongly dependent upon information from satellites, weather forecast, car navigation, TV and so on even though we are not aware of them. SEPs hitting electronics of these satellites produce errors in their function or can damage them. Energetic particles are also dangerous for human health when they hit the human body. Usually we are protected by thick absorber of the earth's atmosphere, but astronauts and airplane crew are directly irradiated by particles. Protection of the satellite electronics and human body from these radiations is important and it is one of the important topics in space weather forecasting. To understand the basic processes of particle acceleration and transport is important to predict the arrival of SEPs.

Solar energetic particles (SEPs) are transient enhancements of the intensities of energetic protons, ions, and electrons observed in the interplanetary (IP) space. They are known to follow in time eruptive phenomena in the solar corona, such as flares and coronal mass ejections (CMEs). Both small scale processes during flares and CME-driven shock waves are used to explain the particle acceleration [32]. On certain occasions transient energetic particle fluxes from the Sun, may comprise relativistic nucleons at energies up to several GeV or even tens of GeV.

Events with significant intensities of >10 MeV protons occur at an average rate of ~13 yr⁻¹near solar maximum and several events with high intensities of >100 MeV protons occur each decade. As particles stream out along magnetic field lines from a shock near the Sun, they generate waves that scatter subsequent particles. At high intensities, wave growth throttles the flow below the "streaming limit." However, if the shock maintains its strength, particle intensities can rise above this limit to a peak when the shock itself passes over the observer creating a 'delayed' radiation hazard, even for protons with

energies up to ~1 GeV. The streaming limit makes us blind to the intensities at the oncoming shock, however, heavier elements such as He, O, and Fe probe the shape of the wave spectrum, and variation in abundances of these elements allow us to evade the limit and probe conditions at the shock, with the aid of detailed modeling. At high energies, spectra steepen to form a spectral 'knee'. The location of the proton spectral knee can vary from ~10 MeV to ~1 GeV, depending on shock conditions, greatly affecting the radiation hazard (Reames 2000, Tylka 2000).

The acceleration mechanisms are thought to be related to the flare, which generally means magnetic reconnection, or to the shock wave generated by the CME. Which of the flare or the shock wave actually is the accelerator is hard to say on observational grounds. Statistical associations do not provide an answer. The relative timing of particle arrival at the Earth with respect to manifestations of flares and CMEs has generally been used in a very simplified way, hypothesizing that when the release of the first relativistic particles observed could not be related to the onset of radiative signatures of energetic particles during a flare (gamma-ray, hard X-ray, radio), a flare-independent acceleration process had to be invoked. From this line of reasoning many studies concluded that relativistic solar particles were accelerated at CME shocks (Lockwood 1990; Kahler 1994; McCracken 2012).

On Earth, these particles affect radio transmission and the chemistry of the upper atmosphere and ozone layer. Satellites are affected by radiation damage to electronics and to photocells that produce power and provide images. Sun sensors and star sensors used for spacecraft orientation are blinded during large SEP events. During their life time their intensity may vary (Reanes 1999, Gosling 1993, Kahler 1994). SEP intensity profiles change appearance with longitude. When these particles reach the Earth, they create disturbances on radio transmissions and upper atmosphere's chemistry. Satellite system electronics and photocells may be damaged [33].

There is an upper bound on the intensities of particles that arrive early in SEP events (Reames 1990, Ng and Reames 1994, Reames and Ng 1998). This "streaming limit" can have a major impact on 1) the probability of occurrence of events with high flux or fluence, and on 2) mission strategies for protecting astronauts from rare but lethal radiation doses (Reames, 1999). Particles streaming along magnetic field lines generate resonant Alfvén waves that scatter other particles that follow (Stix 1962, Lee 1983). As the intensity of streaming particles increases, the wave generation also increases until

there is enough scattering to sharply curtail the streaming, effectively throttling the particle flow and trapping particles near the shock. If the shock is strong enough to continue acceleration out to 1 AU, however, an intense peak can be seen later in the event when the shock itself arrives at the spacecraft.

Once the observed proton intensities reach the streaming limit, intensities at the oncoming shock are hidden from view no matter how large they become. However, ions of other elements such as He, C, O, Si, and Fe resonate with different waves than protons of the same velocity, so these ions differentially probe the shape of the protongenerated wave spectrum between the shock and Earth. Thus, abundance ratios like Fe/O (relative to abundances in the corona or solar wind (Reames 1999a)) can be enhanced early in an SEP event because Fe escapes the shock more easily than O. Nearer the shock, Fe/O is depressed because the Fe has preferentially leaked away. Not only do abundance variations provide a means to avoid the censorship of the streaming limit, they also provide a powerful test of the new SEP models that follow the evolution of particles and waves in time and space (Ng, Reames, and Tylka 1999).

As a particle scatters back and forth across a shock, it gains an increment of energy on each transit. Protongenerated resonant waves increase the scattering, improve the containment, and greatly increase the acceleration efficiency. Eventually, however, particles reach an energy where the intensities of both particles and resonant waves diminishes. There the particles begin to leak away from the shock and the accelerated spectrum steepens. This is the spectral "knee." Ellison and Ramaty (1985) described shock spectra as a power law times an exponential; the efolding energy of this exponential is the knee energy, $E_{\rm knee}$.

Differences in the knee energies cause vastly different behavior above ~100 MeV. Soft radiation, with E ~40 MeV, begins to penetrate spacecraft walls, while hard radiation,

with E >130 MeV, can penetrates 5 cm of Al and becomes extremely difficult to shield. Behind 10 g cm⁻² of material astronauts would receive a dose ~4 rem hr⁻¹ at intensities in the 1989 September event, accumulating their annual dose limit, currently 50 rem, in relatively few hours. Differences in the knee energy alone can turn a benign event into a significant radiation hazard [33].

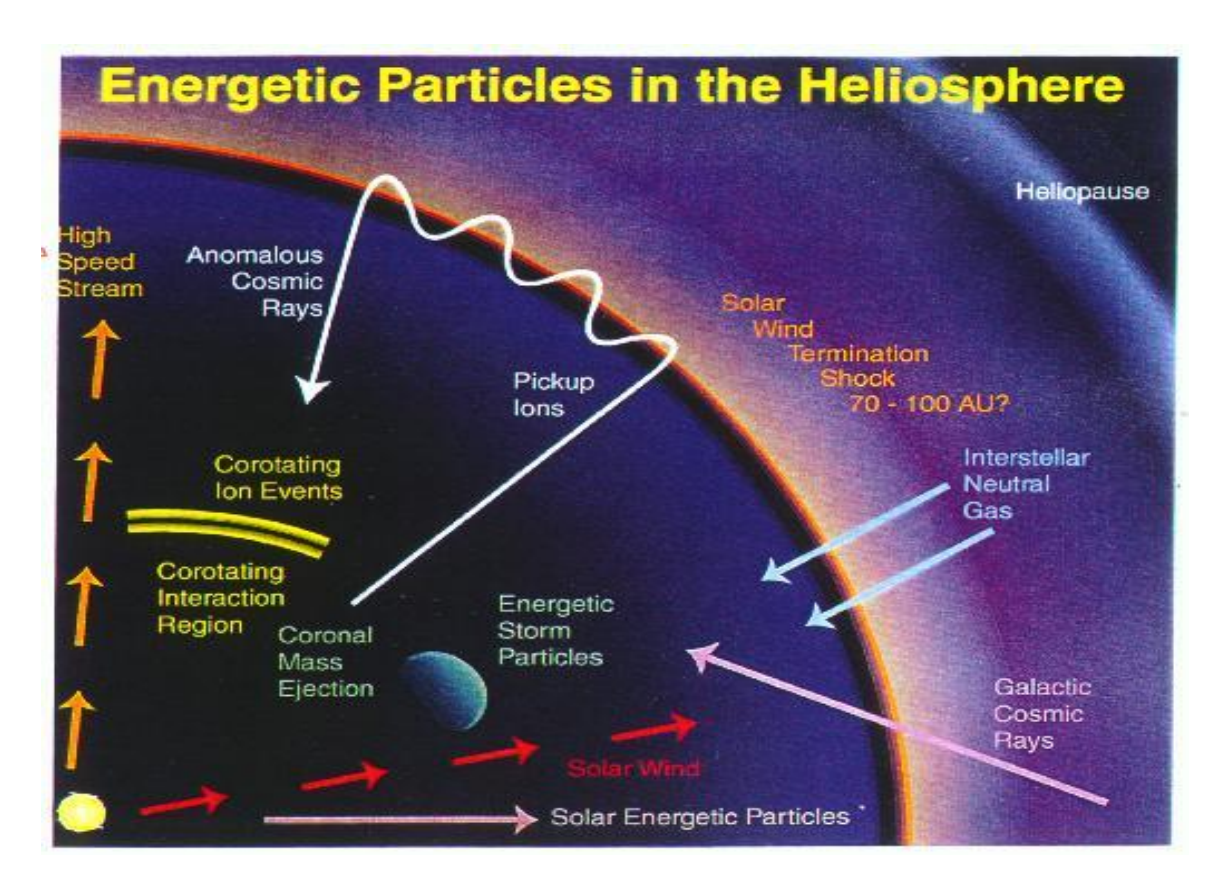


Figure 2.7 Solar Energetic Particle Mechanism [34]

There are 2 mechanisms for the propagation of solar energetic particles (Reames 1990). First mechanism is related with type III solar flares. Particles produced with this way contains mostly coronal ions. There are also electrons with high flux values (Miller 1993). This mechanism sometimes referred as first-order Fermi acceleration.

Second mechanism is valid for solar energetic particle events with high fluxes, and they are produced at the gradual injection stage. These kinds of events are seen when a great CME even happens (Kahler 1992).

The terms impulsive and gradual originally came from the time scales of the associated x-ray events, but nowadays they are applied to distinguish the time scales of SEP events. In fact, the time profiles of impulsive and gradual SEP events look rather different. The gradual event is due to an erupting filament as a part of a CME, with no accompanying flare. The impulsive events were associated with several impulsive flares, but without any CME signatures. The gradual event is dominated by protons, with a small peak at shock passage. The smooth and extended time profile comes from continuous acceleration at the moving CME shock. In the impulsive event the electron

fluxes are higher than those of the protons and those of the gradual event, respectively. The comparatively short duration of the impulsive event is determined by scattering of the particles as they traverse interplanetary space.

There is an important implication with respect to space weather effects: The direct injection of impulsive SEPs affects only a narrow regime in space. But the shock fronts driven by CMEs can extend over large spatial angles and thus can fill them with high fluxes of SEPs (Simmett, 2003). In particular, the very big and fast events produce the highly relativistic and most dangerous particles and spread them almost all around the Sun, covering nearly the whole heliosphere [35].

There is a vast literature on the important issue of elemental abundances in SEP fluxes. Most impulsive flares show not only substantial enhancements of the ³He/⁴He ratio but also enhanced heavy ion contents, as compared to oxygen (Reames and Ng, 2004). It is thought that these anomalies contain information on the acceleration and propagation processes.

SEP charge states represent the temperature of the source plasma, then charge states can be used to determine where these particles are coming from in an event. However, there might be non-thermal processes that occur during acceleration that might render the observed charge state different from its thermal value. A signature of such a process might be a charge state that changes with the particle energy [36].

For SEP events, current research models based on magnetohydrodynamics (MHD) and particle acceleration will be developed further to improve the modelling of particle acceleration in interplanetary shocks, and their associated foreshocks (upstream turbulence). The improved models will better predict the peak intensity, fluence, and energy spectrum of SEPs.

Solar energetic particles can be seperated into 3 part; Protons, electrons and neutrons.

2.2.1 Solar Protons

A Solar proton event occurs when protons emitted by the Sun become accelerated to very high energies during a solar flare accompanied by a coronal mass ejection or in interplanetary space by the shocks associated with coronal mass ejections. They can have energies of 30 MeV or more. These high energetic protons can exceed the limit of 10^{10} cm⁻² flux [37]. According to NOAA (Space Weather Prediction Center), the start of

a proton event is defined when three consecutive proton fluxes are recorded at a rate greater than or equal to ten particle flux units (pfu), where one pfu is a rate of one particle per square centimeter of detector area per steradian of solid angle scanned per second of time. The end of a proton event is the last instance the rate is above 10 pfu. This definition accounts for multiple proton flares or interplanetary shock increases within one proton event.

Particles accelerate with the help of the shock waves. As a result they show a back-forth intense distribution. As the intensity of waves goes up, particles also may be stuck in these waves. This causes particles to gain even more energies (Lee 1983, 1997). These shock waves are all produced by solar protons (Tylka 1999).

Protons are getting away from the shock waves also produce Alfvén Waves. As a consequence the particles following protons are scattered. This is the most important aspect of the current limit (Reames and Ng 1998).

As the shock waves become distant to the Sun, their power damps down, and the SEP energy spectra goes up. However, the energy of protons which are stuck in the waves may still have peak values. CME's velocity is the most important parameter to define the proton energy (Kahler 1984).

Of the solar proton events, one on 4 August 1972 was the largest on record, these kind of solar proton event occur roughly once a decade. It is hard to forecast these events. Existing models can achieve this with a 33% false alarm rate so far (Reames 2002).

Large solar proton events (SPEs), while fairly uncommon, can cause severe radiation damage to spacecraft, because they excite protons and heavy ions to high energy levels capable of penetrating surrounding structures and shielding of satellite electronics. The energy levels required for this form of penetration are approximately 50–100 MeV/nucleon, however particles at 10 MeV can also contribute to surface charging and SEUs [38].

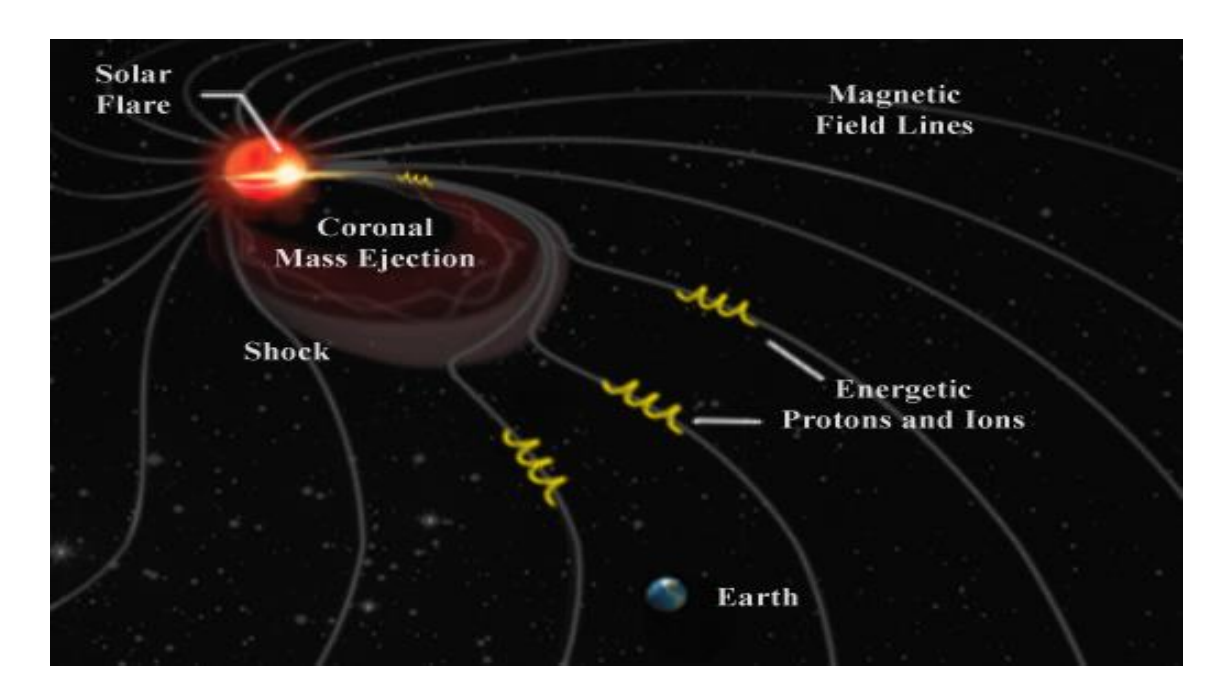


Figure 2.8 Solar energetic protons emitted by the Sun become accelerated to very high energies. Energetic protons and ions are finally guided by the interplanetary magnetic field lines [39].

Earth is largely protected by its magnetic field, or magnetosphere. However, the closer a spacecraft (or aircraft) approaches the polar regions, the greater the exposure to energetic proton radiation will be.

Depending upon the observer's longitude relative to the originating solar event, several intensity profiles that range from magnetically well-connected to poorly-connected solar energetic proton (SEP) events are possible (Reames, 2004).

High-energy protons can penetrate the Earth's magnetic field at the poles, crash into neutral atmospheric particles, and produce ion and electron pairs that temporarily increase the plasma density in the lowest regions of the ionosphere. This causes absorption of short-wave radio signals and widespread blackout of communications, sometimes called a polar cap absorption event [40].

Energetic proton storms can electrically charge spacecraft to levels that can damage electronic components. Solid memory can be altered. Flashes and streaks of light occur when energetic protons strike the sensitive optical electronics in spacecraft and can also destroy the efficiency of the solar. In addition, hazardous levels of high-energy particle radiation build up in the magnetosphere; this radiation can damage spacecraft microelectronics and pose a serious threat to the safety of astronauts. They can cause

increased noise in photonics, total radiation dose problems, power panel damage, and single event upsets [41].

2.2.2 Low Energetic Solar Electrons

Low energy solar particles are frequently emitted from the Sun, especially non-relativistic electrons which commonly originate in small a importance from flares or subflares. Electrons up to $\sim 10^8$ eV in energy have been observed (Datlowe, 1971) from larger flares. Energetic electrons appear to contain the bulk of the flare energy in those flares where they are accelerated (Lin and Hudson, 1971), and they are responsible for most of the observed flare energetic x-ray and radio emissions.

Low frequency radio observations from spacecrafts have provided a way of tracing these electrons from the vicinity of the Sun to and beyond the orbit of the Earth (Fainberg 1972).

Table 2.4 Low Energetic Solar Electron Events in an Active Year [42]

Number of Solar Flares	~16000
Number of Non-Relativistic Electron Events	~400

The possibility of following non-relativistic solar electrons, through x-ray and radio observations at the Sun, low frequency radio emission in the interplanetary medium, and direct observations at 1 AU, make these particles particularly suitable for the study of three process basic to energetic particle phenomena in the universe. There are:

- (1) The acceleration of particles in tenuous plasmas.
- (2) The propagation of energetic charged particles in disordered magnetic fields.
- (3) The interaction of energetic charged particles with tenuous plasmas to produce electromagnetic radiation.

Non-relativistic ~5-100 keV electrons constitute the bulk of the total flare energy in many small solar flares. Thus to a first approximation those flares can be thought of as a

mechanism to convert the available energy, presumably contained in the magnetic field, into energetic electrons. These particles can produce the other flare emissions –soft and hard x-ray, EUV, radio and optical emissions –by their interactions with the solar atmosphere and solar magnetic field.

Some of the low energetic electrons are released into the interplanetary medium. Here their propagation may be substantially different from that of energetic nucleons and relativistic electrons. While these latter two particle species generally propagate diffusively through the medium, the non-relativistic electrons often exhibit essentially 'scatter-free' propagation. This variability in behavior of the non-relativistic electrons can be related to spectrum of the magnetic irregularities at those wavelengths corresponding to the gyroradii of these electrons. As the electrons propagate outward from the Sun they interact with the ambient plasma, and produce plasma waves which in turn generate solar type III radio bursts [43].

For the electrons exciting type III bursts the transport is governed chiefly by beamplasma interactions involving electron-Langmuir wave interactions. For the electrons exciting type III bursts the transport is governed chiefly by beam-plasma interactions involving electron-Langmuir wave interactions. This process is fast and the characteristic length of interaction or Langmuir wave generation by electrons with velocity v and electron density n(v) scales as $\sim v n_p/[\omega_{pe} n(v)]$, where ω_{pe} is the electron plasma frequency and n_p is the plasma density. The complicating aspect of the electron transport and Langmuir wave interaction is that Langmuir waves are effectively scattered and refracted by plasma density fluctuations. This results in a fast change of Langmuir wave spectrum, which in turn affects the overall evolution of the electron stream travelling from the Sun to the Earth. Historically, simulations have been used to model the processes of electron beam generation of Langmuir waves as well the role of density.

Recently Reid and Kontar (2010), Kontar and Reid (2009) have shown that because of the inhomogeneous plasma of the solar wind, the spectral break in the peak flux and fluence appears as the electrons travel from the Sun to the Earth. As a result, the electron flux spectrum (peak and fluence) at 1 AU appears close to a broken power-law with a typical spectral index below the break around -2. Importantly, the exact value is dependent on the level of density fluctuations, so that the spectral index of electrons below the break is higher for a higher level of density fluctuations. Above the break the

electron spectrum is weakly affected by the Langmuir waves, so can be considered as 'scatter-free' transport. However, these electrons are scatter-free only in respect to Langmuir waves and could be affected by other plasma waves. The simulations suggest that the suppression of Langmuir waves changes the electron beam transport. However, the detailed evolution of the electron spectra from the Sun to the Earth has not been performed. The question of electron transport and associated Langmuir waves in the inner heliosphere becomes particularly important in the view of anticipated observations by ESA's Solar Orbiter and NASA's Solar Probe Plus[44].

The non-relativistic electrons are energetic enough to penetrate the craft's surface. But the cumulative effect of these charges on the surface of the craft may create arcing or a breakdown discharge [45].

The midnight to dawn sector is a favored region for surface charging-induced anomalies. A potential sufficient for discharge is easily created when the satellite emerges into sunlight, which results in positive surface charge due to photoelectron emission. The basic solution to differential charging problems is to provide a common ground for the spacecraft surface including internal structures. Spacecraft in geosynchronous orbit are more likely to undergo differential charging. However, use of a high-voltage power system in a low earth orbit satellite can increase the adverse environmental effects [45].

2.2.3 High Energetic Solar Electrons

It has been shown conclusively that electrons have been accelerated to relativistic energies by the solar flare and CME processes. Particles accelerated at or near the Sun are also observed by detectors on spacecraft in interplanetary space. These observations have led to the identification of two classes of acceleration events, impulsive and gradual. Among the various characteristics of the two classes, the composition of the accelerated particles is perhaps the most important. The impulsive events exhibit large enhancements of relativistic electrons relative to MeV protons, of 3He relative to 4He and of heavy ions (particularly Fe) relative to the C and O. In contrast, the gradual events have smaller electron-to-proton ratios (e/p), and their heavy ion abundances and 3He-to-4He ratios are similar to coronal values [46].

Relativistic electrons with the energies > 300 keV, emit also gyrosynchrotron emission because of the interaction of their motion with the magnetic field, which is observable in microwaves. Such microwave emission is often seen cospatially with flare loops,

with high frequencies closer to the footpoints (because of the higher magnetic field). In summary, most coherent and incoherent radio emission observed in flares is caused inone way or the other by non-thermal electrons and thus represents an important diagnostic of particle dynamics in flare plasmas.

The population of relativistic electrons is known to be closely related to the occurrence of high-speed ($V \ge 600 \text{ km s}^{-1}$) solar wind streams and often shows a periodicity of 27 days. Since high-speed solar wind can be associated both with CMEs and with the cyclical development of solar coronal holes, their occurrence is temporally associated with the 11 year solar cycle. The maximum frequency of energetic electrons develops during the declining sunspot phase, but even near solar maximum conditions, very strong relativistic electron events appear in association with coronal mass ejections and the related magnetic clouds interacting with the Earth's magnetosphere. A dramatic example is the event of 24 March 1991, when a strong interplanetary shock struck the Earth's magnetosphere and generated several orders of magnitude increases in the fluxes of multi-MeV electrons and protons in the inner magnetosphere. These results provide support for and strengthen the suggestion that relativistic electron precipitation may significantly influence the photochemical state of the middle atmosphere [47].

Previous studies of solar electrons have made it possible to build a model to predict with a moderate success the relative times of arrival of different energy electrons and protons from certain solar flares which occur at a favorable west longitude on the solar disc. These solar events characterized by a sharp increase in the relativistic electron and near relativistic proton intensities over a period of around one hour for the electrons, (slightly longer for protons), with the onset typically less that one hour after the flare onset. There is velocity dispersion at the onset of the event, with higher velocity particles preceding those with lower velocities [48].

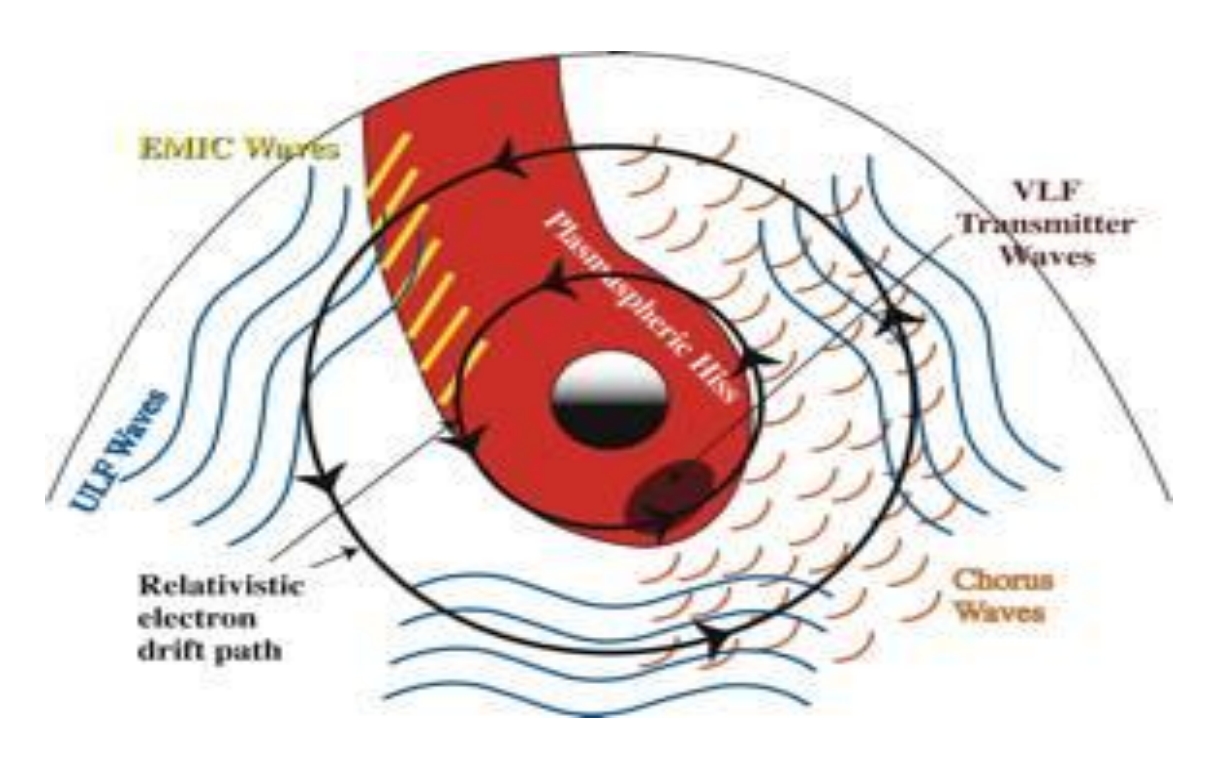


Figure 2.9 A schematic of how relativistic electron paths pass through various plasma wave regions over the course of a drift period. The inner drift path will experience mostly loss processes, while the outer drift path encounters a mixture of acceleration and loss processes (Summers, 1998).

Relativistic electrons can resonate with higher-frequency ULF waves in the period range of 1–10 seconds. The largest source of these oscillations is in the region of ring current–plasmasphere overlap of the Earth. Here the conditions are right for electromagnetic ion cyclotron (EMIC) waves to be strongly enhanced. These EMIC waves can alter a radiation belt electron's direction of motion, expanding the bounce path until it reaches the upper atmosphere. This results in a large but localized loss of particles. Waves in the extremely low frequency (ELF; 3 hertz to 3 kilohertz) and very low frequency (VLF; 3-30 kilohertz) ranges can also resonate with the relativistic electrons. On the nightside of dawn, they are typically confined to near-equatorial latitudes, and their resonant interaction with relativistic electrons is primarily manifested as an energy diffusion process. This process results in a net acceleration of the radiation belt electrons as they drift through this region, and is considered a major candidate for local acceleration of relativistic electrons in the outer zone. On the daytime side of dawn, chorus waves typically occur away from the magnetic equator, and the resonant interaction with the relativistic electrons is dominated by diffusion in the direction of motion. As with EMIC waves, this is a loss process, resulting in

electrons being dumped into the upper atmosphere. So the same type of plasma wave can be a source or loss of relativistic electrons, depending on where and when the electrons interact with the particles [49].

2.3 Galactic Cosmic Radiation

The existence of galactic cosmic rays (GCRs) has been known since 1912 when Victor Hess took an electrometer to a high altitude in a hot air balloon. Contrary to what was expected, the electrometer discharged more quickly at higher altitudes, leading Hess to conclude that the source of the discharge must be from above the atmosphere rather than the Earth itself.

Approximately 98 per cent of these particles are nucleons (protons and neutrons in nuclei without their electrons) and the remaining 2 percent are electrons and their positive counterparts, positrons. Of the particles in the energy range, 10^8 - 10^{10} eV, 87 per cent are hydrogen nuclei (protons), 12 percent are helium nuclei (also called alpha particles), and 1 percent are heavier nuclei. GCRs are slightly underabundant in hydrogen and overabundant, by several orders of magnitude, in the light elements, Li, Be, and B. Moreover, CRs are highly underabundant in electrons since, for a normal plasma, there should be approximately equal numbers of protons and electrons. Thus, the admixture of CR particles is quite different from what is normally seen in the Solar System [50].

To accelerate CR particles requires a source or sources of very high energy, possibilities including shock waves associated with supernovae, massive stellar winds, neutron stars, regions around black holes, active galactic nuclei, g-ray bursts, and others. Even when the most powerful of sources are considered, accelerating particles to Lorentz factors of order 10¹¹ (E~10²⁰ eV) strains the limits of known acceleration mechanisms. Aside from the problems of corrections for the atmosphere, interstellar medium (ISM) interactions and subsequent energy losses with spectral steepening, there is an additional problem in simply identifying the locations of the sources. Cosmic rays easily scatter from magnetic field lines in the galaxy (except at very high energy) and therefore propagate by diffusion, similar to the way a photon would take a random walk out of the Sun. Therefore, even if the angle at which a particle impinges on the Earth can be determined, it will not represent the true direction of the source. There are some energy ranges, however, for which the origin of CRs is thought to be understood [50].

The GCR energy spectrum near Earth's orbit peaks in the energy per mass 1-10 GeV/nucleon. The integral intensity of GCR particles with energy>100 MeV is about 1,1 cm⁻²-s⁻¹. There is moderately strong (5-10%) (Daniel N. Baker 2000). When the primary cosmic ray reaches earth, the ray hits the atmospheric nuclei and nuclei splits. Thus the secondary particles are developed. Some of these secondary particles decay and some of them keeps colliding with the atmospheric nuclei. This chain reaction originates sub-atomic particles such as pions, muons and neutrinos. The secondary rays are responsible for the one-third radioactivity on the Earth.

Below about 1 GeV, CGR spectra becomes much flatter. The arrival of these low energy cosmic rays is correlated with Solar activity, indicating that these particles originate from the Sun. At higher energies, CRs are believed to come from outside of the Solar System with the bulk of the particles originating from sources within the Milky Way. Energetically, ordinary stars or isolated neutron stars in the Milky Way cannot account for the total flux of these higher energy CRs. Supernovae, however, provide sufficient energy. The detection of synchrotron radiation, which is emitted by the electron component of CRs, in supernova remnants in the Milky Way provides a further link, as does the detection of TeV g-rays from supernova remnants. A supernova origin also connects CRs with hot, massive metal-enriched stars since these are the only kinds of stars that produce supernovae and can also account for the underabundance of hydrogen [50].

During a high solar activity, the emissions of matter and electromagnetic fields from the sun make harder for GCRs to reach near-Earth space. Thus the intensity of GCRs is lower, and during the solar minimum one can expect to see the intensity of GCRs will go higher. Earth's magnetic field is the main shielding source against GCRs. However GCRs have free access over the polar regions due to the magnetic field lines are open to interplanetary space. Thus, spacecrafts, orbiting over the polar regions are facing an increased danger level (Daniel N. Baker, 2000).

Most importantly GCRs consists highly ionizing, relatively abundant Fe nuclei, which may yield results of single event upsets (SEU) (Daniel N. Baker 1999).

2.4 Van Allen Radiation Belts

The Earth's radiation belts are two concentric doughnuts of plasma that encircle our planet. They tend to fill in the inner magnetosphere. There, the magnetic field generally reflects that of a classic dipole. The inner torus covers an altitude between 700 and 10,000 kilometers above the Earth, while the outer torus is larger, extending about 13,000–65,000 kilometers above the Earth. Both contain particles ionized by cosmic rays and solar flares, with the latter sometimes causing considerable changes in radiation belt particle flux as a result of the flares inducing intense geomagnetic storms. While the radiation belts exist at the highest energies of the spectrum, the plasmasphere and ring current are lower-energy charged particle populations coexisting in the inner magnetosphere, in the electron volt and kiloelectron volt ranges, respectively. The plasmasphere dominates the mass content of the inner magnetosphere and the ring current dominates the energy content of this region, and therefore both play a special role in governing radiation belt physics.

Radiation belt particles move quickly. Electrons in the outer zone, for instance, circle around the belt's local magnetic field in a few milliseconds. They also bounce back and forth as they become trapped along the belt's magnetic field lines with a period of a few seconds or less. Finally, they drift across the local magnetic field direction in an eastward flow around the Earth, making a complete drift orbit in a few to a few tens of minutes (Roederer, 1970). A magnetic field change that is slow compared with the drift motion yields a reversible increase or decrease in particle energy, following the adiabatic invariant relationships. During geomagnetic storms, the inner magnetospheric field inflates, and the drift paths correspondingly expand outward. This influence is known as the "Dst effect" (Kim and Chan, 1997), so named because the field inflation tracks the disturbance stormtime index, Dst. This process causes the radiation belt fluxes to undergo a predictable and repeatable decrease and subsequent increase during geomagnetic storms.

This is not the only process at work, however. Throughout a geomagnetic storm, several source terms combine to enhance the radiation belts, while a variety of loss mechanisms simultaneously compete to suppress the radiation belt intensity. The balance is not always equal, and (Reeves, 1998) showed that roughly half of geomagnetic storms result in a flux increase, and the other half are about evenly split between a flux decrease and roughly no change from the prestorm flux intensity. Some of these source and loss

terms are due to large-scale reconfigurations of the magnetosphere, while others are due to the interaction of the particles with plasma waves (oscillations in the magnetospheric electric and magnetic fields). In addition, the radiation belts include energetic ions as well as electrons, and some of these processes are important for one or the other type of particle [51].

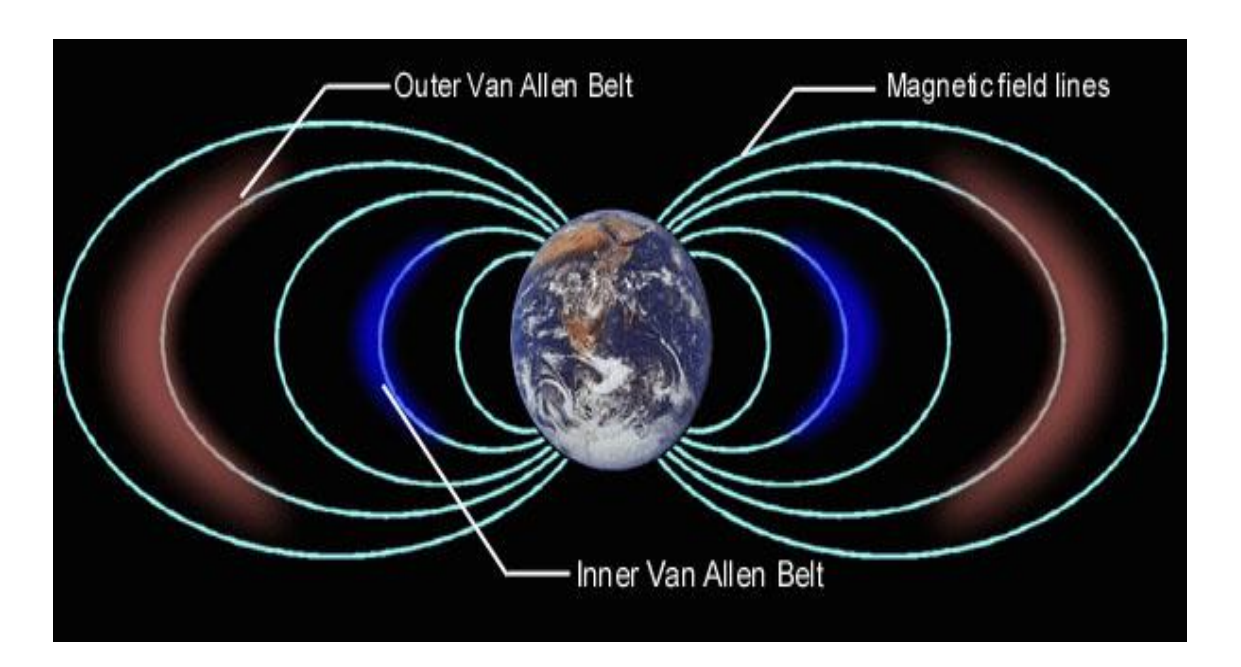


Figure 2.10 Van Allen Radiation Belts [52]

It is generally understood that the inner and outer Van Allen belts result from different processes. The inner belt, consisting mainly of energetic protons, is the product of the decay of so-called "albedo" neutrons which are themselves the result of cosmic ray collisions in the upper atmosphere. The outer belt consists mainly of electrons. They are injected from the geomagnetic tail following geomagnetic storms, and are subsequently energized through wave-particle interactions.

In the inner belt, particles are trapped in the Earth's nonlinear magnetic field, that originate from the sun. Particles gyrate and move along field lines. As particles encounter regions of larger density of magnetic field lines, their "longitudinal" velocity is slowed and can be reversed, reflecting the particle. This causes the particles to bounce back and forth between the Earth's poles [53]. Globally, the motion of these trapped particles is chaotic [54].

A gap between the inner and outer Van Allen belts, sometimes called safe zone or safe slot, is caused by the very low frequency (VLF) waves which scatter particles in pitch angle which results in the gain of particles to the atmosphere. Solar outbursts can pump particles into the gap but they drain again in a matter of days. The radio waves were originally thought to be generated by turbulence in the radiation belts, but recently it has been suggested that they are actually generated by lightning within the Earth's atmosphere.

SPACE WEATHER INDEXES

Scientific researches and the recent technological developments have shown that the dynamic conditions of space weather affect the satellite's performance and life spans, Even though it is indirectly these conditions also have effects on ground based systems. It is obviously crucial to predict these effects and potential threats before they take place in order to prevent great losses.

Space Weather Prediction Center (SWPC) identifies several parameters for terrestrial meteorology. These include temperature, pressure, wind speed and direction, and precipitation. These values change with time and place. Averages of these values help to judge climate trends and overall conditions, and the state of the space environment.

3.1 Solar Radio Flux (SRF)

These radio waves are generated through the coronal plasma which is trapped by the magnetic fields over the Sun's active zones. The F10.7 index is a measure of the solar radio flux per unit frequency at a wavelength of 10.7 cm, near the peak of the observed solar radio emission. F10.7 is often expressed in SFU or solar flux units (1 SFU = 10^{-22} W m⁻² Hz⁻¹). It represents a measure of diffuse, nonradiative heating of the coronal plasma trapped by magnetic fields over active regions. It is an excellent indicator of overall solar activity levels and correlates well with solar UV emissions [55].

The 10.7cm Solar Flux, i.e., the solar flux density at 10.7cm wavelength is measured using two fully automated radio telescopes (called Flux Monitors), located at the Dominion Radio Astrophysical Observatory. The two instruments record the strength of

the solar radio emission at 10.7cm wavelength each day for as long as the Sun is above the horizon. In addition, the instruments interrupt the continuous monitoring each day to make three precise measurements of the solar flux density. These measurements constitute the 10.7cm Solar Flux index [56].

3.2 K-Index

The K-index quantifies disturbances in the horizontal component of earth's magnetic field with an integer in the range 0-9. It is derived by Julius Bartel in 1938 from the maximum fluctuations of horizontal components observed on a magnetometer during a three-hour interval [57].

It is the general planetary index, which is used for describing the geomagnetic environment quantitatively. Kp scales from 0-9 where level-9 is the highest level of severity. Each Kp rank refers to a Dst level and it is formed by averaging the horizontal component of the geomagnetic field.

The K-index is a code that is related to the maximum fluctuations of horizontal components observed on a magnetometer relative to a quiet day, during a three-hour interval. The conversion table from maximum fluctuation (nT) to K-index, varies from observatory to observatory in such a way that the historical rate of occurrence of certain levels of K are about the same at all observatories. In practice this means that observatories at higher geomagnetic latitude require higher levels of fluctuation for a given K-index.

Table 3.1 The Conversion Table for the Boulder Magnetometer [58]

K	nT
0	0-5
1	5-10
2	10-20
3	20-40
4	40-70
5	70-120
6	120-200
7	200-330
8	330-500
9	>500

The K index is a "quasi logarithmic" number and as such cannot be averaged to give a longer-term view of the state of the Earth's magnetic field. Thus was born the A index, a daily average. At each 3-hour increment the K index at an observatory is converted to an equivalent "a" index, and the 8 a-index values are averaged to produce the A index for that day. It can vary up to values around 100. During very severe geomagnetic storms it can reach values of up to 200 and very occasionally more. The A index reading varies from one observatory to the next, since magnetic disturbances can be local. To overcome this, the indices are averaged over the globe to provide the Ap index, the planetary value [59].

Table 3.2 K-index equivalent of a-index [58]

K	a
0	0
1	3
2	7
3	15
4	27
5	48
6	80
7	140
8	240
9	400

The official planetary Kp index is derived by calculating a weighted average of K-indices from a network of geomagnetic observatories. The Space Weather Prediction Center calculates a near real-time estimates of the Kp index using a method described The network of contributing stations are possible through the cooperative efforts between SWPC and data provider partners which currently include the U.S. Geological Survey, the British Geological Survey, the Institut de Physique du Globe de Paris, and the Korean Space Weather Center. Ongoing development work and negotiations are in progress which will augment the network to include contributions from the Geoscience Australia and the Geological survey of Canada.

The Kp scale is a reasonable way to summarize the global level of geomagnetic activity, but it has not always been easy for those affected by the space environment to understand its significance. The NOAA G-scale was designed to correspond, in a straightforward way, to the significance of effects of geomagnetic storms.

Table 3.3 Average Kp to determine Geomagnetic Storm Level [59]

Kp-index	NOAA Space Weather Scale Geomagnetic Storm Level		
Kp=5	G1		
Kp=6	G2		
Kp=7	G3		
Kp=8	G4		
Kp=9	G5		

3.3 Dst Index

The Dst or disturbance storm time index is a measure of geomagnetic activity used to assess the severity of magnetic storms. It is expressed in nanoteslas and is based on the average value of the horizontal component of the Earth's magnetic field measured hourly at four near-equatorial geomagnetic observatories. Use of the Dst as an index of storm strength is possible because the strength of the surface magnetic field at low latitudes is inversely proportional to the energy content of the ring current, which increases during geomagnetic storms. In the case of a classic magnetic storm, the Dst shows a sudden rise, corresponding to the storm sudden commencement, and then decreases sharply as the ring current intensifies. Once the interplanetary Magnetic Field (IMF) turns northward again and the ring current begins to recover, the Dst begins a slow rise back to its quiet time level. The relationship of inverse proportionality between the horizontal component of the magnetic field and the energy content of the ring current is known as the Dessler-Parker-Sckopke relation. Other currents contribute to the Dst as well, most importantly the magnetopause current. The Dst index is corrected to remove the contribution of this current as well as that of the quiet-time ring current [60].

Dst equivalent equatorial magnetic disturbance indices are derived from hourly scalings of low-latitude horizontal magnetic variation. They show the effect of the globally symmetrical westward flowing high altitude equatorial ring current, which causes the "main phase" depression worldwide in the H-component field during large magnetic storms. A negative Dst value refers to a magnetic storm in progress. It becomes more

negative as the intense of the magnetic storm grows, because the number of low energy ions and electrons increases at the magnetosphere.

Hourly H-component magnetic variations are analyzed to remove annual secular change trends from records of a worldwide array of low-latitude observatories. A cosine factor of the site latitude transforms residual variations to their equatorial equivalents and harmonic analysis isolates the term used as the Dst index [58].

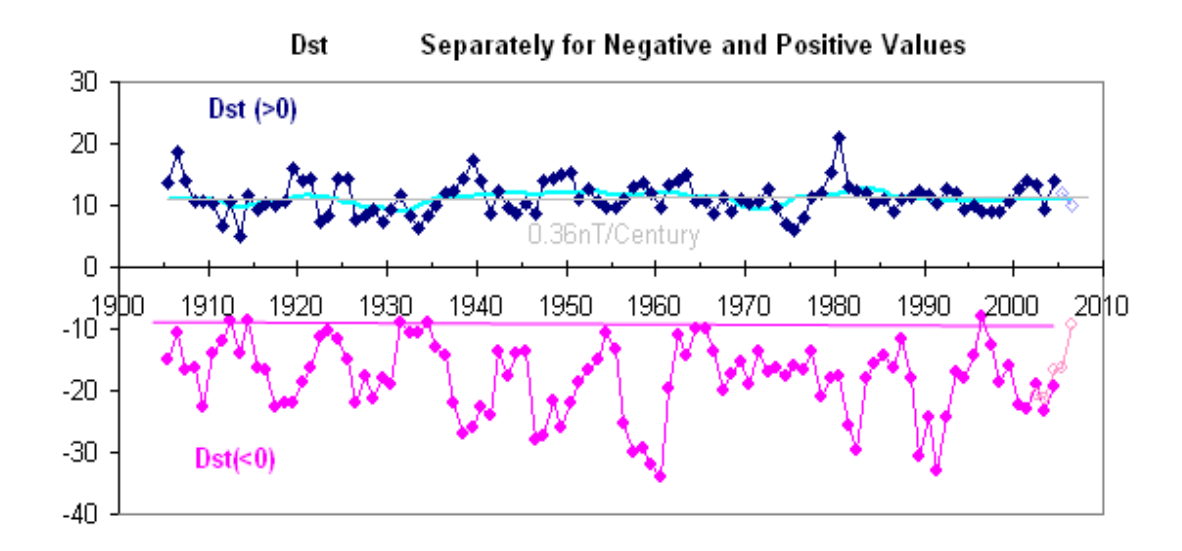


Figure 3.1 Dst Values Since the Year 1900 [61]

3.4 Geomagnetic Storms

Geomagnetic storms are major disturbances of the magnetosphere that occur when the IMF turns southward and remains southward for an prolonged period of time. The dayside magnetopause is eroded, and the associated magnetic flux is transported to the tail lobes. The plasma sheet thins, and the tail current moves earthward. A connected pair of X- and O- type neutral lines form a bubble of plasma in the plasma in the plasma sheet. This bubble is disconnected and pulled out of the center of the tail. The extra flux in the lobes reconnects earthward of the bubble and converts back to the dayside. Particles energized at the x-line are injected into the inner magnetosphere and drift in the radiation belts. Eventually the near-earth portion of the x-line moves tailward, establishing a distant x-line. These events constitute the three phases of a substorm as seen in the magnetosphere [62].

An isolated substorm is created by a brief (30-60min) pulse of southward IMF. When the IMF remains southward for longer times, activity becomes more complex. There is a series of overlapping auroral-zone activations, each injecting particles into the inner magnetosphere. The injected particles drift in a ring around the Earth. Protons drift westward, and electrons eastward, creating a westward current called the ring current. Some particles from each activation are accelerated by drift across the enhanced magnetospheric electric field. The stronger the electric field, the greater energy and the closer ring current is to the Earth. In addition, particles are accelerated out of the ionosphere into the equatorial plane, so that heavy ions such as oxygen become important in the ring current. The ring current causes large decreases in the H component over most of the Earth's surface. This effect is known as a magnetic storm. As long as injection of particles continues, the ring current will grow toward some asymtotic value in which the rate of injection equals the rate of loss. The time during which the ring current is growing calle the main phase of the magnetic storm. However, as soon as the IMF weakens, or turns northward, the ring current stops growing, and the ground perturbations begin to decrease. The ground perturbations decrease principally because particles are lost from the ring current [62].

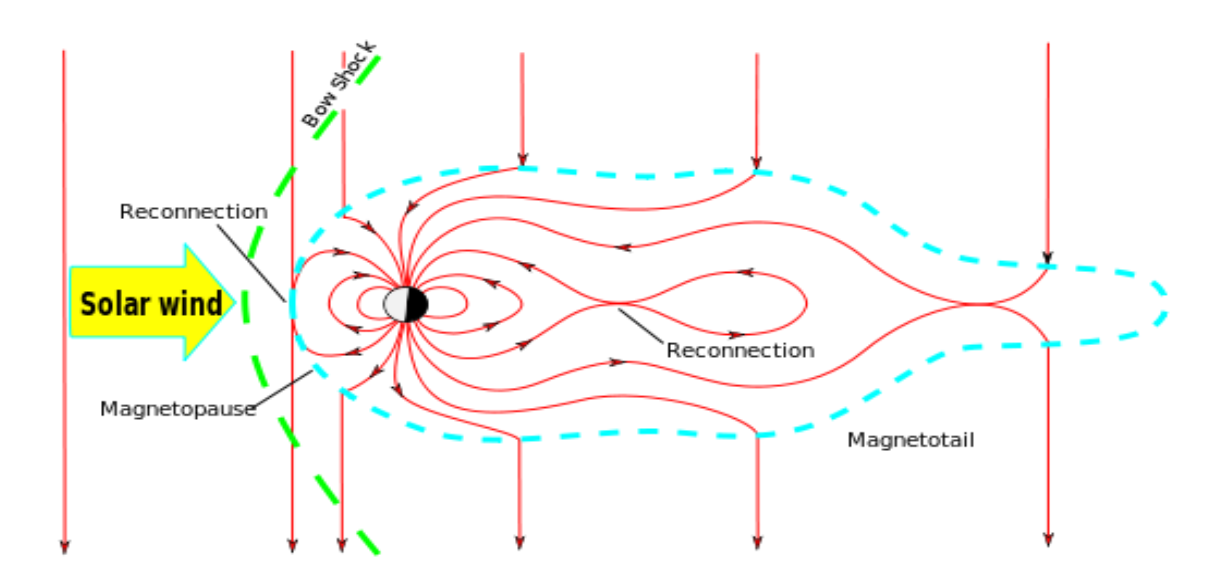


Figure 3.2 Magnetosphere in the near-Earth space environment [63]

The loss process occurs in several steps. First, the rate of dayside reconnection decreases, and the convection boundaries move to larger radial distances. The ionosphere begins to refill flux tubes within the new boundary.

As the cold ionospheric plasma encounters the ring-current plasma, ion-cyclotron waves begin to grow, and these waves scatter the ring current protons into the loss cone. Other ring current ions charge-exchange with the cold neutral hydrogen. Ring-current ions become energetic neutral atoms and are lost to the atmosphere or outer space. The low energy ions that replace them contribute little current, and so the strength of the ring current decreases with time. This is the recovery phase of the magnetic storm. Many storm recoveries occur in at least two stages. The first stage results from the rapid loss of oxygen ions, and the second from the slower loss of protons [62].

Geomagnetic storms are classified as recurrent and non-recurrent. Recurrent storms occur every 27 days, corresponding to the Sun's rotation period. They are triggered by the Earth's encounters with the southward- oriented magnetic field of the high-pressure regions formed in the interplanetary medium by the interaction of low- and high-speed solar wind streams co-rotating with the Sun. Recurrent storms occur most frequently in the declining phase of the solar cycle. Non-recurrent geomagnetic storms, on the other hand, occur most frequently near solar maximum. They are caused by interplanetary disturbances driven by fast CMEs and typically involve an encounter with both the interplanetary shock wave and the CME that drives it [64].

Category		Effect	Physical measure	Average Frequency (1 cycle = 11 years)
Scale	Descriptor	Duration of event will influence severity of effects	0.00 % 60 40	
Geo	Geomagnetic Storms		Kp values* determined every 3 hours	Number of storm events when Kp level was met; (number of storm days)
G5	Extreme	Power systems: widespread voltage control problems and protective system problems can occur, some grid systems may experience complete collapse or blackouts. Transformers may experience damage. Spacecraft operations: may experience extensive surface charging, problems with orientation, uplink/downlink and tracking satellites. Other systems: pipeline currents can reach hundreds of amps, HF (high frequency) radio propagation may be impossible in many areas for one to two days, satellite navigation may be degraded for days, low-frequency radio navigation can be out for hours, and aurora has been seen as low as Florida and southern Texas (typically 40° geomagnetic lat.).**	Кр=9	4 per cycle (4 days per cycle)
G4	Severe	Power systems: possible widespread voltage control problems and some protective systems will mistakenly trip out key assets from the grid. Spacecraft operations: may experience surface charging and tracking problems, corrections may be needed for orientation problems. Other systems: induced pipeline currents affect preventive measures, HF radio propagation sporadic, satellite navigation degraded for hours, low-frequency radio navigation disrupted, and aurora has been seen as low as Alabama and northern California (typically 45° geomagnetic lat.).**	Kp=8	100 per cycle (60 days per cycle)
G3	Strong	Power systems: voltage corrections may be required, false alarms triggered on some protection devices. Spacecraft operations: surface charging may occur on satellite components, drag may increase on low-Earth-orbit satellites, and corrections may be needed for orientation problems. Other systems: intermittent satellite navigation and low-frequency radio navigation problems may occur, HF radio may be intermittent, and aurora has been seen as low as Illinois and Oregon (typically 50° geomagnetic lat.).**	Кр=7	200 per cycle (130 days per cycle)
G2	Moderate	Power systems: high-latitude power systems may experience voltage alarms, long-duration storms may cause transformer damage. Spacecraft operations: corrective actions to orientation may be required by ground control; possible changes in drag affect orbit predictions. Other systems: HF radio propagation can fade at higher latitudes, and aurora has been seen as low as New York and Idaho (typically 55° geomagnetic lat.).**	Кр=6	600 per cycle (360 days per cycle)
G1	Minor	Power systems: weak power grid fluctuations can occur. Spacecraft operations: minor impact on satellite operations possible. Other systems: migratory animals are affected at this and higher levels; aurora is commonly visible at high latitudes (northern Michigan and Maine).**	Kp=5	1700 per cycle (900 days per cycle)

^{*} Based on this measure, but other physical measures are also considered.

Figure 3.3 Space Weather Scale for Geomagnetic Storms [58]

3.5 Solar Radiation Storms

Solar radiation storms also known as solar proton events are when protons with energies of 1–500 MeV are ejected from the Sun. Such events, although infrequent, cause substantial changes to the minor species chemistry, especially O3 and NOx, in the atmosphere between 20 and 80 km altitude. They last from a few hours up to 10 days. Relativistic electron events (energies 1–20 MeV) are also observed inside the

^{**} For specific locations around the globe, use geomagnetic latitude to determine likely sightings

magnetosphere. The sources of these very energetic particles are still unclear. There are plausible arguments suggesting that the Sun, Jupiter, the dayside cusp or the geomagnetic tail may be the source of such particles. Like the solar proton events, their atmospheric consequence may be very significant in the aerosol chemistry. Both energetic ion and electron precipitation may also affect the global electric circuit. This is the cumulative effect of all the thunderstorms which charge the ionosphere to a potential of several 100 kV with respect to the Earth's surface. This potential difference drives vertical electric currents downward from the ionosphere to the ground in regions where thunderstorms do not occur. The fair weather electric current, as it is called, varies spatially and temporally according to the ionospheric potential and the total column resistance between the ionosphere and the ground. This column resistance may vary when very energetic proton or electron events are in progress [65].

Category		Effect	Physical measure	Average Frequency (1 cycle = 11 years)
Scale	Descriptor	Duration of event will influence severity of effects		W 300 1986 18 1986
Sola	ar Ra	diation Storms	Flux level of ≥ 10 MeV particles (ions)*	Number of events when flux level was met**
S 5	Extreme	Biological: unavoidable high radiation hazard to astronauts on EVA (extra-vehicular activity); passengers and crew in high-flying aircraft at high latitudes may be exposed to radiation risk. *** Satellite operations: satellites may be rendered useless, memory impacts can cause loss of control, may cause serious noise in image data, star-trackers may be unable to locate sources; permanent damage to solar panels possible. Other systems: complete blackout of HF (high frequency) communications possible through the polar regions, and position errors make navigation operations extremely difficult.	10 ⁵	Fewer than 1 per cycle
S 4	Severe	Biological: unavoidable radiation hazard to astronauts on EVA; passengers and crew in high-flying aircraft at high latitudes may be exposed to radiation risk.*** Satellite operations: may experience memory device problems and noise on imaging systems; star-tracker problems may cause orientation problems, and solar panel efficiency can be degraded. Other systems; blackout of HF radio communications through the polar regions and increased navigation errors over several days are likely.	104	3 per cycle
S 3	Strong	Biological: radiation hazard avoidance recommended for astronauts on EVA; passengers and crew in high-flying aircraft at high latitudes may be exposed to radiation risk *** Satellite operations: single-event upsets, noise in imaging systems, and slight reduction of efficiency in solar panel are likely. Other systems: degraded HF radio propagation through the polar regions and navigation position errors likely.	103	10 per cycle
S 2	Moderate	Biological: passengers and crew in high-flying aircraft at high latitudes may be exposed to elevated radiation risk.*** Satellite operations: infrequent single-event upsets possible. Other systems: effects on HF propagation through the polar regions, and navigation at polar cap locations possibly affected.	102	25 per cycle
S1	Minor	Biological: none. Satellite operations: none. Other systems: minor impacts on HF radio in the polar regions.	10	50 per cycle

Flux levels are 5 minute averages. Flux in particles s⁻¹ ster ¹-cm⁻² Based on this measure, but other physical measures are also considered.

Figure 3.4 Space Weather Scale for Solar Radiation Storms [58]

These events can last more than one day.

High energy particle (>100 MeV) are a better indicator of radiation risk to passenger and crews. Pregnant women are particularly susceptible.

3.6 Radio Blackouts

When the geomagnetic field is abruptly changed by a magnetic cloud crashing onto it or by an interplanetary shock wave, strong electric fields are induced in large-scale electric power distribution systems. This creates radio blackouts.

Radio blackouts are caused by bursts of X-ray and Extreme Ultra Violet radiation which are emitted during solar flares and affect the sunlit side of the Earth. Radio blackouts primarily affect High Frequency (HF) (3-30 MHz) communication, although fading and diminished reception may spill over to Very High Frequency (VHF) (30-300 MHz) and higher frequencies. These effects occur on the sunlit side of the Earth and are most intense at locations where the Sun is directly overhead. These blackouts are a consequence of enhanced electron densities caused by solar flare emissions. These emissions ionize the sunlit side of Earth, which increases the amount of energy lost as radio waves pass through the upper atmosphere. Radio blackouts are the most common space weather events to affect Earth. Minor events occur about 2000 times each solar cycle. Radio blackouts are by far the fastest space weather event to impact our planet. The electromagnetic emission produced during flares travels at the speed of light taking just over 8 minutes to travel from the Sun to Earth. Radio blackouts can last from several minutes to several hours depending on the duration of the solar flare. How severe a radio blackout is depends on the strength of the solar flare [66].

Ca	Category Effect		Physical measure	Average Frequency (1 cycle = 11 years)
Scale	Descriptor	Duration of event will influence severity of effects	No. of the contract of	N N N N N N N N N N N N N N N N N N N
Rac	dio Bl	ackouts	GOES X-ray peak brightness by class and by flux*	Number of events when flux level was met; (number of storm days)
R5	Extreme	HF Radio: Complete HF (high frequency**) radio blackout on the entire sunlit side of the Earth lasting for a number of hours. This results in no HF radio contact with maniners and en route aviators in this sector. Navigation: Low-frequency navigation signals used by manitime and general aviation systems experience outages on the sunlit side of the Earth for many hours, causing loss in positioning. Increased satellite navigation errors in positioning for several hours on the sunlit side of Earth, which may spread into the night side.	X20 (2x10 ⁻³)	Fewer than 1 per cycle
R 4	Severe	HF Radio: HF radio communication blackout on most of the sunlit side of Earth for one to two hours. HF radio contact lost during this time. Navigation: Outages of low-frequency navigation signals cause increased error in positioning for one to two hours. Minor disruptions of satellite navigation possible on the sunlit side of Earth.	X10 (10 ⁻³)	8 per cycle (8 days per cycle)
R3	Strong	HF Radio: Wide area blackout of HF radio communication, loss of radio contact for about an hour on sunlit side of Earth. Navigation: Low-frequency navigation signals degraded for about an hour.	X1 (10 ⁻⁴)	175 per cycle (140 days per cycle)
R 2	Moderate	HF Radio: Limited blackout of HF radio communication on sunlit side of the Earth, loss of radio contact for tens of minutes. Navigation: Degradation of low-frequency navigation signals for tens of minutes.	M5 (5x10 ⁻⁵)	350 per cycle (300 days per cycle)
R 1	Minor	HF Radio: Weak or minor degradation of HF radio communication on sunlit side of the Earth, occasional loss of radio contact. Navigation: Low-frequency navigation signals degraded for brief intervals.	M1 (10 ⁻⁵)	2000 per cycle (950 days per cycle)

Flux, measured in the 0.1-0.8 mm range, in W·m². Based on this measure, but other physical measures are also considered.

 Other frequencies may also be affected by these conditions.

URL: www.swpc.noaa.gov/NOAAscales

April 7, 2011

Figure 3.5 Space Weather Scale for Radio Blackouts [58]

EFFECTS ON SPACECRAFTS & SATELLITES

Anytime that satellite technology or astronauts are being affected by forms of radiation in space such as fast-moving particles and X-rays, this usually causes some changes to occur. Most of the time these changes are so minor that they have no real consequences either to the way that the satellite operates, or the health of the astronaut. But sometimes, and especially during a severe solar storm or a space weather event, the conditions in space can change drastically. The term space radiation effects has to do with all of the different ways that these severe conditions can significantly change the way a satellite operates, or the health of an astronaut working and living in space.

The major obstacles to mission success remain the hazards during launch and early spacecraft deployment. Once the spacecraft is deployed and on-station, the spacecraft operator must then be vigilant against other hazards that might endanger the mission. Space weather is one of these hazards and it should be monitored to help ensure spacecraft health and to minimize outages.

Space weather effects on satellites vary according to orbit, spacecraft local time, spacecraft position relative to certain regions in space, stage of the 11-year sunspot cycle, and many other factors. Effects can range from simple upsets, that are easily recovered from, to total mission failure. Space weather is of concern to those pursuing commerce and discovery in space.

When a high-energy particle penetrates a satellites metal skin, its energy can be absorbed by microscopic electrical components in the circuitry of a satellite. The switch can be changed from 'on' to 'off' momentarily, or if the energy is high enough, this can

be a permanent change. If that switch is a piece of data in the satellites memory, or a digit in a command or program, it can suddenly cause the satellite to veer out of control until a human operator on the ground can correct this problem. If the particle happens to collide with one of the pixel elements in the satellite's star-tracking camera, a false star might be created and this can confuse the satellite to think it is not pointing in the right direction. Other satellite effects can be even more dramatic. When severe solar storms affect Earth's upper atmosphere, the atmosphere heats up slightly and expands deeper into space. Satellite will feel more friction with the air they are passing through, and this will seriously affect their orbits.

Today, engineers design satellites with space weather in mind, using radiation models to predict how much radiation a satellite may be exposed to over its lifetime. A satellite's radiation exposure may vary depending on its orbit. For instance, some orbits are more dangerous than others; engineers choose components that can survive and operate in such environments.

In this chapter various known effects on satellites and spacecrafts will be discussed.

4.1 Surface Charging

Surface charging is created from low-energy plasma and photoelectric currents. The midnight to dawn sector is a favored region for surface charging-induced anomalies. Typically, differential charging has occurred after geomagnetic substorms, which result in the injection of keV electrons into the magnetosphere. While in eclipse, the spacecraft may negatively charge to tens of kilovolts. A potential sufficient for discharge is easily created when the satellite emerges into sunlight, which results in positive surface charge due to photoelectron emission. Differential charging can also be caused by satellite self-shadowing.

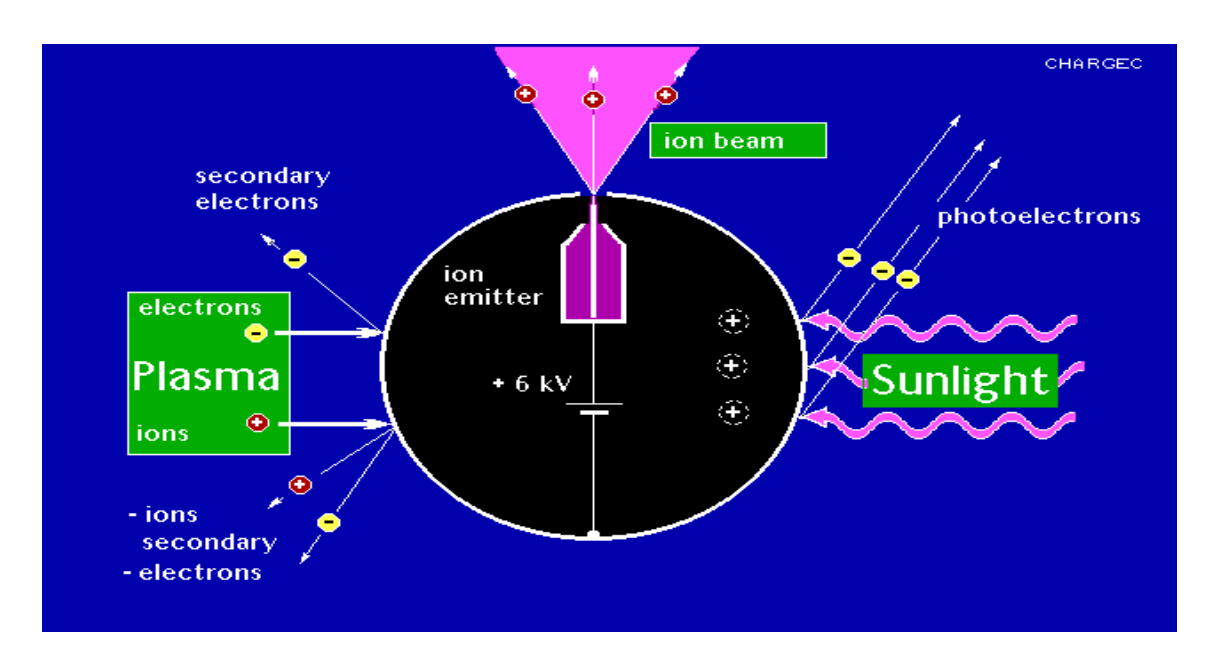


Figure 4.1 Charge control mechanism for a satellite [67]

The basic solution to differential charging problems is to provide a common ground for the spacecraft surface (including internal structures). Spacecraft in geosynchronous orbit are more likely to undergo differential charging. However, use of a high-voltage power system in a low earth orbit satellite can increase the adverse environmental effects [68].

Surface charging to a high voltage does not usually cause immediate problems for a spacecraft. However, electrical discharges resulting from differential charging can damage surface material and create electromagnetic interference that can result in damage to electronic devices. Variations in low energy plasma parameters around the spacecraft, along with the photoelectric effect from sunlight, cause most surface charging. Due to the low energy of the plasma, this type of charging does not penetrate directly into interior components. Surface charging can be largely mitigated through proper materials selection and grounding techniques.

Surface charging occurs predominantly during geomagnetic storms. It is usually more severe in the spacecraft local times of midnight to dawn but can occur at any time. Night to day, and day to night transitions are especially problematic during storms since the photoelectric effect is abruptly present or absent, which can trip discharges. Additionally, thruster firings can change the local plasma environment and trigger discharges [58].

4.2 Deep Dielectric (Bulk Charging)

Internal dielectric charging is caused by high-energy electrons penetrating dielectric materials (e.g., printed circuit boards). These high-energy electrons are more likely found trapped within the earth's Van Allen radiation belts. Normally, a fluence of 10¹⁰ - 10¹¹ electrons/cm² (over a period relative to the dielectric leakage rate) will build-up a sufficient charge for arcing. Some researchers have indicated a higher likelihood of deep dielectric charging-induced anomalies than those from surface charging and single-event upset. Leaky dielectrics, proper grounding, and shielding can be used to reduce the possibility of internal charging. In addition, EMI-susceptibility reduction techniques can be employed to mitigate the effects of arcing [69].

Bulk charging is a problem primarily for high altitude spacecraft. At times, when Earth is immersed in a high-speed solar wind stream, the Van Allen belts become populated with high fluxes of relativistic (>~1 MeV) electrons. These electrons easily penetrate spacecraft shielding and can build up charge where they come to rest in dielectrics such as coax cable, circuit boards, electrically floating radiation shields, etc. If the electron flux is high for extended periods, abrupt discharges (tiny "lightening strokes") deep in the spacecraft can occur [58].

High fluxes of these electrons vary with the 11 year solar cycle and are most prevalent late in the cycle and at solar minimum. Occasionally, high-energy electron events recur with a 27-day periodicity - the rotation period of the Sun. Discharges appear to correlate well with long periods of high fluxes. At these times, charge buildup exceeds the natural charge leakage rate of the dielectric. The charge builds and discharge occurs after the breakdown voltage is reached. In the past, some energetic electron enhancements at GEO have approached two weeks in duration. It was at the end of one of these long duration enhancements in 1994 that two Canadian satellites experienced debilitating upsets [58].

The fact that the explanation given here for internal charging is shorter than that for surface (differential) charging should not be indicative of the relative importance of the two. In fact, just the opposite, internal discharge is more damaging since it occurs within dielectric materials and well-insulated conductors, which are in close proximity to sensitive electronic circuitry [70]. Based on CRRES data obtained at GEO, most environmentally induced spacecraft anomalies result from deep dielectric charging and

the resulting discharge pulses and not from surface insulator charging or single-event upsets (Gussenhoven, 1996). In addition, the mechanisms for internal charging are more straightforward, high-energy electrons penetrate internal dielectric materials, and if charge buildup occurs too rapidly, then an arc discharge ensues.

High-energy (E > 100 keV) electrons may penetrate into the satellite, and establish negative potential on isolated parts such as dielectric materials and floating conductors. The electrons may become trapped (buried) in dielectric materials. The internal electric field will build up if the charge leakage rate is less than the charge collection rate. A fluence of 10^{10} - 10^{11} electrons/cm² (over a time period relative to the dielectric leakage rate) will build-up a sufficient charge for arcing [71]. The resulting arcing will appear as a pulse on the cabling and circuit board. Pulse widths are usually in the tens of nanoseconds. Also, printed circuit boards with islands of metallization will charge up like a capacitor. If a sufficient potential is reached, arcing may result in upset or burnout of nearby semiconductor devices.

The internal charging can affect insulators such as cable wrap, wire insulation, circuit boards, electrical connectors, feed throughs, etc. The likelihood of discharge is a function of both the voltage potential and the electric field.

4.3 Singe Event Upsets (SEU)

The primary cosmic rays are very energetic and are highly ionising, which means that they strip electrons from atoms which lie in their path and hence generate charge. The density of charge deposition is proportional to the square of the atomic number of the cosmic ray so that the heavier species can deposit enough charge in a small volume of silicon to change the state of a memory cell, a one becoming a zero and vice versa. Thus memories can become corrupted and this could lead to erroneous commands. Such soft errors are referred to as single event upsets (SEU) [68].

Single event upsets occur when a high-energy particle (>~50 MeV) penetrates spacecraft shielding and has the misfortune to hit a device in just the wrong way to cause disruption. This is generally a hit or miss situation. Effects can range from simple device tripping to component latch-up or failure. Particle bombardment of memory devices can also change on-board software through physical damage or through deposition of charge resulting in a "bit flip." There are two natural phenomena that

cause this type of problem - Galactic Cosmic Rays (GCRs) and Solar Proton Events (SPEs) [58].

Solar Proton Events at Earth can occur throughout the solar cycle but are most frequent in solar maximum years. SPEs result from powerful solar flares with fast coronal mass ejections. During an SPE satellites experience dramatically increased bombardment by high-energy particles, primarily protons. Fluxes of particles with energies > 10 MeV, can reach 70,000 protons/cm2/sec/ster. SEU rates increase with high fluxes since there is a higher likelihood of impact with a sensitive location. High-energy particles reach Earth from 30 minutes to several hours following the initiating solar event. The particle energy spectrum and arrival time seen by satellites varies with the location and nature of the event on the solar disk [58].

Sometimes a single particle can upset more than one bit to give what are called multiple bit upsets (MBU). Certain devices could be triggered into a state of high current drain, leading to burn-out and hardware failure; such effects are termed single event latch-up or single event burn-out. In other devices localised dielectric breakdown and rupture can occur (single event gate rupture and single event dielectric failure). These deleterious interactions of individual particles are referred to as single event effects (SEE) to distinguish them from the cumulative effects of ionising radiation (total dose effects) or lattice displacements (damage effects). For space systems SEE have become increasingly important over the last fifteen years and are likely to become the major radiation effects problem of the future. For avionics SEE are the main radiation concern but total dose can be of significance for aircrew [68].

The severity of an environment is usually expressed as an integral linear energy transfer spectrum which gives the flux of particles depositing more than certain amount of energy per unit pathlength of material. Energy deposited per unit pathlength is referred to as linear energy transfer (LET) and the common units are MeV per g.cm⁻² or per mg.cm⁻² (the product of density and pathlength). Devices are characterised in terms of a cross-section which is a function of LET. For each device there is a threshold LET below which SEE does not occur. As device sizes shrink these thresholds are moving to lower LET and rates are increasing. In addition to directly ionising interactions with electrons, particles may interact with atomic nuclei thus imparting a certain recoil energy and generating secondary particles. Both the recoiling nucleus and secondary charged particles are highly ionising so that if such a reaction occurs in, or adjacent to, a

device depletion region a SEE may result. Collisions with nuclei are less probable than collisions with orbital electrons but when certain particle fluxes are high this mechanism can dominate. This occurs in the earth's inner radiation belt where there are intense fluxes of energetic protons. It can also occur in the atmosphere where there is a build-up of significant fluxes of secondary neutrons. This mechanism is thought to be the dominant SEE hazard for current and near future avionics at most altitudes.

For radiation effects on biological systems it is found that there is a strong dependence on LET and so dose equivalents are used. Quality factors are defined to measure the enhancement in the effect compared with lightly ionising electrons or photons. These factors can be as large as 20 for heavy ions and fast neutrons. Thus for radiobiological dosimetry the charge deposition or LET spectrum must be measured, at least at coarse resolution, and summation of dose x quality factor made to give the dose equivalent, for which the SI units are sieverts (the dose equivalent of the rad is the rem, so that 1 sievert = 100 rem) [68].

4.4 Total Dose Effects

Spacecraft ages through continual bombardment by GCRs, trapped radiation, and SPEs. There are several models used to estimate the total dose expected in various orbits and at different stages of the solar cycle. These models provide total dose estimates that are helpful in estimating the lifetime of an operational satellite. The total dose a satellite receives from GCRs is relatively constant. Solar cycle variations in trapped radiation are also reasonably well modeled. SPEs are most prevalent during the solar maximum years but their time of occurrence and severity are very difficult to model.

The majority of effects depend on rate of delivery and so dose-rate information is required. Accumulated dose leads to threshold voltage shifts in complementary metal oxide semiconductor (CMOS) due to trapped holes in the oxide and the formation of interface states. In addition increased leakage currents and gain degradation in bipolar devices can occur [68].

Spacecraft components are manufactured to withstand high total doses of radiation. However, it is important for the satellite operator to know how much dose each spacecraft in his fleet has endured. This knowledge allows for reasoned replacement strategies in an industry with very long manufacturing lead times.

Spacecraft power panels are physically and permanently damaged by particles of energy high enough to penetrate their surfaces. During one large high-energy SPE, several percent of power panel output can be lost. This shortens the overall lifetime of the spacecraft or at least entails power management problems as the spacecraft nears its end of life. Recent developments in the manufacturing process have made SPEs less of a problem, but power loss still occurs in these new panels.

4.5 Solar Radio Frequency and Scintillation

The Sun is a strong, highly variable, broad-band radio source. At times, the Sun is within a side-lobe or even the main beam of a ground antenna looking at a satellite, usually pointed within about 1 degree of the Sun. If the Sun happens to produce a large radio burst during that time, the signal from the spacecraft can be overwhelmed. Large solar radio bursts occur most frequently during solar maximum years. An operator should be aware of when the Sun is in close proximity to the satellite being tracked. At times, the ionosphere becomes highly irregular causing satellite signals to band inhomogeneously when they transit this disturbed medium, and scintillate at the receiver. Strong geomagnetic storms can cause scintillation in the auroral zones.

Ionospheric scintillation is a rapid fluctuation of radio-frequency signal phase and/or amplitude, generated as a signal passes through the ionosphere. Scintillation occurs when a radio frequency signal in the form of a plane wave traverses a region of small scale irregularities in electron density. The irregularities cause small-scale fluctuations in refractive index and subsequent differential diffraction (scattering) of the plane wave producing phase variations along the phase front of the signal. As the signal propagation continues after passing through the region of irregularities, phase and amplitude scintillation develops through interference of multiple scattered signals. scintillation is problematic for signals traversing the equatorial ionosphere. In this area, large rising turbulent plumes form in the afternoon and evening ionosphere, resulting in rapidly varying, significant signal loss. Not only does this affect telemetry up/downlink but, GPS users can lose tracking of enough spacecraft so as to make location finding difficult [72].

4.6 Background Noise in Sensors

During Solar Proton Events, photonic devices such as charged couple devices (CCDs) and some star trackers experience a noise floor increase. For star trackers, this noise can result in orientation problems. Streaks and extra "photo electrons" in imaging CCDs can compromise data quality. Spurious counts are produced in many detector systems and these depend on the size distribution of individual depositions and can occur from both prompt ionisation and delayed depositions due to induced radioactivity [73].

4.7 Spacecraft Orientation

Some spacecraft use Earth's magnetic field as an aid in orientation or as a force to work against to dump momentum and slow down reaction wheels. During geomagnetic storms, dramatic unexpected changes in the magnetic field observed by the satellite can lead to mis-orientation of the spacecraft. Some effects have been reported at Kp values as low as Kp=4. Usually, problems are not experienced until Kp>=6 occurs.

GEO spacecraft also experience a unique occurrence termed a Magnetopause Crossing. The sunward boundary of Earth's magnetic field (magnetopause) is usually located approximately 10 Earth radii from Earth center. Variations in the pressure (due to changes in the velocity, density, and magnetic field) of the incoming solar wind change the location of that boundary. Under solar wind conditions of high velocity and density and strongly southward magnetic field, this boundary can be rammed to inside the altitude of GEO orbit at 6.6 Earth radii. A GEO spacecraft on the sunward side of Earth can be outside the (compressed) magnetopause and in the (modified) solar wind magnetic field for minutes to hours. When the magnetopause is inside 6.6 radii, GEO spacecraft are within the magnetosheath between the bow shock and the magnetopause. Magnetic sensors on board become confused as the detected magnetic field drops from ~200 nanoTesla to near zero and its sign changes erratically. However, since magnetopause compression is time varying, and different spacecraft are at different longitudes [58].

4.8 Faulty Hardware or Design

There is also the possibility that an anomaly may occur because of faulty hardware or software onboard the spacecraft. This cause is often coupled with the previously discussed space environment effects but may be more directly attributed to

manufacturing or design error if the hardware fails when the space environment conditions do not exceed the design specifications, or when a part is inadequately shielded for the environment in which it is meant to be placed. Such hardware or design faults may be easier to identify if anomaly investigators are aware of whether other satellites using the same hardware are experiencing similar problems, or whether there are environmental causes that may be playing a role.

4.9 Operator Error

Operator errors are anomalies caused by humans incorrectly commanding the spacecraft in a way that causes abnormal or unexpected behavior. Examples of operator error include command error, causing the satellite to take an action it was not designed to take, incorrect calculations of required thruster adjustments, reaction wheel rates, antenna pointing, power cycling, or failing to take action to "safe" the satellite when space environment conditions are known to be extremely hazardous, such as during a major geomagnetic storm. Some such storms can be predicted through observations of coronal mass ejections on the sun's surface, which are monitored by several spacecraft in Earth orbit, in orbit around the sun itself or at the Earth-Sun LaGrange point, about 1/100 astronomical unit closer to the sun than the Earth. Remote sensing observations of explosions on the sun's surface, if appropriately aligned, can provide more than a day's worth of warning before the solar plasma encounters the Earth's magnetosphere [74].

CHAPTER 5

METHODS OF ANALYSES

Satellite anomalies are mission-degrading events that negatively affect on-orbit operational spacecraft. All satellites experience anomalies of some kind during their operational lifetime. They range in severity from temporary errors in non-critical subsystems to loss-of-contact and complete mission failure. There is a range of causes for these anomalies, and investigations by the satellite operator or manufacturer to determine the cause of a specific anomaly are sometimes conducted at significant expense.

Many satellites encounter anomalous events detrimental to mission performance at some point during their operational lifetimes. These "satellite anomalies" may be as minimal as a temporary error in a noncritical subsystem, or as devastating as a complete mission failure. Hardware damage and software malfunctions, the typical manifestations of these anomalies, may occur because of a variety of causes, including faulty equipment, the hazardous natural space environment, impact with orbital debris, operator error, hostile actions by a malicious actor, or even unintentional interference from another satellite transmitter. The cause of the anomaly is typically not obvious to the satellite operators at the time of the event.

The hidden specific agents behind these anomalies are hard to be pinpointed, and are elusive. But in literature there are some techniques to overcome the situation. The techniques that were used in this study will be explained briefly in this chapter.

5.1 Superposed Epoch Approach

The superposed epoch approach (SPE) is a simple statistical analysis technique which is applied to time series. Despite being simple, the SPE is one of the powerful analysis techniques if it is used carefully. The idea was that if you average the data in some clever way in relation to an event, the event signal will remain and all other influences will tend to average out. Thus, the crucial part of applying this technique is to be able to define a proper event definition.

Having defined an event, data of a specifically designated interval were extracted from the complete dataset. Then, the selected data were superposed on each other taking the zero time as the event time. By simply dividing with the total number of identified events, results of SPE were obtained. As prescribed, if the identification of an event representing a physical process successfully made, the results would reveal dynamic component of the response, or in other words, the information containing component of the response [75].

Through simple compositing, the SEA method involves sorting data into categories dependent on a 'key-date' for synchronization and then comparing the means of those categories. Given sufficient data, a common underlying (causal) response to a forcing event should theoretically emerge in the average (composite). Examples of applications of the SEA method are widespread in various scientific fields of study.

The SEA method is simple and involves basic arithmetic calculations (averaging). However, the randomization procedure used to determine statistical significance, depending on the number of iterations performed, can be computationally demanding.

As with any statistical method, care must be taken in the application and interpretation of SEA results. For instance, the SEA can be vulnerable to leveraging resulting from the influence of a single large anomaly. This problem typically arises when the 'key date' sample size is small. To deal with this explicitly approach of this study embraced proxy data to considerably increase the number of satellite anomaly data incorporated into the SEA. This thesis also was included with a normalization step in SEA in order to provide a methodological safeguard to leveraging.

5.2 Space Weather Models

Turkish remote sensing satelite of RASAT is the first remote sensing satellite, it is a phase tester, and due to that fact to lower the initial costs, a radiation sensor hadn't been installed on the satellite. But it created some great challenges to be overcame by. Space weather elements works differently and measurements are different on each orbit, (Low earth orbit (LEO), geosynchronous orbit (GEO), high elliptical orbit-high earth orbit (HEO)).

To see the correlation with GEO and LEO data, in this study, the Space Environment Information System (SPENVIS) is used, and it is the European Space Agency's (ESA) primary tool for modeling the effect of the space environment. The system allows spacecraft engineers to perform a rapid analysis of environmental problems related to natural radiation belts, solar energetic particles, cosmic rays, plasmas, gases, magnetic fields and micro-particles. Various reporting and graphical utilities and extensive help facilities are included to allow engineers and spacecraft designers with relatively little familiarity to produce reliable results.

SPENVIS and the NASA's AE-8 Radiation Model embedded in the tool's radiation sources and effects package, are selected. AE-8 models the trapped electron flux for a given orbit or location; first geosynchronous orbit was selected. The initial properties for RASAT has been entered and tried to see if there was a correlation with the anomaly dates of RASAT. Same procedure was applied for LEO. In chapter 7 the procedure will be explained briefly.

Summer of Environment Tools of Spenvis [76];

- A Radiation belt models: particle fluxes at points in space or over an orbit.
- * Radiation effects: dose vs. shielding depth and damage-equivalent fluence for solar cells.
- Cosmic Ray Effects on MicroElectronics model (CREME): fluxes for various situations and SEU rates.
- Solar energetic protons: spectra, statistics, history and geomagnetic shielding.
- ❖ COSPAR International Reference Atmosphere model (CIRA):density and temperature as function of position, time and solar activity.

- ❖ ATOmic OXygen interaction model (ATOMOX):fluxes, fluences and erosion rates on satellite surfaces.
- ❖ JUNK meteoroid/debris model: fluxes to surfaces and damage probabilities.
- ❖ International Reference Ionosphere model (IRI):local fluxes and column density (total electron content).
- Geomagnetic substorm model and data: density, temperature and spectra.
- Plasma interactions and effects: surface charge (EQUIPOT) and sputter (SOLARC)
- ❖ Internal Dielectric Charging (DICTAT): maximum electric field and liability to electrostatic discharges
- ❖ Internal magnetic field models: magnetic field B, L parameter, geomagnetic latitude lambda, conjugate points.
- External magnetic field models: perturbations to geomagnetic field as a function of solar activity.
- ❖ Space environment data: access to OMNI database and others.
- Solar data: NOAA on-line reports, solar activity history and predictions.
- ❖ Orbit generator.

TURKISH REMOTE SENSING SATELLITE: RASAT

RASAT is the second remote-sensing satellite after the launch of Turkey's first remote sensing satellite BİLSAT of TUBİTAK UZAY. RASAT, having a high-resolution optical imaging system and new modules developed by Turkish engineers, is the first Earth-observation satellite to be designed and manufactured in Turkey.

RASAT, the first earth observation satellite designed and manufactured in Turkey, was launched from Russian Federation, and it was designed, manufactured and tested by TUBITAK Space Technologies Research Institute (TUBITAK UZAY), and the project was funded by Turkish State Planning Office (DPT).



Figure 6.1 Rasat is Ready for its Transportation to Russia [77]

RASAT project enabled development of satellite design, manufacturing and test capabilities of TUBITAK UZAY. The experience and capabilities that TUBITAK UZAY and Turkish engineers gained, pioneered Turkey to new satellite projects, to reach the targets in space technologies. In this aspect, the basic targets of RASAT are already met.

RASAT satellite, which is wholly designed, manufactured and tested by Turkish engineers and technicians in TUBITAK UZAY facilities, took off for Yasny Launch Base in Russian Federation on June 14th, and reached to the city of Ulyanovsk for customs procedures.



Figure 6.2 Rasat is on Its Way for Launching [77]

In the launch which is planned to take place in July 2011. The launch was performed by Dnepr launch vehicle, which was a converted SS-18 intercontinental ballistic missile, among the most reliable rockets. The launch campaign, which RASAT will participate, will be Dnepr's 17th commercial launch [77].

RASAT was developed to demonstrate satellite design, manufacturing, test and operation capabilities of TUBITAK UZAY and hence Turkey, serve as a test-bed for Turkish home-grown space hardware and software designed and developed by Turkish engineers and technicians, and to gather optical satellite images.

RASAT was operationally and structurally confirmed to be ready for launch, by TUBITAK UZAY and the launch vehicle manufacturer, in 2010 by the tests performed in launch vehicle manufacturer's facilities, in Ukraine. Thus, the basic targets of development of capabilities for designing, manufacturing and testing regarding satellite technologies and enhancing experiences and capabilities for Turkish engineers and specifically TUBITAK UZAY were already met [77].

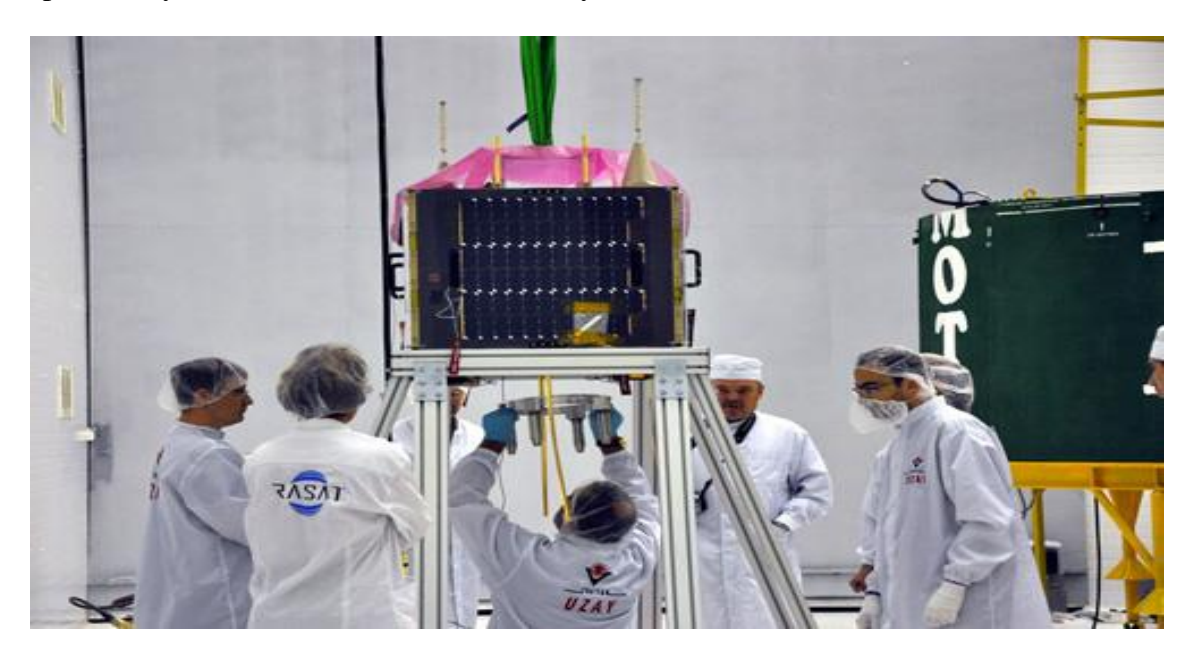


Figure 6.3 Rasat is Being Tested by TUBITAK Scientists and Engineers [77]

Injection of RASAT to the target orbit and successful trial of the space systems developed by TUBITAK UZAY, is providing not only heritage but also serve as basis for the upcoming satellite programs. Additionally, the optical images gathered by RASAT is planned to be used for city planning, forestry, agriculture, disaster management and similar purposes

6.1 Technical Properties of RASAT

Table 6.1 Technical Properties of Rasat [77]

NORAD ID	37791
Int'l Code	2011-044D
Perigee	671.8 km
Apogee	703.1 km
Inclination	98.2°
Period	98.4 minutes
Semi Major Axis	7058 km
Launch Date	August 17, 2011

RASAT, having a high-resolution optical imaging system and new modules developed by Turkish engineers, is the first Earth-observation satellite to be designed and manufactured in Turkey. Goals of RASAT project from technological standpoint are:

- 1. To develop space qualified systems using current technologies and gaining flight heritage by succeeding in operating these systems in space.
- 2. To investigate the current capabilities of Turkey for space technologies and to use as much as possible.
- 3. To increase number of qualified man power in the field of satellite technologies.

Table 6.2 Technical Properties of Rasat [77]

Weight	93 kg
Orbit	Circulat at 700 km- Low Earth Orbit (LEO) Sun-synchronous
Orientation	3 axis controlled
Period	98.8 minutes
Equator Local time	10:30
Spatial Resolution	Panchromatic: 7.5 m Multi-Band: 15 m
Estimated Lifetime	3 years
Spectral Resolution (µm)	0.42 – 0.73 (Panchromatic) 1. Bant: 0.42 – 0.55 (Blue) 2. Bant: 0.55 – 0.58 (Green) 3. Bant: 0.58 – 0.73 (Red)
Radiometric Resolution	8 bit
Temporal Resolution	4 days
Bandwidth	30 km



Figure 6.4 Turkish Remote Sensing Satellite of RASAT [77]

RASAT has various subsystems;

GEZGİN-2: A real-time on-board image processing module. It the image processing subsystem of RASAT, an earth-observing small satellite which has been developed, built and qualified by TÜBİTAK-UZAY for a LEO mission. GEZGİN-2 is responsible for real-time compression of multi-spectral images acquired by the push-broom imagers of RASAT, before being transferred to the Solid State Data Recorders on-board the satellite. By applying compression to image data prior to recording, on-board storage space and downlink communication bandwidth of RASAT is more efficiently utilized. GEZGİN-2 realizes its image processing tasks through a fully integrated application specific digital architecture, delivering a processing rate of 55Mbps and consuming 6 Watts. As all subsystems of RASAT, GEZGİN-2 has been implemented with commercial-off-the-shelf (COTS) components but qualified for its LEO mission through thermal vacuum cycling and vibrations tests compliant to ESA specifications. GEZGİN-2 has been successfully integrated on RASAT in year 2010 and is ready for launch [78].

KUZGUN [77]: Band satellite camera system for Low Earth Orbit (LEO) satellites.

• Infrared Camera with 800nm-1700nm (SWIR) spectral band (optional: visible band-panchromatic)

- 20m SWIR GSD, (optional 4m Panchromatic)
- Opto-Electronic System MTF~40%, 20 lp/mm
- Effective Focal Length: 850mm
- Controllable exposure time and readout time for different orbital altitudes
- Automatic exposure time according to the illumination level
- 128 MB local storage
- 8-bit digitization in Optic Unit
- Data Retrieval
- 25MHz LVDS

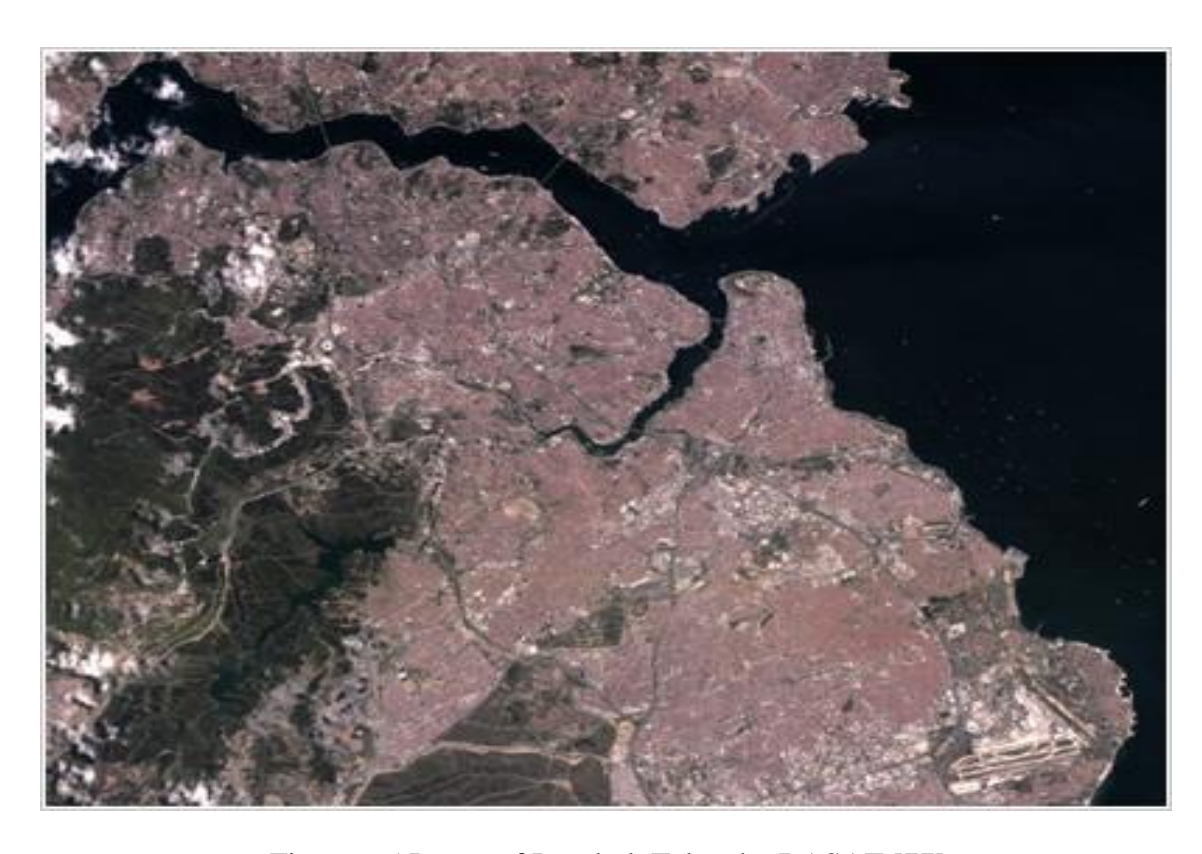


Figure 6.5 Image of Istanbul, Taken by RASAT [77]

Electric Propulsion Applications Research and Hall Thruster Development (HALE): Through the HALE project, Turkey will establish its first facility for research and development of electric thruster technologies. This project will establish the necessary knowledge base and facilities to design, manufacture, and test Hall effect thrusters [77].

T-REX Communication System: X-Band transmitter for LEO satellites. It is a The Consultative Committee for Space Data Systems (CCSDS) compatible high datarate X-Band transmitter for LEO satellites with high-efficiency solid-state power amplifier of 7W output power [77].

BILGE: On-board computer and router. Based on a new generation processor technology, BiLGE serves as a high performance and reliable flight computer and can also be employed as a data storage unit during imaging operations [77].

GILGAMESH: The first parallel processor and memory system of Turkey in the supercomputer class, designed for space missions. Being a very reliable and high-performance system, it can be used for RADAR applications such as high-resolution-optics and SAR [77].

POWER SYSTEM: Power production and distribution on satellite. The unit responsible for power production, power conditioning, and reliable power distribution within satellites under all foreseeable operational states and environments. The newly developed power system satisfies the power needs of satellites of different sizes in different orbits within the reability, functionality, flexibility, modularity needs [77].

GROUND STATION SOFTWARE: Software that enables all command control procedures of satellites, such as sending/collecting telemetry data of LEO satellites, planning missions, downloading the pictures made by the satellites, to be completed easily. The software has graphical interface mapping the satellite positions in 2D or 3D [77].

FLIGHT SOFTWARE: Communicates with ground station, receives and distributes commands and controls the satellite by determining the attitude. For a reliable operation, monitors the subsystems, collects all mission and payload data, processes and saves them. Makes decisions and executes the tasks on possible events during mission lifetime. Performs fault detection and isolation tasks reliably [77].

ANOMALIES OF RASAT

The approach for this study is splitted into 3 main parts. First one is the acquired specific environmental data set. These sets were mostly taken from NOAA, National Oceanic Atmospheric Administration. Second part is that RASAT telemetry data which was taken from TUBITAK Uzay, Turkish National Scientific Organization. This part also includes hypothetical data which were acquired with using SPENVIS, a Space Weather Model. With the help of SPE technique, the third part's purpose was to pinpoint the hidden elements of space environment behind the satellite anomalies.

Since Turkish remote sensing satellite of RASAT doesn't have a radiation sensor installed on it, trying to find the hidden agents of space weather was challenging. Most of LEO satellites are army and security based satellites, due this fact their data aren't public or outdated data are being released by the companies or governments. Multiple small databases are common yet there isn't a centralized database.

RASAT is a satellite orbiting at LEO at an altitude of 687 km. For SEUs, the solution implemented in RASAT is the following: RASAT holds three slots for each data. Each day, there is a daily check on all the slots. If one slot carries different data than the other two slots, then the one that is changed by SEU will be corrected according to the other two slots. In this case such an event is called a 'fixed' event. Rarely, all three slots are inconsistent with each other. In such a case, the error can not be corrected and will be labeled as 'severe'.

7.1 Anomalies of RASAT

LEO spacecrafts are subjected to a variety of interactions with the orbital environment and notables among these are effects related to the plasma environment. During times of geomagnetic storms in the GEO, the plasma environment has charged spacecrafts to a high level of voltages, which may result in system anomalies. However, the LEO plasma is typically of much lower energy and higher density. Although the LEO spacecrafts can not be charged to a high level voltages by plasma environment such as they are in GEO, the effects related to plasma environment are various, particular in floating potential, parasitic current loses, ion sputtering, single event upsets and others.

7.2 Incident Dates between the years of 2011-2012

Turkish Satellite RASAT's data log which holds only SEU events, has been investigated and incidents with severe severity have been counted, the days with severe severity incidents have been identified. The identified dates were the focused ones during this study. For these dates, space weather data and weekly reports were taken from NOAA. Space environment data for Low-Earth-orbit were formed with the help of SPENVIS. The literature of satellite anomalies was checked in order to see if there was any other satellites which are orbiting the Earth having anomalies and similar symptoms. Sunspots, geomagnetic storms, Kp, Ap, Dst, radio flux, solar energetic particles's flux plots were generated.

November 29th, 2011, February 4th, July 12th, December 16th, 2012 are the dates of RASAT's great anomalies for the years between 2011-2012. These particular dates have been investigated with Superposed Epoch technique which was identified briefly in chapter 5. In Figure 7.1 it is plotted as Days vs RASAT's correction counts. Green spots are the corrections against severe incidents.

Some dates have high countings of corrections which are not listed as "severe". The reason for this is that RASAT has 3 ram slots, and when one or more rams fail the other ram/rams correct the faulty readings, and that counts as one correction. When RASAT is exposed to high radiation levels, and it encounters ram failings as well, and the rams still working correct the failing ram/rams again but this time it also reports to ground based system as a SEU event.

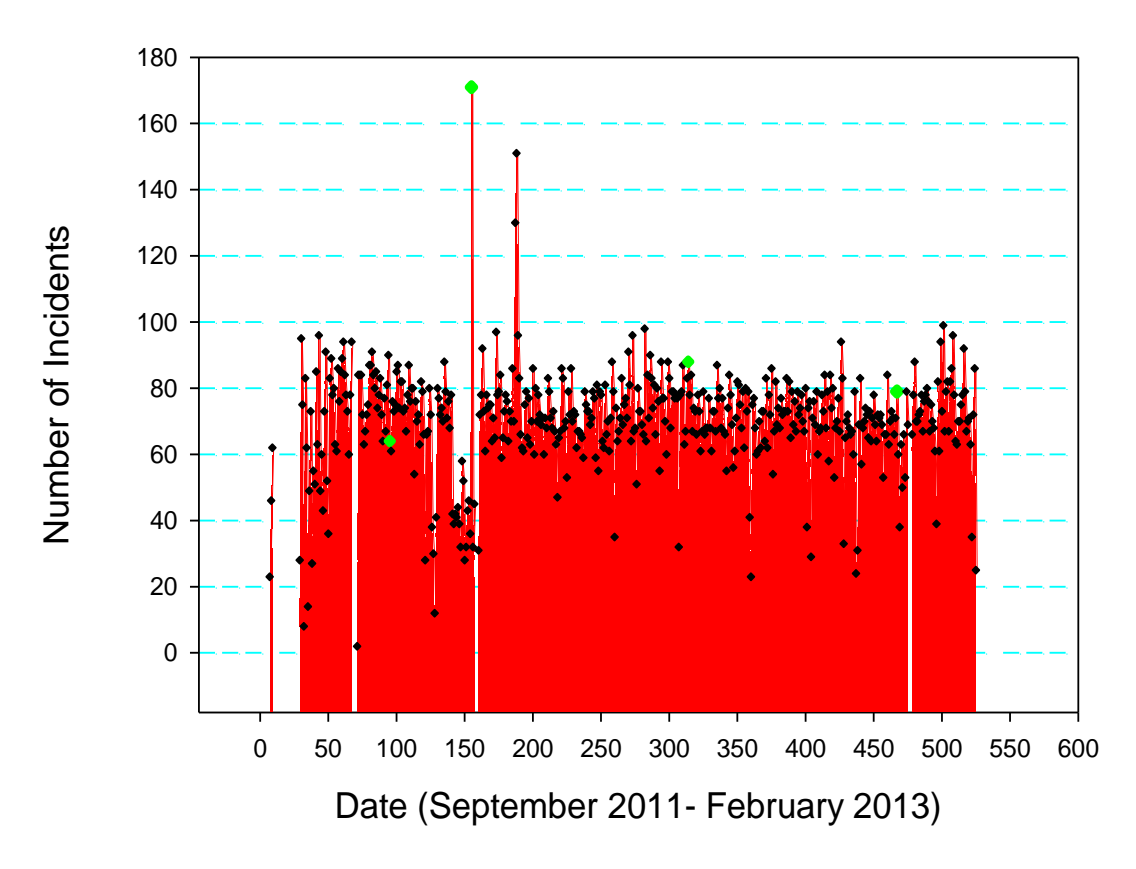


Figure 7.1 Measured SEU incidents in RASAT versus time from September 2011 to February 2013. Green data points represent the SEUs labeled as 'severe'.

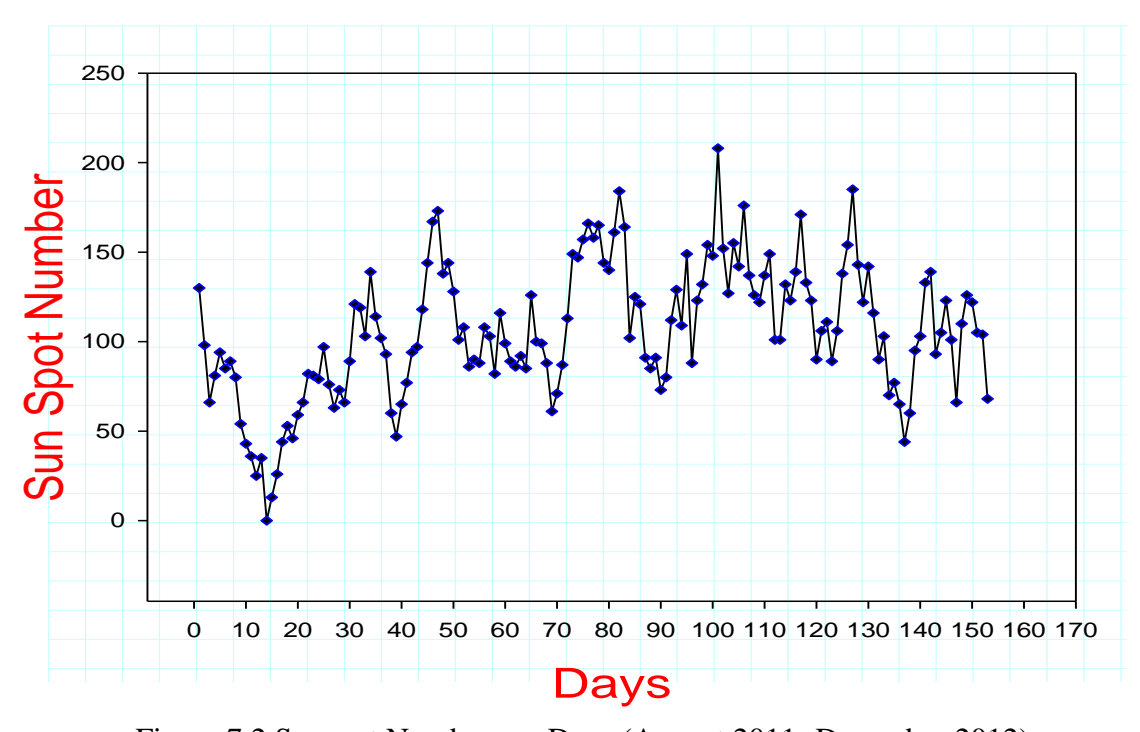


Figure 7.2 Sunspot Numbers vs Days (August 2011- December 2012)

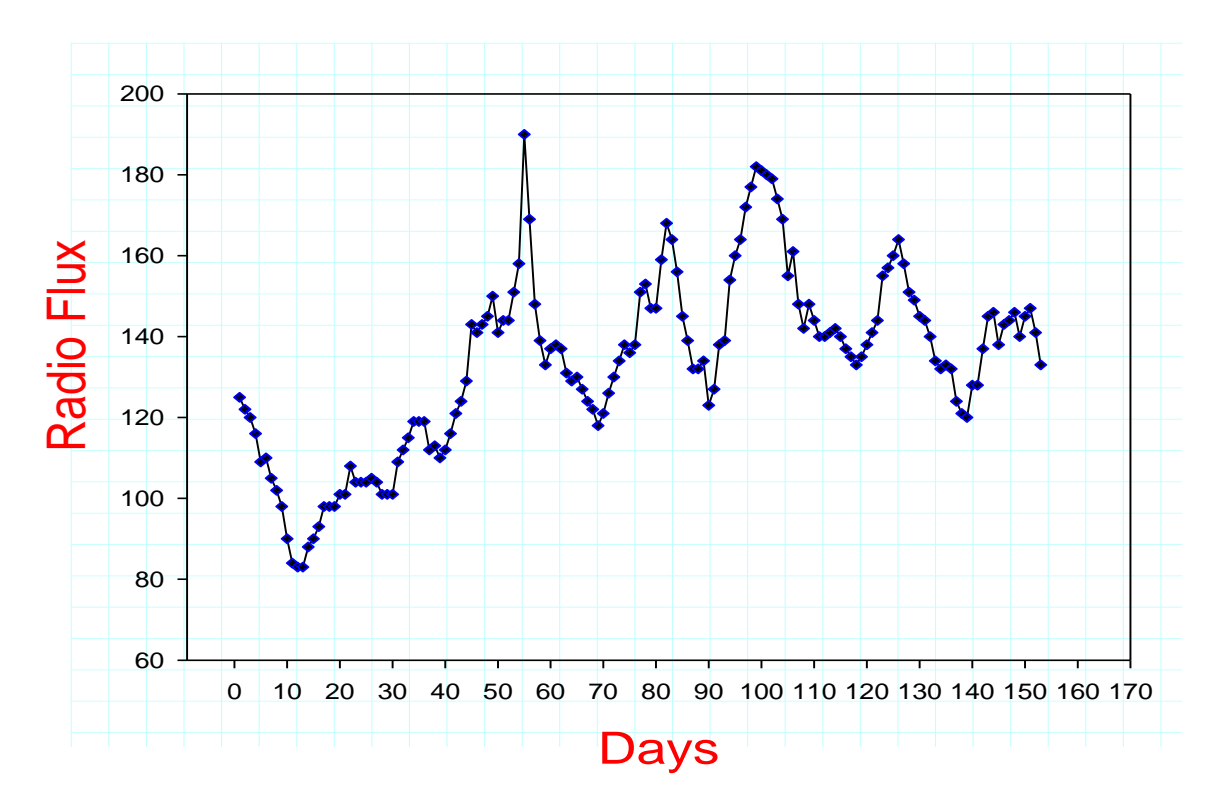


Figure 7.3 Radio Flux vs Days (August 2011- December 2012)

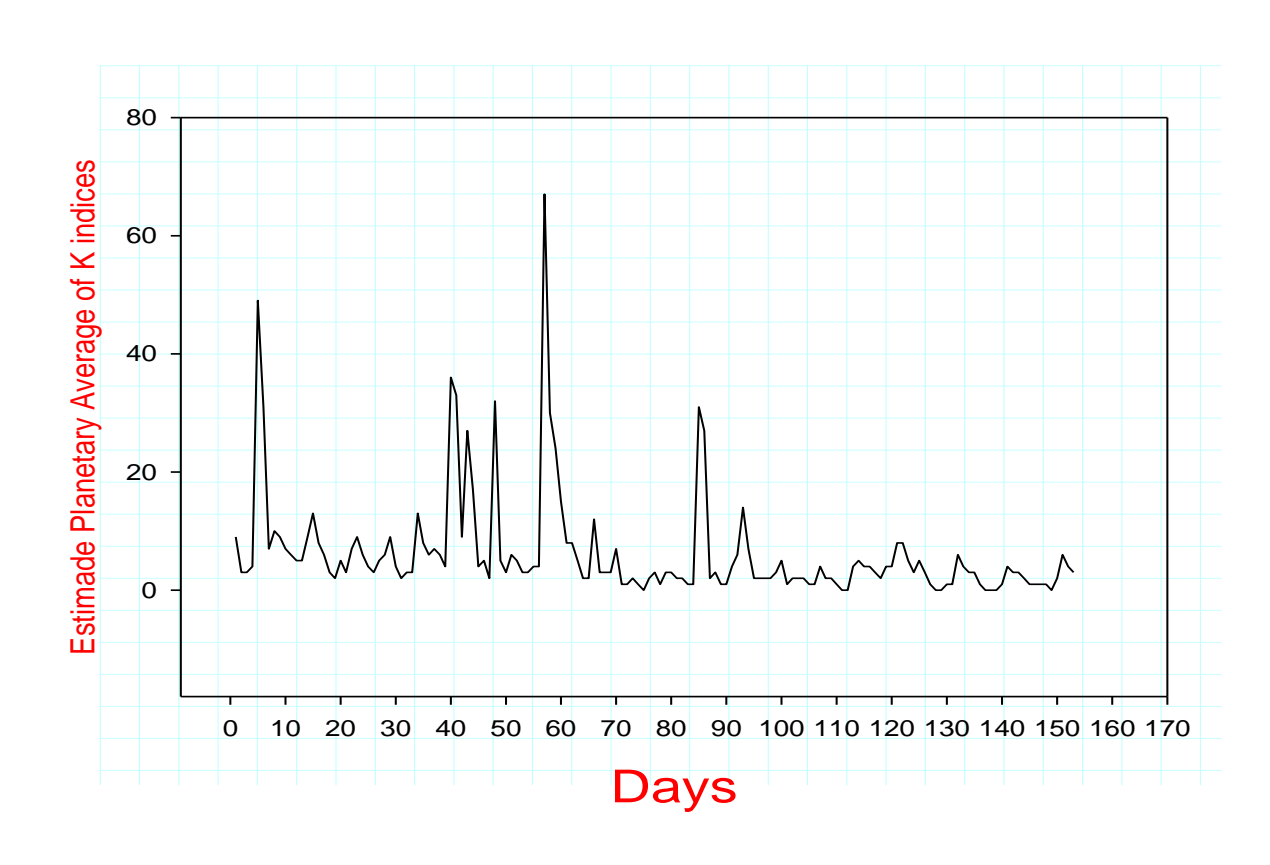


Figure 7.4 A_p Values vs Days (August 2011- December 2012)

7.2.1 September 29th, 2011 - October 8th, 2011

As one can see in Figure 7.1, Turkish remote sensing satellite of RASAT didn't send any data about the corrections it had made between the dates of September 29th,2011 and October 8th, 2011. Even though the corrections don't have be severe there had to be corrections related to RASAT's processes. In order to see what caused the problem these dataless dates were investigated.

Solar activity ranged from low to moderate levels during the period. Activity was moderate on 26 September a M4/1b event was detected at 26/0508 UTC and a M2/2b event at 26/1443 UTC. Solar activity decreased to low levels on 27 September before increasing again to moderate levels on 28 September. (Due to a M1/1n event at 28/1328 UTC with an associated Tenflare (320 sfu)). Another decrease to low levels occurred on 29 September before levels increased once again to moderate levels on 30 September through 02 October. Associated with a M1/1f event there was a Type II radio sweep with an estimated speed of 690 km/s as well as a 260 sfu Tenflare. Despite limited STEREO data, a slower CME is believed to be potentially geoeffective from this event.

A M1/1f event produced a possible earth directed CME, with an associated Type II radio sweep with an estimated speed of 850 km/s), Type IV radio sweep, and a 180 sfu Tenflare. On 02 October, M3/1n event at 02/0050 UTC that was related to an Earth directed CME visible in STEREO imagery with an estimated speed of 532 km/s. Final a M1/Sf event at 02/1723 UTC. A greater than 10 MeV proton event at geosynchronous orbit began at 23/2255 UTC in response to an X1 flare on 22 September, reached a maximum of 35 pfu at 26/1155 UTC, and ended at 27/0430 UTC. Fluxes returned to background levels for the remainder of the period.

The greater than 2 MeV electron flux at geosynchronous orbit was at normal to moderate levels from 26 to 29 September. Fluxes increased to high levels on 30 September, returned to normal to moderate levels on 01 October, and back to high levels on 02 October. Geomagnetic activity ranged from quiet to severe storm levels during the period. Increased activity on 26 - 28 September was due to effects of an expected CME from 24 September. Increased activity early on 29 September was due to nighttime sub-storms. Increased activity on 01 - 02 October was due to a solar sector boundary crossing (SSBC) prior to the onset of high speed stream (HSS) effects from a favorably positioned coronal hole. Solar activity is expected to be at low to moderate

levels during 05 - 15 October with a slight chance for M-class flare activity on 07 October, and disturbances had ended on 08 October. The greater than 2 MeV electron flux at geosynchronous orbit reached high levels during 03 - 05 October. Normal to moderate levels were observed during 06 - 09 October.

Geomagnetic field activity was at quiet to unsettled levels during 03 - 04 October. Activity increased to quiet to minor storm levels on 05 October following a geomagnetic sudden impulse at 05/0742 UTC (19 nT, Boulder USGS magnetometer), with major storm levels observed at high latitudes, due to multiple CME passages at Earth. Activity decreased to quiet to unsettled levels during 06 - 08 October. An increase to quiet to active levels occurred on 09 October associated with a solar sector boundary change.

Table 7.1 Radio Flux, Sunspot Numbers, Sunspot Area [58]

	Radio Flux	Sunspot	Sunspot Area
Date	10.7 cm	Numbers	(10 ⁻⁶ hemi.)
27 September	139	82	1110
28 September	133	116	1240
29 September	137	99	920
30 September	138	89	970
1 October	137	86	950
2 October	131	92	760
3 October	129	85	785
4 October	130	126	1015
5 October	127	100	850
6 October	124	99	880
7 October	122	88	790
8 October	118	61	450

Table 7.2 Proton Flux Values, Taken from NOAA [58]

	Proton Flux	Proton Flux	Proton Flux
Date	(protons/cm ² day sr)	(protons/cm ² day sr)	(protons/cm ² day sr)
Range	>1 MeV	>10 MeV	>100 MeV
27 September	2.9e+07	5.9e+05	2.4e+03
28 September	1.0e+07	2.3e+05	2.7e+03
29 September	5.7e+06	9.4e+04	2.9e+03
30 September	2.1e+06	2.7e+04	2.9e+03
1 October	7.5e+05	1.6e+04	3.1e+03
2 October	5.7e+05	1.3e+04	2.9e+03
3 October	4.5e+05	1.3e+04	3.2e+03
4 October	4.9e+05	1.5e+04	3.4e+03
5 October	1.6e+06	1.6e+04	2.7e+03
6 October	1.2e+06	1.4e+04	2.8e+03
7 October	4.9e+05	1.3e+04	3.1e+03
8 October	1.6e+06	1.3e+04	3.2e+03

Table 7.3 Proton, Peak 5-minute-averaged fluxes Values at Spacecraft, Generated by SPENVIS

	Proton Flux	Proton Flux	Proton Flux
Date	(protons/cm ² day sr)	(protons/cm ² day sr)	(protons/cm ² day sr)
Range	>1 MeV	>10 MeV	>100 MeV
27 September	2.732e+04	1.127e+03	2.712e+01
28 September	2.725e+04	1.124e+03	2.705e+01
29 September	2.732e+04	1.127e+03	2.712e+01
30 September	2.739e+04	1.130e+03	2.719e+01
1 October	2.742e+01	1.131e+01	2.722e+01
2 October	2.735e+04	1.128e+03	2.715e+01
3 October	2.742e+04	1.131e+03	2.722e+01
4 October	2.742e+04	1.131e+03	2.722e+01
5 October	2.756e+04	1.137e+03	2.735e+01
6 October	2.749e+04	1.134e+03	2.729e+01
7 October	2.776e+04	1.145e+03	2.756e+01
8 October	1.148e+03	1.148e+03	2.762e+01

Table 7.4 Electron Flux Values [58]

(electrons/cn	
(electrons/cm ² day sr)	
>0.6 MeV >2M	eV >4 MeV
2.1e+07	
1.8e+07	
3.8e+07	
7.5e+07	
2.2e+07	
4.7e+07	
9.8e+07	
1.3e+08	
4.0e+07	
1.1e+07	
4.0e+06	
7.0e+06	
	2.1e+0 1.8e+0 3.8e+0 7.5e+0 2.2e+0 4.7e+0 4.0e+0 1.1e+0 4.0e+0

Table 7.5 Electron Flux Values at Spacecraft, Generated by SPENVIS

	Electron Flux		
Date	(electrons/cm ² day sr)		
Range	>0.6 MeV >2MeV >4 MeV		
27 September	2.2728e+09		
28 September	1.8088e+11		
29 September	4.0354e+10		
30 September	5.9583e+10		
1 October	2.2452e+10		
2 October	4.0172e+10		
3 October	4.0158e+10		
4 October	1.0489e+08		
5 October	1.0473e+08		
6 October	1.0484e+08		
7 October	1.3589e+03		
8 October	4.0114e+10		

7.2.2 November 29th, 2011

RASAT made 64 corrections with severe severity on November 29th, 2011. During the whole week solar activity was low. On average, seven small and magnetically simple spotted regions were present at any given time during this period. Five C-class flares and 4 optical flares were detected. It appeared on the disk on 29 November as a small Hsx-alpha group and ended the period as the largest and most magnetically complex (beta-gamma) group on the disk. Despite its size and complexity, Region 1363 did not produce the largest x-ray flare of the week.

At least one CME was observed each day in coronagraph imagery, mostly attributed to filament eruptions. None of the CMEs had any significant geoeffective component. The greater than 10 MeV protons at 10 pfu exceeded threshold during the period. The event reached a maximum flux of 80 pfu. This event was associated with a filament eruption observed early on 26 November. The greater than 2 MeV electron flux at geosynchronous orbit was at normal levels, which means electron flux wasn't an issue at LEO.

The geomagnetic field on 27 November was at quiet to unsettled levels, with isolated high latitude active periods. Most of 28 November was quiet. A 45 nT Sudden Impulse at the Boulder magnetometer signaled the arrival of a CME from 26 November. Unsettled to minor storm periods followed at all latitudes. Quiet to unsettled levels, with isolated high latitude active periods, returned by midday on 29 November and lasted until early on 03 December. Radio flux and A_p values were not high enough to form a radio blackout nor a strong geomagnetic storm.

A partial solar eclipsed occured on November 25th, 2011. Geographic reagons for this eclipse were South Africa, Antarctica and Tasmania. This may had created substorms in magnetosphere of the Earth, and Kp values were around 4-5.

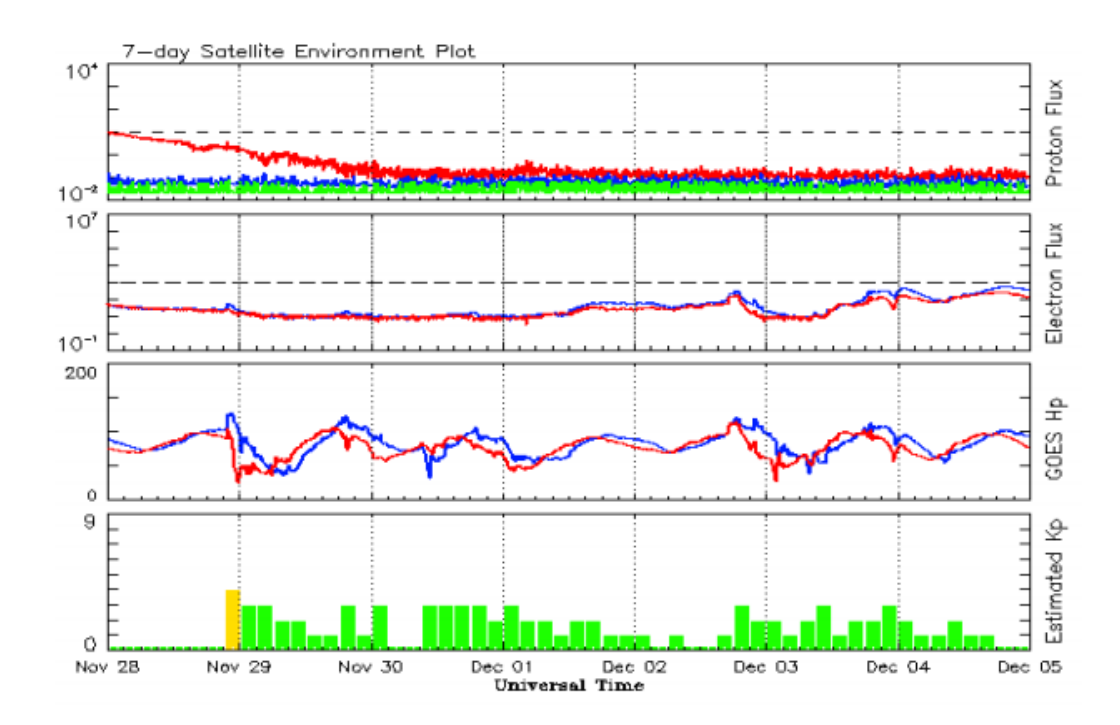


Figure 7.5 Geosynchronius satellite environment plot, proton flux, electron flux (The electron flux plot contains the five-minute averaged integral electron flux (electrons/cm -sec -sr) with energies greater than 2 MeV by the SWPC Primary GOES satellite.), GOES Hp(The GOES Hp plot contains the 1-minute averaged parallel component of the magnetic field in nanoTeslas (nT), as measured at GOES-13 and GOES 15), Estimated Kp, starting from November 28, ending on December 05 [58].

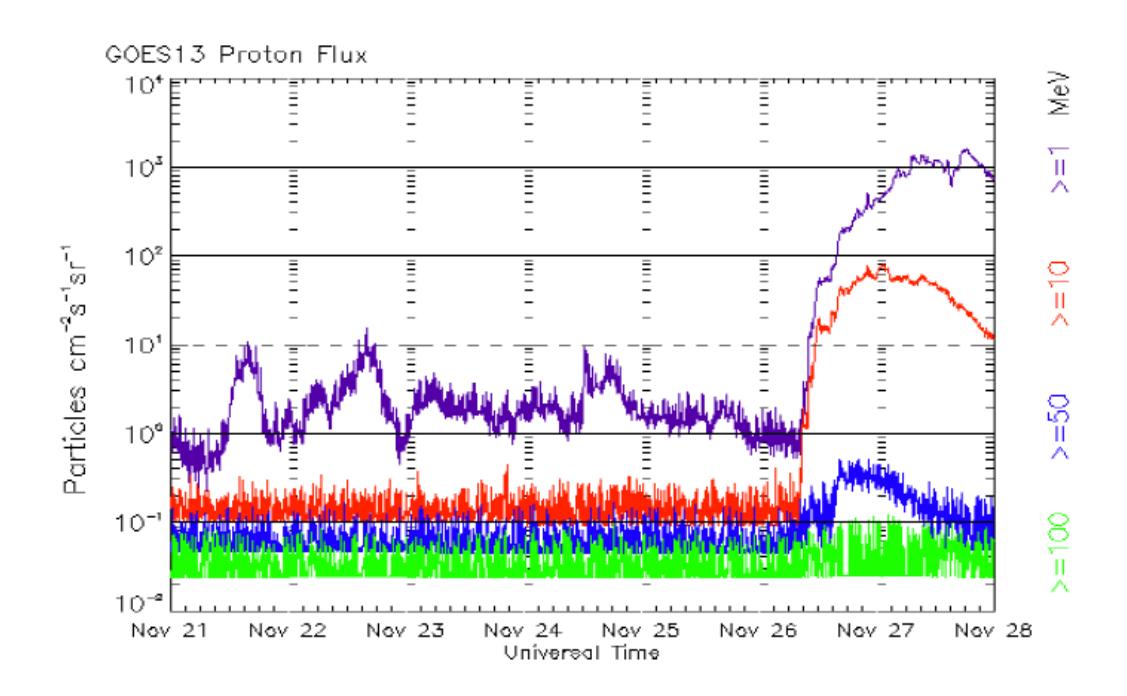


Figure 7.6 Goes 13 Proton flux, The proton plot contains the five-minute averaged intergral flux units primary SWPC GOES Proton satellite for each of the energy thresholds: >1, >10, >30, and >100 MeV. The P10 event threshold is 10 pfu at greater than 10 MeV.

Table 7.6 Radio Flux, Sunspot Numbers, Sunspot Area [58]

	Radio Flux	Sunspot	Sunspot Area
Date	10.7 cm	Numbers	(10 ⁻⁶ hemi.)
28 November	138	90	350
29 November	141	106	510
30 November	144	111	620

Table 7.7 Proton Flux Values [58]

	Proton Flux	Proton Flux	Proton Flux
Date	(protons/cm ² daysr)	(protons/cm ² daysr)	(protons/cm ² daysr)
Range	>1 MeV	>10 MeV	>100 MeV
28 November	2.4e+07	4.3e+05	2.9e+03
29 November	1.1e+07	6.4e+04	2.7e+03
30 November	1.8e+06	1.6e+04	2.9e+03

Table 7.8 Proton, Peak 5-minute-averaged fluxes Values at Spacecraft, Generated by SPENVIS

Date	Proton Flux (protons/cm ² daysr)	Proton Flux (protons/cm ² daysr)	Proton Flux (protons/cm ² daysr)
Range	>1 MeV	>10 MeV	>100 MeV
28 November	2.742e+04	1.131e+03	2.722e+01
29 November	2.735e+04	1.128e+03	2.715e+01
30 November	2.756e+04	1.137e+03	2.735e+01

Table 7.9 Electron Flux Values [58]

Date	Electron Flux (electrons/cm² day sr)	
Range	>0.6 MeV >2MeV >4 MeV	
28 November	2.8e+06	
29 November	1.0e+06	
30 November	8.5e+05	

Table 7.10 Electron Flux Values at Spacecraft, Generated by SPENVIS

	Electron Flux	
Date	(electrons/cm ² day sr)	
Range	>0.6 MeV >2MeV >4 MeV	
28 November	2.2798e+09	
29 November	1.0603e+08	
30 November	8.7542e+10	

7.2.3 February 4th, 2012

RASAT made 171 corrections with severe severity. Solar activity ranged from very low to low levels throughout the period with two C-class flares observed. A C1 event was detected on 30 January, and a second C1 flare was produced on 01 February. Low level B-class activity dominated the remainder of the period.

The greater than 10 MeV proton event reached a maximum of 796 pfu, and dropped below the 10 pfu threshold afterwards. The greater than 2 MeV electron flux at geosynchronous orbit reached high levels on 30 January. Predominantly background levels prevailed with moderate levels observed from 03 - 04 February. This may effected LEO satellites too.

The geomagnetic field was at predominantly quiet to unsettled levels during the past week. The geomagnetic field was quiet, until the arrival of a glancing blow from the asymmetric halo CME that occurred in association with the X1/1f flare on 27 January. The transient passage was observed by the ACE spacecraft with a solar wind speed increase from around 320 km/s to near 430 km/s. A weak sudden impulse measuring 8 nT was observed by the Boulder magnetometer. The field increased to unsettled levels following the shock but returned to quiet levels. Quiet conditions prevailed on 31 January. On 01 February, a coronal hole high speed stream became geoeffective with unsettled to minor storm levels observed at high latitudes and predominantly quiet levels observed at mid latitudes from 01 February through the end of the summary period on 05 February.

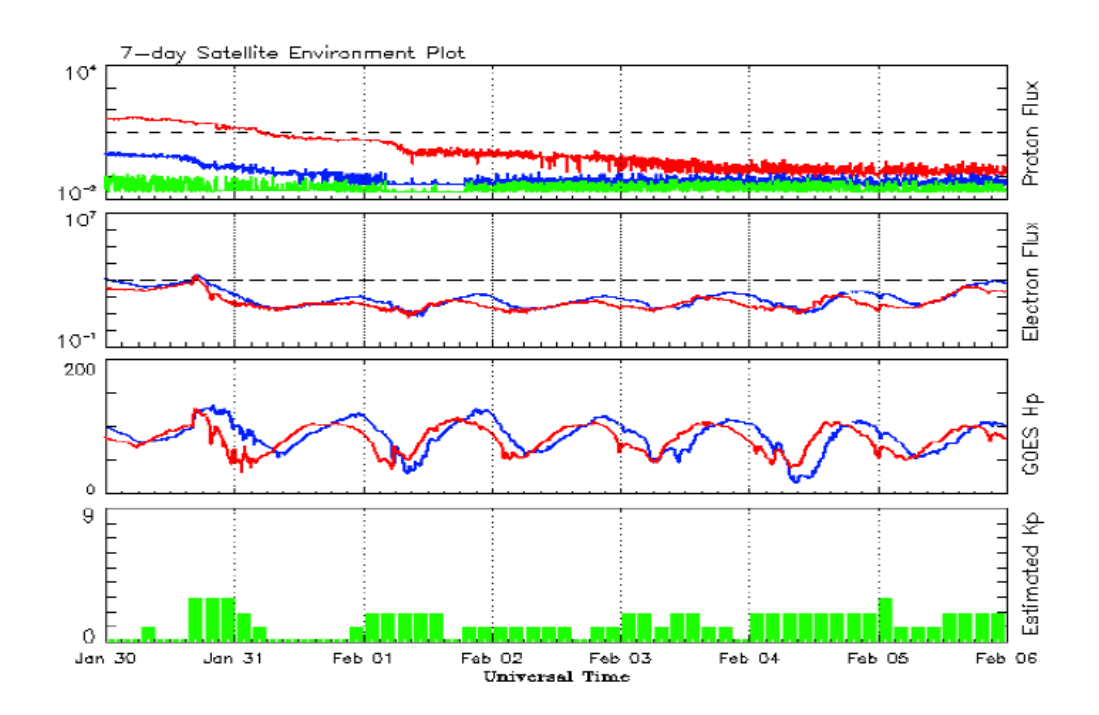


Figure 7.7 Geosynchronius satellite environment plot, proton flux, electron flux (The electron flux plot contains the five-minute averaged integral electron flux (electrons/cm -sec -sr) with energies greater than 2 MeV by the SWPC Primary GOES satellite.), GOES Hp(The GOES Hp plot contains the 1-minute averaged parallel component of the magnetic field in nanoTeslas (nT), as measured at GOES-13 and GOES 15), Estimated Kp, starting from November 28, ending on December 05 [58]

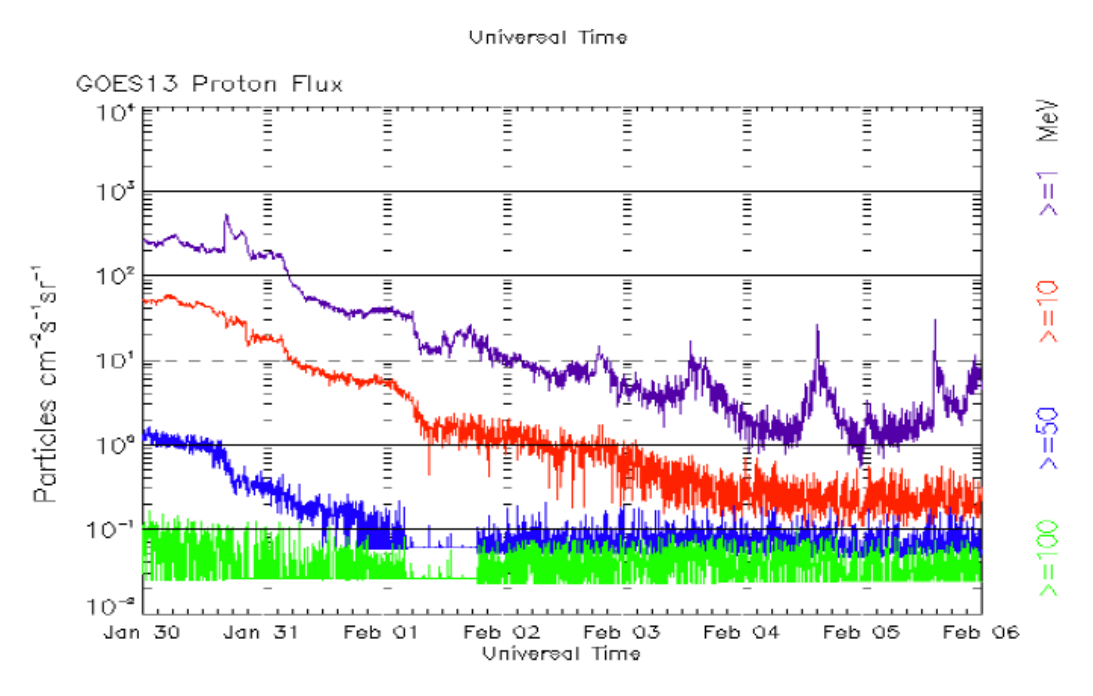


Figure 7.8 Proton Flux [58]

Table 7.11 Radio Flux, Sunspot Numbers, Sunspot Area [58]

	Radio Flux	Sunspot	Sunspot Area
Date	10.7 cm	Numbers	(10 ⁻⁶ hemi.)
3 February	11	39	280
4 February	107	43	270
5 February	103	107	170

Table 7.12 Proton Flux Values [58]

	Proton Flux	Proton Flux	Proton Flux
Date	(protons/cm ² daysr)	(protons/cm ² daysr)	(protons/cm ² daysr)
Range	>1 MeV	>10 MeV	>100 MeV
3 February	4.1e+05	3.7e+04	3.8e+03
4 February	2.4e+05	2.2e+04	3.6e+03
5 February	2.6e+05	2.0e+04	3.2e+03

Table 7.13 Proton, Peak 5-minute-averaged fluxes Values at Spacecraft, Generated by SPENVIS

Date	Proton Flux (protons/cm ² daysr)	Proton Flux (protons/cm ² daysr)	Proton Flux (protons/cm ² daysr)
Range	>1 MeV	>10 MeV	>100 MeV
3 February	2.820e+04	1.163e+03	2.799e+01
4 February	2.806e+04	1.158e+03	2.786e+01
5 February	2.786e+04	1.149e+03	2.766e+01

Table 7.14 Electron Flux Values [58]

Date	Electron Flux (electrons/cm² day sr)		
Range	>0.6 MeV >2MeV >4 MeV		
3 February	4.8e+06		
4 February	4.5e+06		
5 February	1.5e+07		

Table 7.15 Electron Flux Values at Spacecraft, Generated by SPENVIS

	Electron Flux	
Date	(electrons/cm ² day sr)	
Range	>0.6 MeV >2MeV >4 MeV	
3 February	2.0824e+09	
4 February	3.5156e+07	
5 February	3.5708e+09	

7.2.4 July 12th, 2012

RASAT made 88 corrections with severe severity. Solar activity ranged from low to high levels due to activity from a complex of closely spaced regions in the southern hemisphere. These spotted groups were made up of Regions 1519 (S15, L=107, class/area Hsx/120 on 05 July), 1520 (S16, L=86, class/area Fkc/1460 on 12 July), and 1521 (S21, L=96, class/area Eki/300 on 12 July). Region 1520 grew into a large Fkc spot group with a Beta-Gamma-Delta magnetic configuration with over 1300 millionths in area by 09 July and continued to remain large and magnetically complex as it rotated across the visible disk. Region 1520 produced M1 flares at 09/2307 UTC and 10/0514 UTC, an M2/1f flare at 10/0627 UTC, and a long duration X1/2b flare at 12/1649 UTC. Associated with the X1/2b flare were Type II (1268 km/s) and Type IV radio emissions along with an 800 sfu Tenflare and a geoeffective CME with an estimated plane-of-sky speed of 1453 km/s. Region 1521 produced an M1/1f flare at 14/0458 UTC. Region 1521 continued to grow through the period into an Eki spot group with 300 millionths of area and a Beta-gamma magnetic classification. A greater than 10 MeV proton event

at geosynchronous orbit began at 09/0130 UTC, reached a maximum of 19 pfu at 09/0430 UTC and ended at 09/1445 UTC. This event was likely associated with the 08 July M6/1n flare at 08/1632 UTC from Region 1515 (S18, L=206, class/area Fhc/900 on 06 July). A second greater than 10 MeV proton event began at 12/1835 UTC, reached a maximum of 96 pfu at 12/2225 UTC, and ended at 15/0200 UTC. This event was associated with the X1/2b flare at 12/1649 UTC from Region 1520. The greater than 2 MeV electron flux at geosynchronous orbit was at moderate levels on 09 and 15 July, but reached high levels 10 through 14 July.

Geomagnetic field activity was at unsettled to minor storm levels, on 09 July, with high latitude major storm intervals due to residual CME effects likely associated with the 04 July M1 event. July 10 began with an isolated period of active levels and decreased to quiet to unsettled levels for the remainder of the day. On 11 and 12 July, activity was mostly quiet to unsettled with an isolated active period with high latitude intervals of minor to major storm levels. Quiet conditions were observed from 13 July till late on 14 July when a CME associated with the 12 July X1/2b flare arrived. At 14/1728 UTC, a shock was observed at the ACE spacecraft followed by a sudden impulse (27 nT) at the Boulder magnetometer at 14/1811 UTC. Solar wind speed at the ACE spacecraft increased from approximately 350 km/s to 630 km/s while the Bz component of the interplanetary magnetic field (IMF) went south to around -12 nT. At around 15/0600 UTC, solar wind speed was around 600 km/s while the IMF Bz went south around -16 nT and stayed steadily southward through the end of the period. The geomagnetic field responded with active to major storm levels while minor to severe storm conditions were observed at high latitudes through the end of the summary period.

On 12 July, at 1653 UTC Sun's AR1520 sunspot produced X1.4 class solar flare and a few c classes. A coronal mass ejection with a 1480km/s solar wind steam speed directly towards Earth had been observed. Related to this CME there had been a particle elevation at SOHO, STEREO B and other GOES satellites. The energetic proton flux of greater than 10 MeV exceeded the radiation storm threshold value 10 pfu due to the X class solar flare. In the following days due to the CME arrival there were reports about more satellite malfunctions. During this period the satellite Calipso commanded to SAFE mode due to the energetic particle elevation. It had lost 28 days of scientific data. GOES-13 suffered filter wheel anomalies.

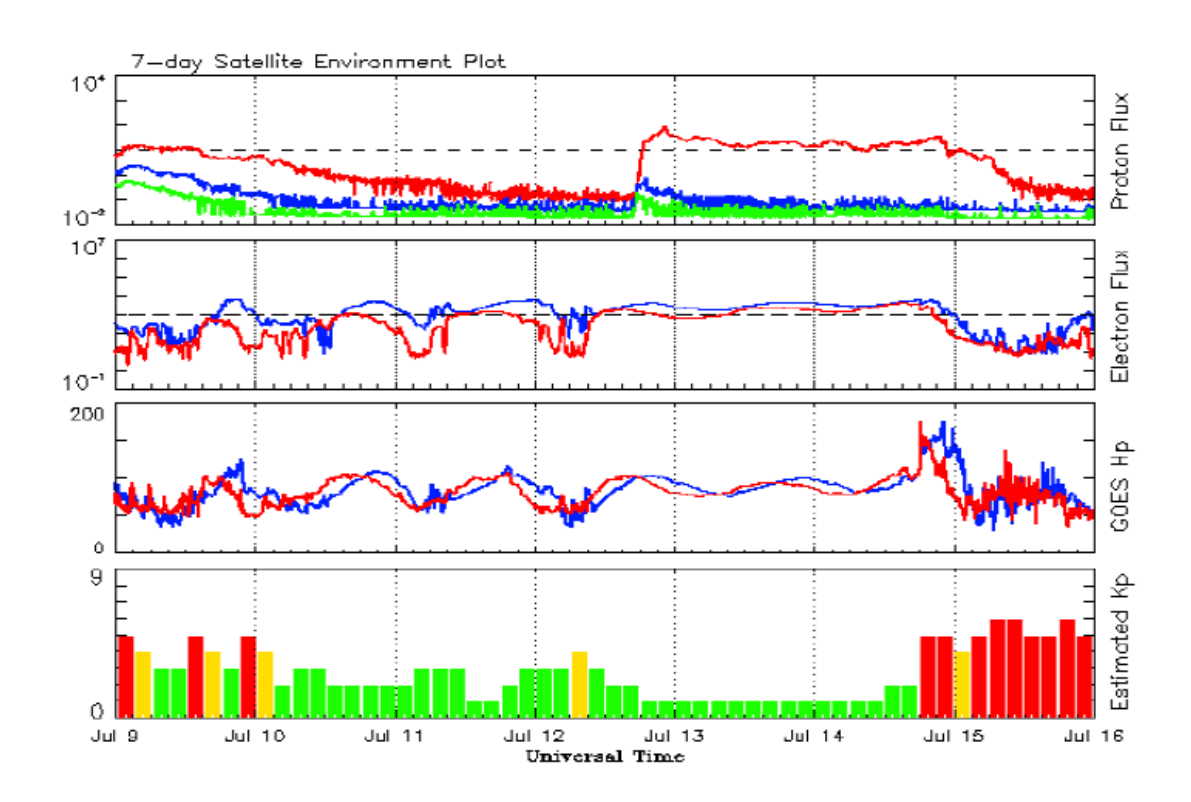


Figure 7.9 7-day Satellite data including proton flux, electron flux, Goes Hp, Estimated Kp [58]

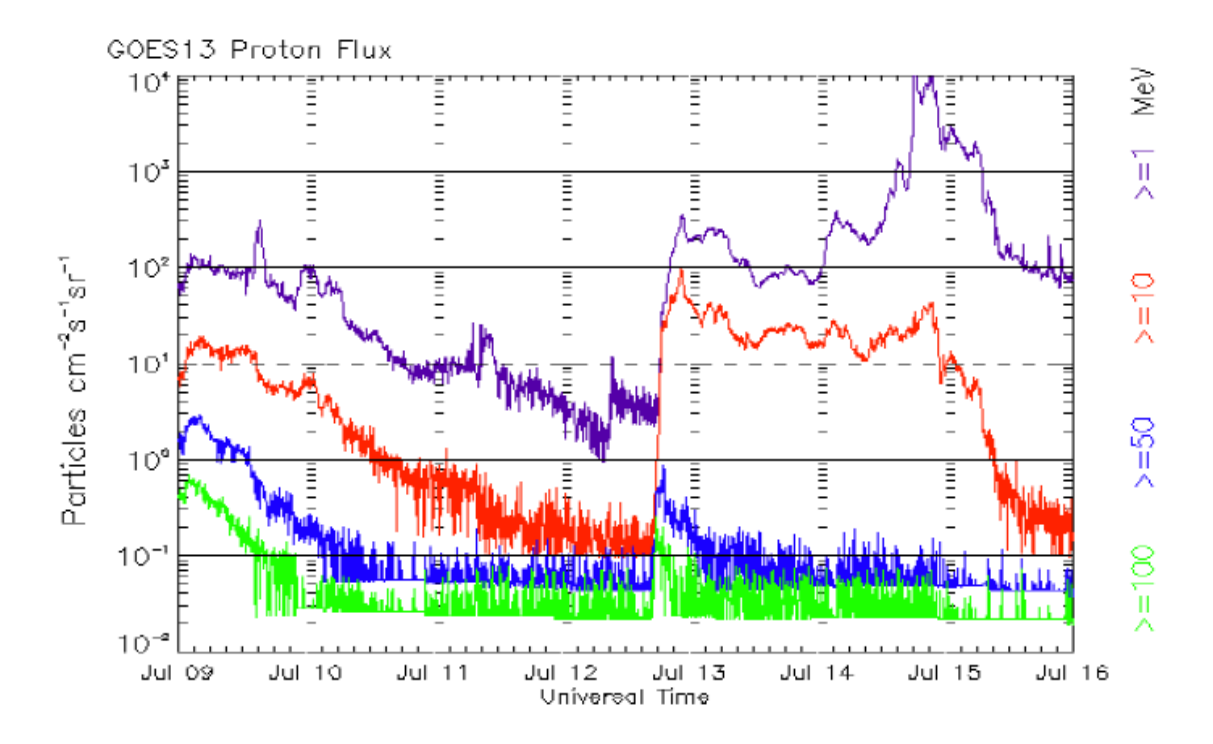


Figure 7.10 Proton Flux [58]

Table 7.16 Radio Flux, Sunspot Numbers, Sunspot Area [58]

	Radio Flux	Sunspot	Sunspot Area
Date	10.7 cm	Numbers	(10 ⁻⁶ hemi.)
11 July	162	94	1510
12 July	165	132	1750
13 July	147	112	1270

Table 7.17 Proton Flux Values [58]

Data	Proton Flux	Proton Flux	Proton Flux
Date	(protons/cm ² daysr)	(protons/cm ² daysr)	(protons/cm ² daysr)
Range	>1 MeV	>10 MeV	>100 MeV
11 July	7.3e+05	3.1e+04	2.7e+03
12 July	3.5e+06	9.5e+05	3.7e+03
13 July	1.1e+07	2.1e+06	3.3e+03

Table 7.18 Proton, Peak 5-minute-averaged fluxes Values at Spacecraft, Generated by SPENVIS

Date	Proton Flux (protons/cm ² daysr)	Proton Flux (protons/cm ² daysr)	Proton Flux (protons/cm ² daysr)
Range	>1 MeV	>10 MeV	>100 MeV
11 July	2.739e+04	1.130e+03	2.719e+01
12 July	2.766e+04	1.141e+03	2.746e+01
13 July	2.759e+04	1.138e+03	2.739e+01

Table 7.19 Electron Flux Values [58]

	Electron Flux	
Date	(electrons/cm ² day sr)	
Range	>0.6 MeV >2MeV >4 MeV	
11 July	6.8e+07	
12 July	8.3e+07	
13 July	1.6e+08	

Table 7.20 Electron Flux Values at Spacecraft, Generated by SPENVIS

Date	Electron Flux (electrons/cm² day sr)	
Range	>0.6 MeV >2MeV >4 MeV	
11 July	5.5790e+09	
12 July	9.0686e+10	
13 July	1.3114e+10	

7.2.5 December 16th 2012

RASAT made 79 corrections with severe severity. Solar activity was low. The largest flare of the period came from Region 1629 (N11, L=240, class/area=Dai/170 on 14 December), a C5/Sf 12/0727Z. Region 1630 (N19, L=253, class/area=Cai/90 on 11 December), also produced a C5 flare on 10/0558Z. The remainder of the period was dominated by infrequent, low-level C-class activity. No earth-directed coronal mass ejections were observed during the week. A 10 MeV proton enhancement at geosynchronous orbit was observed on 14-15 December.

10 MeV particle flux was slightly elevated beginning around 14/0900Z. An eruption from the beyond the west limb, in the southern hemisphere, was visible in STEREO-A EUVI imagery beginning around 14/1200Z. 10 MeV flux began climbing more steeply around 14/2245Z, reaching a peak of 9.36 pfu at 15/0155Z, just below the S1 threshold of 10 pfu. Flux returned to normal levels over the course of the next two days. The greater than 2 MeV electron flux at geosynchronous orbit was at normal levels throughout the week.

Geomagnetic field activity quiet all week. Solar wind speed at the ACE spacecraft ranged from around 270 km/s to the near 470 km/s while Bz was never less than -8 nT. A very weak shock was observed at the ACE spacecraft at 14/1852Z, and at GOES by

14/1946Z. Isolated unsettled to minor storm levels were subsequently observed at high latitudes mid-day on 15 and 16 December.

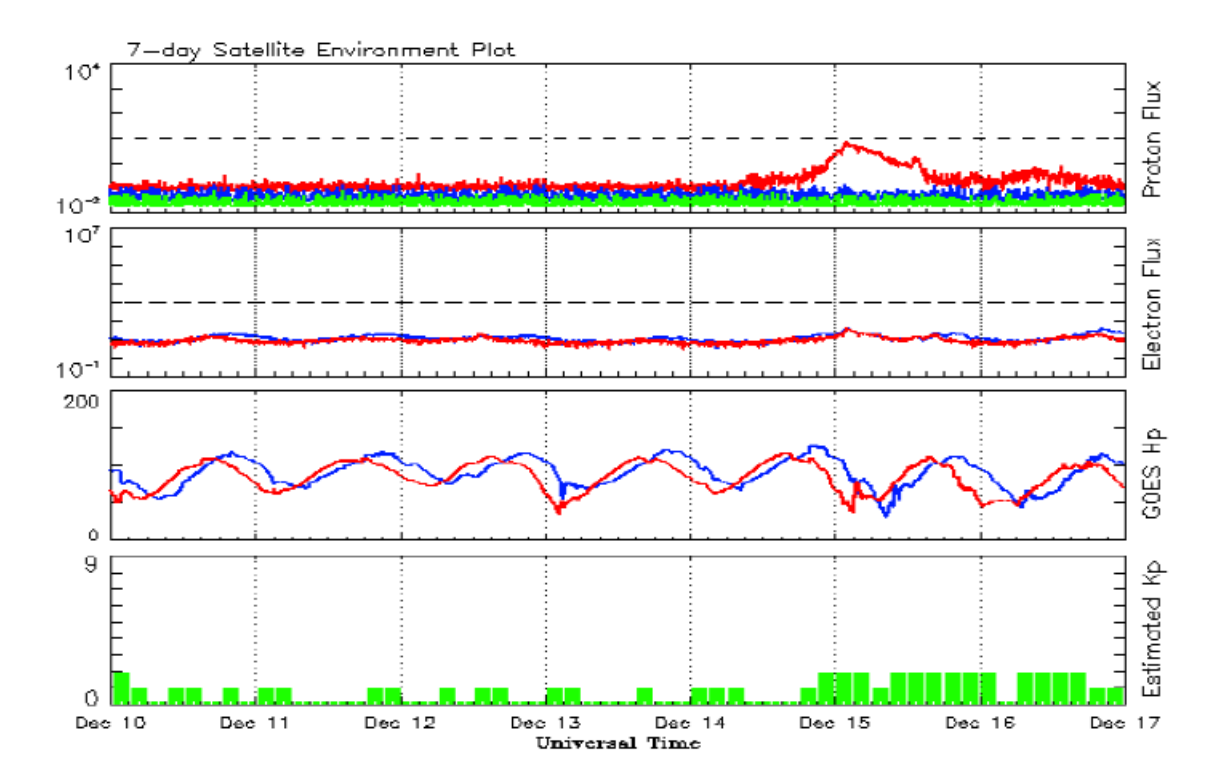


Figure 7.11 7-day Satellite data including proton flux, electron flux, Goes Hp, Estimated Kp [58]

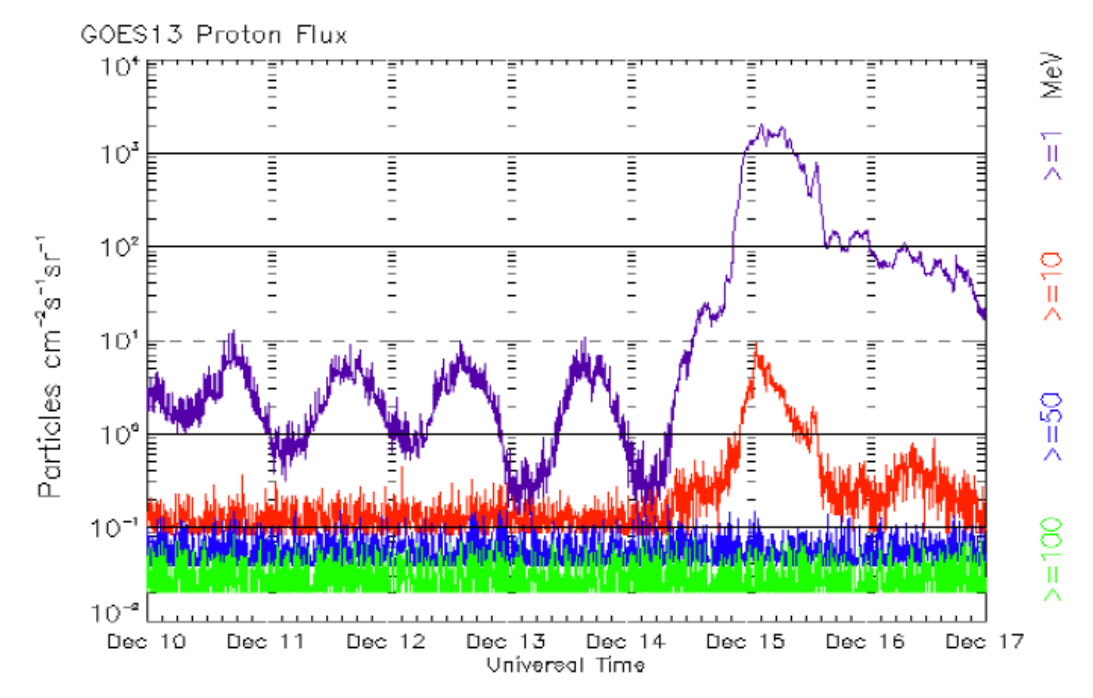


Figure 7.12 Proton Flux [58]

Table 7.21 Radio Flux, Sunspot Numbers, Sunspot Area [58]

	Radio Flux	Sunspot	Sunspot Area
Date	10.7 cm	Numbers	(10 ⁻⁶ hemi.)
15 December	122	88	650
16 December	150	74	570
17 December	115	83	680

Table 7.22 Proton Flux Values [58]

	Proton Flux	Proton Flux	Proton Flux
Date	(protons/cm ² daysr)	(protons/cm ² daysr)	(protons/cm ² daysr)
Range	>1 MeV	>10 MeV	>100 MeV
15 December	6.7e+07	1.6e+05	2.6e+03
16 December	5.4e+06	2.4e+04	2.7e+03
17 December	1.7e+06	1.3e+04	2.8e+03

Table 7.23 Proton, Peak 5-minute-averaged fluxes Values at Spacecraft, Generated by SPENVIS

Date	Proton Flux (protons/cm ² daysr)	Proton Flux (protons/cm ² daysr)	Proton Flux (protons/cm ² daysr)
Date	(protons/em daysr)	(protons/cm daysr)	(protons/em daysr)
Range	>1 MeV	>10 MeV	>100 MeV
15 December	2.715e+04	1.120e+03	2.695e+01
16 December	2.715e+04	1.120e+03	2.695e+01
17 December	2.729e+04	1.126e+03	2.709e+01

Table 7.24 Electron Flux Values [58]

Date	Electron Flux (electrons/cm² day sr)	
Range	>0.6 MeV >2MeV >4 MeV	
15 December	1.4e+06	
16 December	1.0e+06	
17 December	4.1e+06	

Table 7.25 Electron Flux Values at Spacecraft, Generated by SPENVIS

	Electron Flux	
Date	(electrons/cm ² day sr)	
Range	>0.6 MeV >2MeV >4 MeV	
15 December	1.0765e+08	
16 December	1.0748e+08	
17 December	4.0990e+10	

7.3 Incident Dates between the years of 2013-2014

June 3rd, 2013, July 9th, July 10th and July 25th, 2013, August 8th, 2013, October 11th, 2013, and Janury 8th, 2014 are the dates of RASAT's great anomalies for the years between 2011-2014. These particular dates have been investigated with Superposed Epoch technique which was identified briefly in chapter 5. In Figure 7.13 and in Figure 7.14, it is plotted as Days vs RASAT's correction counts. Green spots are the corrections against severe incidents.

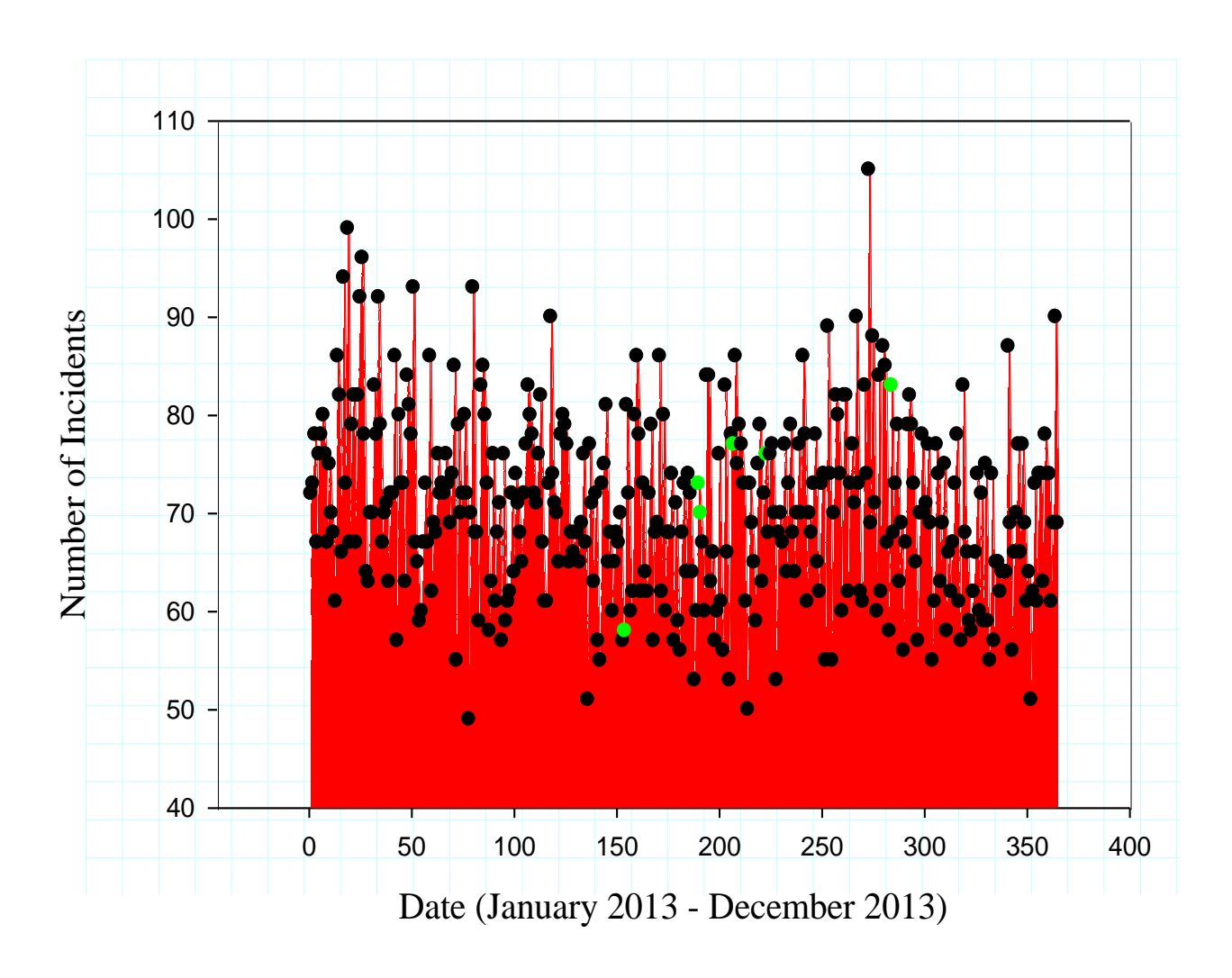


Figure 7.13 Measured SEU incidents in RASAT versus time from January 2013 to December 2013. Green data point represent the SEUs labeled as 'severe'.

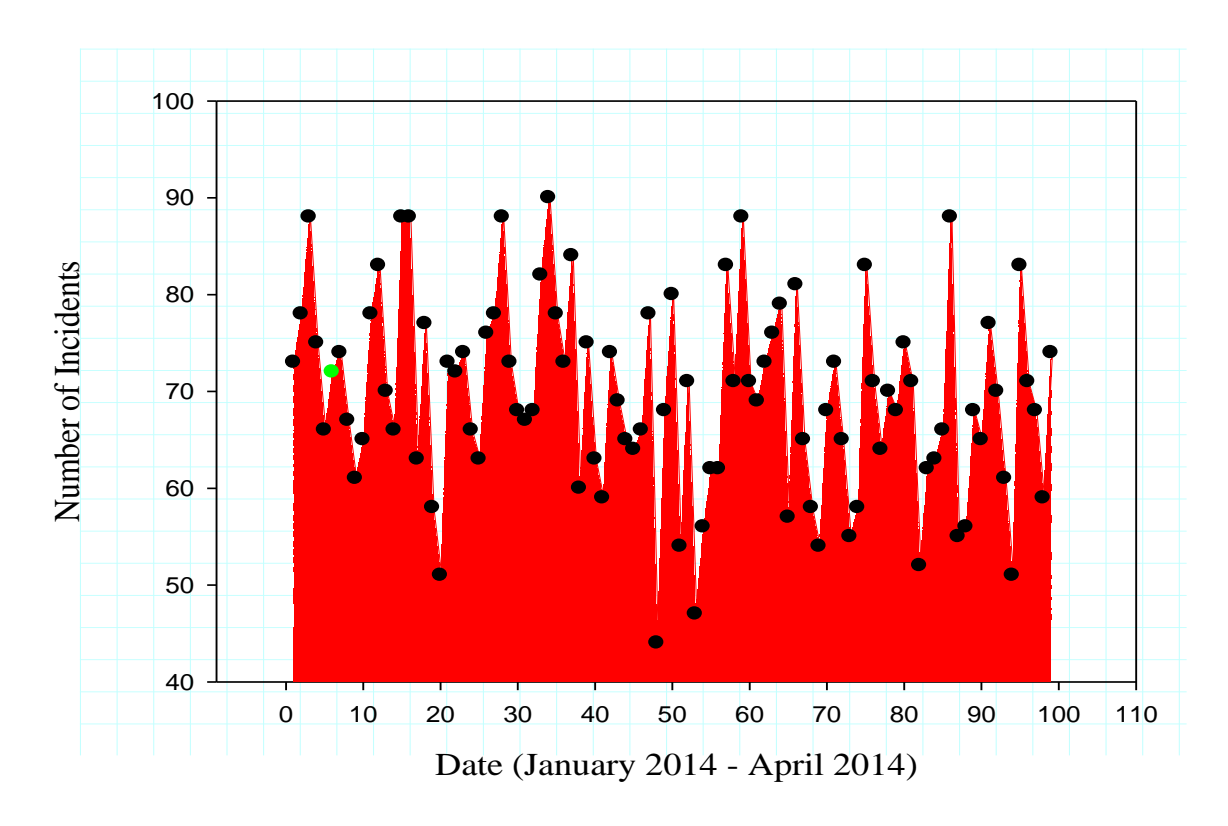


Figure 7.14 Measured SEU incidents in RASAT versus time from January 2014 to April 2014. Green data point represent the SEUs labeled as 'severe'.

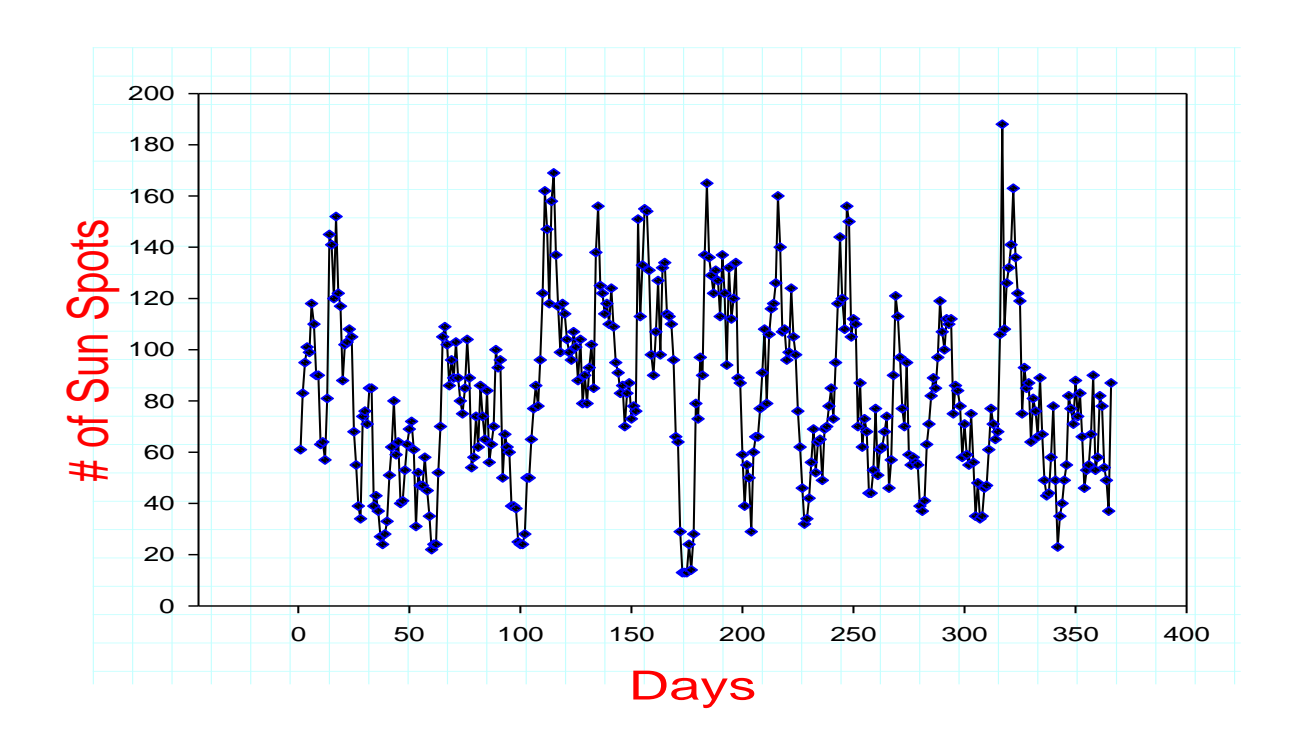


Figure 7.15 Sunspot Numbers vs Days (January 2013- December 2013)

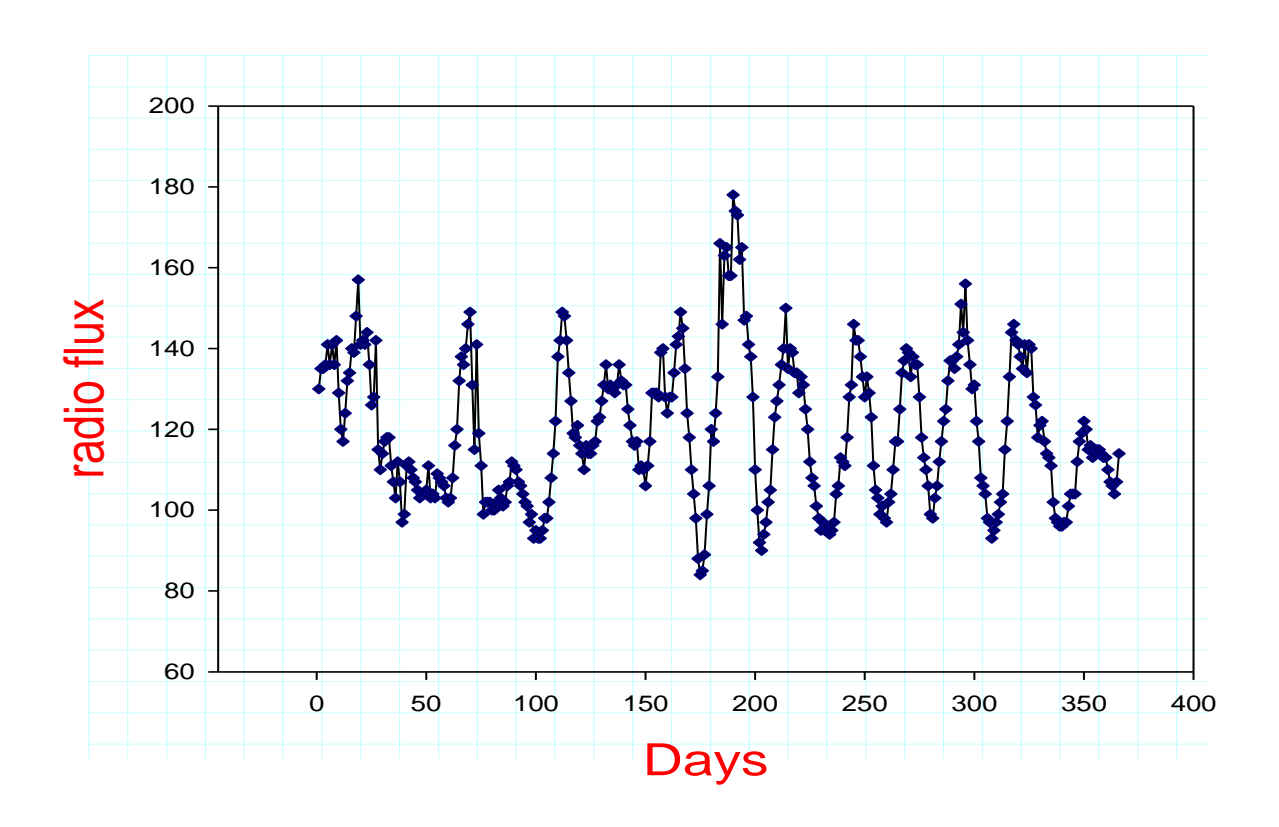


Figure 7.16 Radio Flux vs Days (January 2013- December 2013)

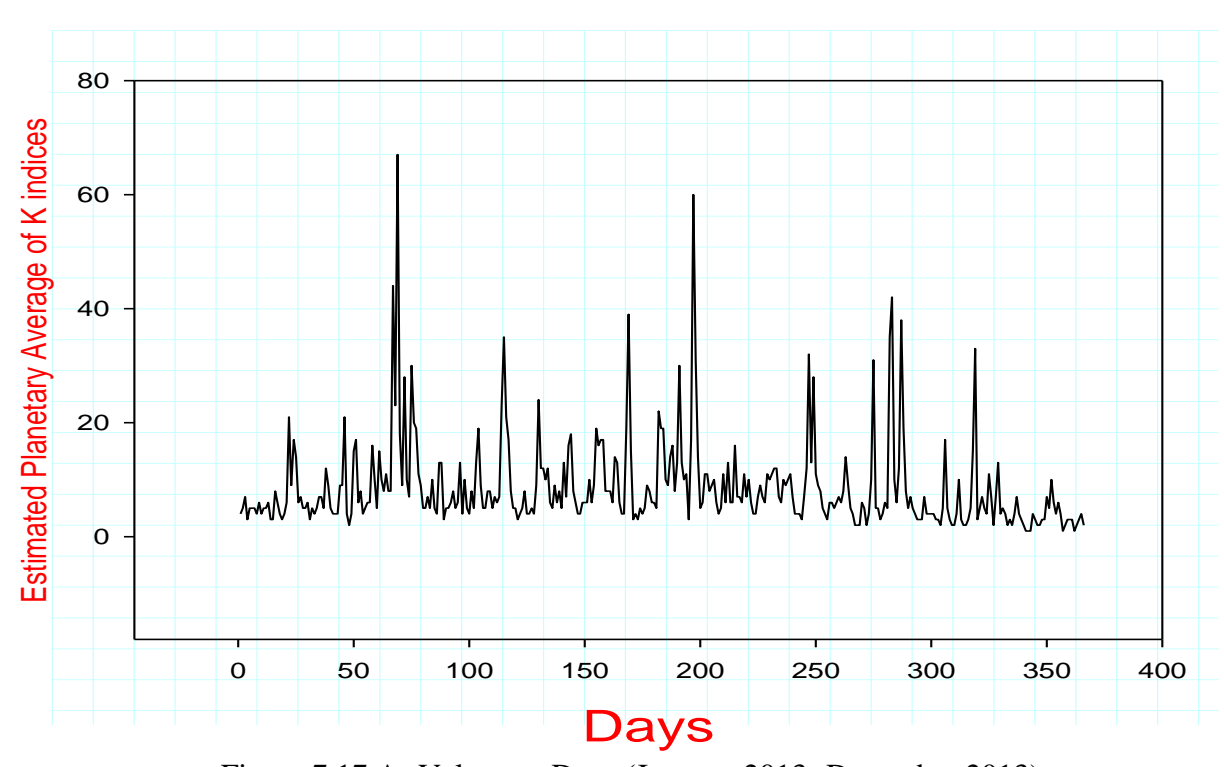


Figure 7.17 A_p Values vs Days (January 2013- December 2013)

7.3.1 June 3rd 2013

RASAT made 58 corrections with severe severity. Solar activity was very low to high during the period. The week began at low levels. A C9 solar flare at 03/0725 UTC. Activity was very low on 04 June. Moderate levels were observed on 05 June when an M1 solar flare was produced at 05/0857 UTC with an associated Type IV radio sweep and a weak CME.

The majority of the ejecta was directed southwest. 06 June saw a return to very low activity. High activity was observed on 07 June when an M5 flare was produced at 07/2249 UTC along with a 160 sfu Tenflare. An associated CME was observed but was determined to be directed west and well south of the ecliptic. Solar activity returned to low levels for the remainder of the period.

No proton events were observed. The greater than 2 MeV electron flux at GEO and LEO was at high levels for the entire period with only short periods dipping below threshold. The peak flux for the week reached 31,800 pfu on 04 June and levels remained high at the time of this report.

Geomagnetic field activity was at mostly quiet levels from 03 - 06 June. Activity increased to unsettled to active levels on 06 June due to effects from a combination of multiple weak transients from 03 June and a co-rotating interaction region (CIR) ahead of a coronal hole high speed stream (CH HSS). Minor to major storm periods were observed on 07 June due to continued effects from the CIR/CH HSS. Activity returned to quiet to unsettled levels on 08 and 09 June as CH HSS stream effects began to subside.

Table 7.26 Radio Flux, Sunspot Numbers, Sunspot Area [58]

	Radio Flux	Sunspot	Sunspot Area
Date	10.7 cm	Numbers	(10 ⁻⁶ hemi.)
2 June	111	76	290
3 June	112	99	160
4 June	110	59	390

Table 7.27 Proton Flux Values [58]

	Proton Flux	Proton Flux	Proton Flux
Date	(protons/cm ² daysr)	(protons/cm ² daysr)	(protons/cm ² daysr)
Range	>1 MeV	>10 MeV	>100 MeV
2 June	1.4e+06	1.0e+04	2.3e+03
3 June	1.7e+06	1.0e+04	2.3e+03
4 June	9.8e+05	1.1e+04	2.4e+03

Table 7.28 Proton, Peak 5-minute-averaged fluxes Values at Spacecraft, Generated by SPENVIS

	Proton Flux	Proton Flux	Proton Flux
Date	(protons/cm ² daysr)	(protons/cm ² daysr)	(protons/cm ² daysr)
Range	>1 MeV	>10 MeV	>100 MeV
2 June	2.064e+04	1.030e+03	2.754e+01
3 June	2.746e+04	1.133e+03	2.725e+01
4 June	2.739e+04	1.130e+03	2.719e+01

Table 7.29 Electron Flux Values [58]

D .	Electron Flux	
Date	(electrons/cm ² day sr)	
Range	>0.6 MeV >2MeV >4 MeV	
2 June	1.3e+08	
3 June	6.4e+08	
4 June	1.4e+08	

Table 7.30 Electron Flux Values at Spacecraft, Generated by SPENVIS

Date	Electron Flux (electrons/cm² day sr)	
Range	>0.6 MeV >2MeV >4 MeV	
2 June	1.3878e+09	
3 June	6.4431e+07	
4 June	1.3167e+10	

7.3.2 July 9th and July 10th 2013

RASAT made 73 and 70 corrections with severe severity respectively on July 10th and July 11th. Solar activity was low. The largest flare of the period was a C9 solar flare at 08/0122 UTC. A C4/1n flare at 10/0643 UTC. A 12-degree filament occurred at 09/1400 UTC resulting in an Earth-directed coronal mass ejection (CME) with an estimated speed of 400 km/s. Another slow-moving CME with a potential Earth-directed component was observed at 12/1824 UTC. The remainder of the week was devoid of potentially geoeffective events.

No proton events were observed.

The greater than 2 MeV electron flux at GEO and LEO reached high levels on 10 - 14 July and was at moderate levels before that. A peak flux value of 22,500 pfu was reported on 12 July at 1850 UTC.

Geomagnetic field activity ranged from quiet to minor geomagnetic storm conditions during the week. An Earth-directed CME which left the Sun on 06 July arrived at the ACE spacecraft at approximately 09/1958 UTC. A 25 nT sudden impulse was subsequently recorded at the Fredericksburg magnetometer at 09/2049 UTC. By 09/2359 UTC, the geomagnetic field had reached active levels, and by 10/0257 UTC, minor (NOAA Scale G1) geomagnetic storm conditions were observed. Minor (G1)

storm conditions prevailed for two periods, after which, active to unsettled conditions were observed. The following day, there was an isolated minor (G1) storm period nestled among otherwise quiet to active conditions. By 12 July, the field had returned to mostly quiet levels when a co-rotating interaction region (CIR) ahead of a small negative polarity coronal hole high speed stream (CH HSS) arrived.

Table 7.31 Radio Flux, Sunspot Numbers, Sunspot Area [58]

Date	Radio Flux 10.7 cm	Sunspot Numbers	Sunspot Area (10 ⁻⁶ hemi.)
8 July	119	143	790
9 July	120	98	720
10 July	118	76	440
11 July	113	85	350

Table 7.32 Proton Flux Values [58]

Date	Proton Flux (protons/cm ² daysr)	Proton Flux (protons/cm ² daysr)	Proton Flux (protons/cm ² daysr)
Range	>1 MeV	>10 MeV	>100 MeV
8 July	1.1e+05	1.0e+04	2.6e+03
9 July	1.6e+05	9.8e+03	2.4e+03
10 July	2.0e+05	9.6e+03	2.3e+03
11 July	5.3e+05	9.6e+03	2.4e+03

Table 7.33 Proton, Peak 5-minute-averaged fluxes Values at Spacecraft, Generated by SPENVIS

	Proton Flux	Proton Flux	Proton Flux
Date	(protons/cm ² daysr)	(protons/cm ² daysr)	(protons/cm ² daysr)
Range	>1 MeV	>10 MeV	>100 MeV
8 July	2.632e+04	1.132e+03	2.761e+01
9 July	2.752e+04	1.135e+03	2.732e+01
10 July	2.746e+04	1.133e+03	2.725e+01
11 July	2.746e+04	1.133e+03	2.725e+01

Table 7.34 Electron Flux Values [58]

Date	Electron Flux (electrons/cm² day sr)	
Range	>0.6 MeV >2MeV >4 MeV	
8 July	9.7e+06	
9 July	1.1e+07	
10 July	3.3e+07	
11 July	1.1e+08	

Table 7.35 Electron Flux Values at Spacecraft, Generated by SPENVIS

	Electron Flux	
Date	(electrons/cm ² day sr)	
Range	>0.6 MeV >2MeV >4 MeV	
8 July	9.7062e+09	
9 July	1.3025e+10	
10 July	3.5569e+09	
11 July	1.0653e+08	

7.3.3 July 25th 2014

RASAT made 78 corrections with severe severity. Solar activity was low. The largest flare of the week was a C3 solar flare at 28/1223 UTC. The remaining regions were generally small and docile in comparison. While a few coronal mass ejections were observed throughout the week, analysis suggested none were Earth-directed.

No proton events were observed at GEO and LEO.

The greater than 2 MeV electron flux at GEO and LEO reached high levels from 22-25 July and again on 27 July. Remarkably, 25 July marked the last day of a 16 day streak of high electron flux levels which began on 10 July.

Geomagnetic field activity was at quiet to unsettled levels throughout most of the week, with the exception of 25-26 July. On those two days, planetary conditions reached active levels with a single period of minor storm conditions at high latitudes. The increased activity came in response to the onset of a recurrent, positive-polarity, coronal hole high speed stream. Quiet to unsettled levels returned on 27 July and lasted through the end of the period.

Table 7.36 Radio Flux, Sunspot Numbers, Sunspot Area [58]

Date	Radio Flux 10.7 cm	Sunspot Numbers	Sunspot Area (10 ⁻⁶ hemi.)
24 July	108	65	320
25 July	107	71	340
26 July	110	58	330

Table 7.37 Proton Flux Values [58]

Date	Proton Flux (protons/cm ² daysr)	Proton Flux (protons/cm² daysr)	Proton Flux (protons/cm ² daysr)
Range	>1 MeV	>10 MeV	>100 MeV
24 July	4.5e+05	1.1e+04	2.8e+03
25 July	6.7e+05	1.1e+04	2.7e+03
26 July	1.5e+05	1.1e+04	2.6e+03

Table 7.38 Proton, Peak 5-minute-averaged fluxes Values at Spacecraft, Generated by SPENVIS

	Proton Flux	Proton Flux	Proton Flux
Date	(protons/cm ² daysr)	(protons/cm ² daysr)	(protons/cm ² daysr)
Range	>1 MeV	>10 MeV	>100 MeV
24 July	2.824e+04	1.052e+03	2.674e+01
25 July	2.786e+04	1.149e+03	2.766e+01
26 July	2.786e+04	1.149e+03	2.766e+01

Table 7.39 Electron Flux Values [58]

Date	Electron Flux (electrons/cm² day sr)	
Range	>0.6 MeV >2MeV >4 MeV	
24 July	8.7e+07	
25 July	7.3e+07	
26 July	8.8e+06	

Table 7.40 Electron Flux Values at Spacecraft, Generated by SPENVIS

Date	Electron Flux (electrons/cm² day sr)	
Range	>0.6 MeV >2MeV >4 MeV	
24 July	4.0528e+09	
25 July	5.5420e+09	
26 July	4.0628e+10	

7.3.4 August 8th 2014

RASAT made 79 corrections with severe severity. Solar activity was at low levels. The week began at very low levels a C2 solar flare was produced at 09/2028 UTC. Activity was at low levels the remainder of the period. The largest event was a C8 solar flare at 11/2155 UTC. Multiple disappearing filaments (DSFs) were observed during the period but none of them resulted in geomagnetic activity.

No proton events were observed at GEO and LEO.

The greater than 2 MeV electron flux at GEO and LEO was at high levels from 05 - 10 Aug and decreased to normal to moderate levels on 11 Aug.

Geomagnetic field activity was at active to minor storm levels on 05 Aug due to coronal hole high speed stream (CH HSS) effects. Mostly quiet conditions prevailed from 06 - 08 Aug as CH HSS effects subsided. Quiet to unsettled conditions were observed on 09 Aug due to a second CH HSS followed by a return to mostly quiet conditions from 10 - 11 Aug as effects waned.

Table 7.41 Radio Flux, Sunspot Numbers, Sunspot Area [58]

Date	Radio Flux 10.7 cm	Sunspot Numbers	Sunspot Area (10 ⁻⁶ hemi.)
7 August	106	99	190
8 August	104	90	190
9 August	104	51	130

Table 7.42 Proton Flux Values [58]

	Proton Flux	Proton Flux	Proton Flux
Date	(protons/cm ² daysr)	(protons/cm ² daysr)	(protons/cm ² daysr)
Range	>1 MeV	>10 MeV	>100 MeV
7 August	1.4e+05	9.9e+03	2.6e+03
8 August	1.5e+05	1.0e+04	2.4e+03
9 August	3.7e+05	1.0e+03	2.5e+03

Table 7.43 Proton, Peak 5-minute-averaged fluxes Values at Spacecraft, Generated by SPENVIS

Date	Proton Flux (protons/cm ² daysr)	Proton Flux (protons/cm ² daysr)	Proton Flux (protons/cm ² daysr)
	(protons, our dujor)	(protons, our dujor)	(protons, em aujor)
Range	>1 MeV	>10 MeV	>100 MeV
7 August	5.5e+04	1.1e+03	2.5e+01
8 August	8.1e+04	1.0e+03	2.6e+01
9 August	9.1e+04	1.1e+03	2.5e+01

Table 7.44 Electron Flux Values [58]

Date	Electron Flux (electrons/cm² day sr)	
Range	>0.6 MeV >2MeV >4 MeV	
7 August	4.2e+08	
8 August	3.1e+08	
9 August	1.3e+08	

Table 7.45 Electron Flux Values at Spacecraft, Generated by SPENVIS

Date	Electron Flux (electrons/cm² day sr)	
Range	>0.6 MeV >2MeV >4 MeV	
7 August	3.6e+09	
8 August	4.6e+08	
9 August	3.3e+09	

7.3.5 October 11th 2013

Rasat made 83 corrections with severe severity. The week began at low, then very low levels of solar activity. Moderate levels followed on 09 October when an M2 flare was produced at 09/0148 UTC with no corresponding optical flare reported. This event was associated with weak Type II (estimated speed 791 km/s) and Type IV radio sweeps.

By 11 October, a coronal mass ejection was observed at 11/0724 UTC. Another CME was observed at 11/1400 UTC. This event was associated with a C6 flare that occurred at 11/1228 UTC, and was expected to imact Earth later early on the 15th.

After a brief respite, solar activity again reached moderate levels when an isolated M1 solar flare was produced at 13/0043 UTC which was accompanied by a Type II radio emission at 11/0035 UTC (estimated speed 798 km/s).

No proton events were observed at GEO and LEO.

The greater than 2 MeV electron flux at GEO and LEO reached high levels on 12 October at 1520 UTC. For the remainder of the week the flux was at low to moderate levels.

Geomagnetic field activity reached minor storm levels during the week. The period began with a weak CME passage at approximately 07/0035 UTC with minor increases

in IMF Bt, speed, and density; associated with the CME observed on October 3rd. Solar wind speed remained low in the 269 to 341 km/s range. IMF Bt ranged from 4 to 7 nT. IMF Bz was weakly southward during most of the period with a range of 3 to -6 nT. The geomagnetic field was at quiet levels until around 08/2023 UTC, then rapidly increased to minor storm levels by 08/2024 UTC. The activity increased following a geomagnetic sudden impulse (SI) at 08/1941 UTC.

By 09 October, solar wind speed increased to a high of 683 km/s at 09/0311 UTC following the shock arrival, then gradually decreased to a low of 445 km/s at 09/2316 UTC. IMF Bt was elevated through the period with a peak of 14 nT observed at 09/0900 UTC. IMF Bz was weakly southward during the first half of the period, then became weakly northward during the rest of the day with a range of 7 to -5 nT. The geomagnetic field was at active to minor storm levels during the first half of the period, then decreased to unsettled levels after 09/1200 UTC. The following day, an isolated active period was observed during 10/0000-0300 UTC as the effects of the CME diminished. Quiet conditions returned on the 11th and remained through the end of the week.

Table 7.46 Radio Flux, Sunspot Numbers, Sunspot Area [58]

Date	Radio Flux 10.7 cm	Sunspot Numbers	Sunspot Area (10 ⁻⁶ hemi.)
10 October	121	138	670
11 October	129	115	780
12 October	128	106	760

Table 7.47 Proton Flux Values [58]

Date	Proton Flux (protons/cm² daysr)	Proton Flux (protons/cm² daysr)	Proton Flux (protons/cm ² daysr)
Range	>1 MeV	>10 MeV	>100 MeV
10 October	1.2e+05	9.8e+03	2.4e+03
11 October	1.2e+05	1.1e+04	2.9e+03
12 October	2.7e+05	1.4e+04	3.7e+03

Table 7.48 Proton, Peak 5-minute-averaged fluxes Values at Spacecraft, Generated by SPENVIS

Date	Proton Flux (protons/cm ² daysr)	Proton Flux (protons/cm² daysr)	Proton Flux (protons/cm² daysr)
Range	>1 MeV	>10 MeV	>100 MeV
10 October	2.796e+04	1.153e+03	2.776e+01
11 October	2.783e+04	1.148e+03	2.762e+01
12 October	2.769e+04	1.142e+03	2.749e+01

Table 7.49 Electron Flux Values [58]

Date	Electron Flux (electrons/cm² day sr)	
Range	>0.6 MeV >2MeV >4 MeV	
10 October	3.8e+06	
11 October	1.7e+07	
12 October	3.9e+07	

Table 7.50 Electron Flux Values at Spacecraft, Generated by SPENVIS

Date	Electron Flux (electrons/cm² day sr)	
Range	>0.6 MeV >2MeV >4 MeV	
10 October	2.7760e+08	
11 October	1.0564e+08	
12 October	3.5200e+09	

7.3.6 January 8th 2014

Rasat made 72 corrections with severe severity. Solar activity ranged from low to high levels during the period. Low levels were observed on 06 January and again from 09-12 January with the majority of the solar flare activity. High levels were reached on 07 January due to an M1/1n flare at 07/0353 UTC, and an M7/2b flare at 07/1013 UTC with an associated Tenflare radio burst (409 sfu), and an X1/2n at 07/1832 UTC. The X1 flare was associated with a Type II radio sweep (1064 km/s), a 8300 sfu Tenflare, and a partial halo CME with an approximate speed ranging from 1800 km/s to 2100 km/s.

Model output of the CME indicated an Earth-directed component; however the impact on the geomagnetic field was significantly less than By 08 January, solar activity decreased to moderate levels due to an isolated M3/Sf flare at 08/0347 UTC. The M3 flare was accompanied by a Type II radio sweep (697 km/s) and a non-Earth directed CME.

By 09 January and through the rest of the reporting period the sunspot group was in a slow decay phase. The period began with the greater than 10 MeV proton flux recovering from last weeks enhancement likely associated with an M4 flare on 04 January. At 06/0820 UTC, both the greater than 10 MeV and 100 MeV proton flux levels began to rise in response to flare activity which rotated off the visible disk on 04 January. The greater than 10 MeV protons crossed the 10 pfu (S1 Minor) threshold at 06/0915 UTC and reached a maximum of 42 pfu at 06/1600 UTC before slowly declining to 10.1 pfu by 07/1930 UTC. The greater than 100 MeV protons crossed the 1 pfu threshold at 06/0830 UTC and reached a maximum of 4 pfu at 06/1005 UTC. The event ended at 06/1710 UTC. The greater than 100 MeV proton event associated with the X-flare reached the 1 pfu threshold at 07/2030 UTC, reached a maximum of 4 pfu at 07/2240 UTC, and ended at 08/1225 UTC.

Solar wind speed increased from approximately 350 km/s to 435 km/s with the total field increasing from 3 nT to 7 nT at 07/1428 UTC. This small shock and CME resulted in several periods of unsettled levels late on 07 January through early on 08 January. Quiet to unsettled levels continued through 09 January. Late on 09 January, the An isolated unsettled period wasobserved late on 09 January as a result of CME activity. Nominal solar wind condition continued through late on 12 January with mostly quiet

conditions observed. By late on 12 January, a negative polarity coronal hole high speed stream began to impact the geomagnetic field. Solar wind speeds increased from approximately 480 km/s to near 680 km/s by the end of the period. The geomagnetic field responded with unsettled to active levels by late on 12 January.

Table 7.51 Radio Flux, Sunspot Numbers, Sunspot Area [58]

	Radio Flux	Sunspot	Sunspot Area
Date	10.7 cm	Numbers	(10 ⁻⁶ hemi.)
7 January	237	196	1850
8 January	195	178	1990
9 January	184	106	1960

Table 7.52 Proton Flux Values [58]

Date	Proton Flux (protons/cm ² daysr)	Proton Flux (protons/cm ² daysr)	Proton Flux (protons/cm ² daysr)
	(protons, our duyer)	(protons, our dujer)	(protons, our duyer)
Range	>1 MeV	>10 MeV	>100 MeV
7 January	2.1e+07	2.6e+06	6.1e+04
8 January	1.4e+08	6.9e+07	1.2e+05
9 January	3.7e+08	4.0e+07	9.2e+03

Table 7.53 Proton, Peak 5-minute-averaged fluxes Values at Spacecraft, Generated by SPENVIS

Date	Proton Flux (protons/cm² daysr)	Proton Flux (protons/cm² daysr)	Proton Flux (protons/cm² daysr)
Range	>1 MeV	>10 MeV	>100 MeV
10 October	2.759e+04	1.138e+03	2.739e+01
11 October	2.759e+04	1.138e+03	2.739e+01
12 October	2.766e+04	1.141e+03	2.745e+01

Table 7.54 Electron Flux Values [58]

	Electron Flux	
Date	(electrons/cm ² day sr)	
Range	>0.6 MeV >2MeV >4 MeV	
7 January	4.1e+07	
8 January	1.7e+07	
9 January	9.9e+07	

Table 7.55 Electron Flux Values at Spacecraft, Generated by SPENVIS

Date	Electron Flux (electrons/cm² day sr)	
Range	>0.6 MeV >2MeV >4 MeV	
10 October	2.2952e+10	
11 October	1.0731e+08	
12 October	9.0345e+10	

CHAPTER 8

RESULTS & DISCUSSION

Various aspects of space weather can cause on-orbit satellite anomalies and also can affect ground based systems. Many studies have shown that electrostatic discharges, and single event upsets are the most common anomaly producing mechanisms in space systems. The flux values of space environment particles change from orbit to orbit, due to that fact, one may expect to see anomaly variation among satellites which are on different orbits. Yet it is clear when a GEO satellite have a malfunction after a huge CME or a Solar Flare, a LEO satellite may be effected with the same type of that anomaly.

Impact of space radiation is divided into two principal parts. First is cumulative effect. Energy particles that are cumulated on satellite create an electric field, which after a time damages the circuits on satellite. Second is single event effect. A high energy particle directly interacts with an electronic component on satellite. Sometimes this interaction is permanent, creating single event latch-up or burnout. If there are plenty permanent effects, satellite breaks down and stops working but this may take years. The data logs of Turkish remote sensing satellite of RASAT which were investigated were covering all but SEU events. Although SEUs change the data in micro-electronic device, it is not beyond repair unlike burnouts or latch-ups. While some other satellites orbiting were commanded to shield up against possible intense space weather, and had lost some data on particular dates, RASAT had managed to correct the anomaly mistakes. And again on some quiet days RASAT had shown severe corrections while other satellites orbiting the Earth had shown no anomalies. Even though the SEUs

effects are accepted as short term anomalies, RASAT corrections vs no storm dates arouse a suspicion on total dose effect creating particles. GCRs are known for SEUs (Lanford, 1979), and even though GCRs seem to be responsable for these severe corrections, these anomalies were happened during the solar maxima.

It is been known that the high-energy protons in the inner radiation belt are expected be the principal factor governing SEU events for LEO satellites that encounter them several times a day. High density memory structures in particular, like SRAMs, exhibit low threshold Linear Energy Transfers (LET) to protons. The particle population is affected by the solar cycle and events such as flares. The number of trapped protons decreases during solar maximum and increases during solar minimum. Flares can inject additional protons in the belt, and can sometimes even lead to the formation of additional belts thereby increasing the probability of SEU events. This indicate the responsible particles are may be originating from the radiation belts or solar flares. In fact on the exact dates of the anomalies, there had been a few solar flares yet they were insignificant. If solar events can produce enough heavy ions they can create a nuclear reaction on satellites. If they do elastic collisions with the devices energy is transferred to a recoil Si nucleus, and if they do spallation, target nucleus divide into lighter particles and a heavy nuclei ion. This may create a non-direct SEU event as well. In case of spallation, the angle of incidence of the original particle also need to be considered, as the charge deposition is higher at certain angles.

A particular region of interest for LEOs is the South Atlantic Anomaly (SAA). This region is located off the coast of Brazil at an altitude of approximately 500 km and consists of intense concentrations of protons from the inner belt. Its existence at that particular location arises due to the earth's magnetic field being offset from its center. This results in the geomagnetic field strength being weakest in that region, allowing particles from the inner belt to extend lower into the atmosphere. While other satellites weren't having any troubles, RASAT was making corrections against severe mistakes on its rams. Even though RASAT location was unknown when the corrections were made it is possible that RASAT was in the SAA region.

With other assumptions, informations and notions it is safety to say;

- ❖ There is a correlation between observed events and spacecraft anomalies, but it is not clear and precise. Experiences with past major anomalies, lost capacities and on-station failures are linked to space weather as a possible cause but lacks direct correlations with specific alerts based on anomaly investigations conducted by satellite manufactures and independent consultants.
- ❖ Solar spots vs the anomalies RASAT were investigated. There isn't a clear correlation between those. It's been known that the solar maxima and solar minima effects the number of solar spots. It is expected to see an increment during solar maximums and decrement during solar minimums. In the light of the recent researches it is clear to say, formations due to the magnetic fields of solar spots on the Sun designate solar flare events. The regions of the solar spots gain importance. Since the number of solar flares goes up during solar maximums, one can assume to encounter more satellite anomalies in this period.
- ❖ Solar Radio Flux vs the anomalies of RASAT were investigated. It is an excellent indicator for identifying the actions of solar spots. If one wants to predict major solar events it must be taken account of. Low values indicate that the maximum useable frequency will be low and overall conditions will not be very good, particularly on the higher HF bands. Conversely, high values generally indicate there is sufficient ionization to support long-distance communication at higher- than-normal frequencies. On the dates of anomalies of RASAT, there are numerous radio emissions which vary from type I to type IV. Yet it isn't clear to pinpoint if these radiation emissions are the real cause behind these anomalies.
- ❖ Expected events are not observed when there are severe storm warnings. Most anomalies did not coincide with timing of published major storm events. This may be related to incoming particles's incidence angle and the satellite position. Apart from the date July 12th 2012, there wasn't a great disturbance on Earth's magnetosphere. All of the anomalies of RASAT may have been related to energetic proton events. Since proton events are due to solar flares and coronal mass ejections, direct hit of these events are highly likely to be responsible for anomalies of RASAT. The secondary effects of these events can create

- geomagnetic disturbances. After hitting Earth's magnetosphere these disturbances can create sub-storms and sometimes they turn into a great geomagnetic storms. The anomalies of RASAT took place before these kind of storms. This indicates that solar flares and CMEs create proton events and hit RASAT before hitting the Earth's magnetosphere.
- There are no standard protocols for responding to space weather amongs the literature, and it is hard to access the data of other satellites orbitting the Earth or the satellites working no more. There are multiple smaller databases, but it is clear that they are not enough. A single,centralized database could offer adventages over multiple smaller databases. The development of a centralized satellite anomaly database that would be useful to the broad satellite community is hindered by concerns about sharing proprietary information, as well as the lack of available resources to develop and maintain such a database. Concerns over sharing of proprietary information are perhaps themost significant obstacle for companies in the commercial sector. The lack of resources for development and maintenance is a problem in the civil or defense sector of government, which would likely include organizations that could serve as trusted third parties, and for those that could develop encryption technologies that could obviate the need for a trusted third party.
- ❖ There is no radiation sensor on Turkish Remote Sensing Satellite of RASAT which makes it harder for future investigations. The future project satellites must have a radiation sensor in order to have easy access to space weather information focused on the next generation spacecrafts.
- ❖ Automated 'satellite as a sensor' methods for identifying and cataloging anomalies may significantly reduce the workload of those investigating satellite anomalies. Such systems can enhance both cataloging and categorization efforts and improve space situational awareness. They can also be used as an alternative to data sharing to help diagnose anomalies from the telemetry of a single satellite.
- Current space weather models such as SPENVIS are insufficient to estimate contributing factors qualitatively. The physics of space radiation environment is not fully understood. Consequently, It contains severe simplifications and assumptions which introduces systematic and unknown errors, uncertainties,

poor sampling and resolution. The SPENVIS data set covers only about 4 solar cycles. One can question whether this cycles are representative enough. Data set also includes multiple coverage of some regions and undersampling of some other region. New and better models must be developed.

Space physics are relatively a new field, and it is a must to be conquered by the mankind. Since the first situ measurements in 1950 by Van Allen, launched the first rockets, the rate of the developments have been increasing with an enourmous speed. The modern society and scientists have begun to understand how important the space weather is. Because of the increasing reliance on technologies susceptiple to space weather environment, the forecasting and mitigation systems must have a parallel development with the escalating using rate of satellites and spacecrafts in order to respond catasthrophic events before take place. This study may be a future reference for those who will design and engineer the next generation spacecrafts and satellites.

- [1] Nature Group Publishing, Nature Publishing and Institute of Physics Publishing., (2001). Encyclopedia of Astronomy and Astrophysics, 4654, 785998.
- [2] Trümper, J.E. and Hasinger G., (2006). "The Universe in X-rays".
- [3] Chaisson, E. and McMillan S., (1993). Astronomy Today, New Jersey: Prentice Hall.
- [4] Metcalfe, T., Layers of the Sun:
 http://windows2universe.org/sun/Solar_interior/Sun_Layers/Convection_zone/convection_zone.html, 15 January 2014.
- [5] Jennings, H., Mechanism of the Sun:
 http://Solar_heliospheric.engin.umich.edu/hjenning/convectionZone.html, 10
 June 2014.
- [6] NASA, Layers of the Sun: https://nasa.gov/images/content/179925main_heliolayers_label_516.jpg, 12 March, 2014
- [7] Center for Science and Engineering, Layers of the Sun: http://csep10.phys.utk.edu/astr162/lect/sun/chromosphere.html, 13 March, 2014
- [8] Freedman, R.A. and William, J., (2008). Universe, New York, USA.
- [9] Lorrain, P. and Kouthchmy, S., (1996). "Two Dynamical Models for Solar Spicules", Solar Physics 165(1):115-137.
- [10] Falconer, D.A., Davila, J.M., and Thomas, R.J., "Relative Elemental Abundance of the Quiet Solar Corona Determined by SERTS", ApJ 482, 1004.
- [11] Gibson, E.G., (1973). "The Quiet Sun", National Aeronautics and Space Administration, Washington, DC.
- [12] Center for Science and Engineering, Layers of the Sun: http://csep10.phys.utk.edu/astr162/lect/sun/, 4May, 2014
- [13] Lund Observatory: http://www.astro.lu.se/Education/utb/ASTA21/pdf/Solar_Wind.pdf, 5 May, 2014
- [14] Kivelson, M. and Russell, C., (1995). Introduction to Space Physics, 62, First Edition, Cambridge University Press, Australia.

- [15] Wikipedia, Magnetosphere:
 http://en.wikipedia.org/wiki/Magnetosphere#mediaviewer/File:Magnetosphere
 rendition.jpg, 15 May, 2014
- [16] Hewish, A., (1971). "The Spectrum of Plasma-Density Irregularities in the Solar Wind", The Astrophysical Journal, 163:645.
- [17] Parker, E.N., (1958). "Interaction of the Solar Wind with the Geomagnetic Field", Physics Fluids 171(1)
- [18] Li, H.W., Pallavicini, R. and Cheng, C.C., (1987). "Analysis of Ultraviolet and X-ray Observations of Three Homologous Solar Flares from SMM", Solar Physics Journal 107:271-282.
- [19] Hudson, H.S., (1991). "Solar Physics", Solar Physics Journal, vol 133(2):357-369.
- [20] Space Weather Live, Classification of Solar Flares:
 http://www.spaceweatherlive.com/en/help/the-classification-of-solar-flares, 12
 June, 2014
- [21] Crooker, N., Joselyn, J. A. and Feynman, J., (1997). "Coronal Mass Ejections", Geophysical Monograph Series, 99, American Geophysical Union.
- [22] Hundhausen, A. J. (1988). "The Origin and Propagation of Coronal Mass Ejections", Proc. 6th Int. Solar Wind Conference, Boulder, CO: National Center for Atmospheric Research, 187-214.
- [23] Forbes, T.G., Chen, J., Cid, C., Kotas, J., Lee, M.A., Mann, G., Miki, Z., Potgieter, M.S., Schmidt, J.M., Siscoe, G.L., Vainio, R., Antiochos, S.K. and Riley, P., (2006). "CME Theory and Models".
- [24] Gosling, J.T., McRomas, D.J., Philips, J.L. and Barne, S.J., (1991). "Geomagnetic Activity Associated with Earth Passage of Interplanetary Shock Disturbances and Coronal Mass Ejections", Geophysics Journal, 96:7831-7839
- [25] McIntosh, P.S., (1981). "The Physics of Sunspots", NOAA Space Environment Lab., Boulder, CO.
- [26] Bray, R.J. and Laughhead, R.E., (1964). Sunspots, New York, Wiley.
- [27] NASA, Sunspots: httpp://starchild.gsfc.nasa.gov, 10 June, 2014
- [28] Rice University, Sun Spots: https://galileo.rice.edu/sci/observations/Sunspot_drawings.html, 11 May, 2014
- [29] Nature Group Publishing, Nature Publishing and Institute of Physics Publishing (2001). Encyclopedia of Astronomy and Astrophysics, 4678.
- [30] Kivelson, M. and Russell, C. (1995). Introduction to Space Physics, 70.
- [31] Thomas J.H. and Weiss N., (1992). "Sunspots: Theory and Observations", NATO ASI series, 375.

- [32] Miteva, R., Klein, K.L., Malandraki, O. and Dorrlan, G. (2013). "Solar Energetic Particle Events in the 23rd Solar Cycle: Interplanetary Magnetic Field Configuration and Statistical Relationship with Flares and CMEs", Solar Physics, 282(2):579-613.
- [33] Reames, D.V., Tylka, A.J., Chee, K.Ng., (2001). "Solar Energetic Particles and Space Weather", Goddard Space Flight Center.
- [34] CALTECH, The Space Environment: http://srl.caltech.edu/ACE/CRIS_SIS/scitech.html, 11 May, 2014
- [35] Solar Physics, Solar Energetic Particles: http://solarphysics.livingreviews.org/open?pubNo=lrsp-2006-2&page=articlesu15.html, 11 May, 2014
- [36] Sollitt, L., (2004). "Ionic Charge States of Solar Energetic Particles", California Institute of Technology.
- [37] Reames, D.V., (2002). "Solar Energetic Particle Variations", Cospar D2.3-E3.3-003202.
- [38] Baker, D.N. (2000). "The Occurrence of Operational Anomalies in Spacecraft and Their relationship to Space Weather", IEEE, Transactions on Plasma Science, vol 28(6):2007-2016.
- [39] Space Weather at UMA, Forecasting Solar Energetic Protons: http://spaceweather.uma.es/solarstorms.html, 15 May, 2014
- [40] Lohmeyer, O.W., Cahoy, K. and Liu, S., (2013). "Casual Relationship Between Solar Proton Events and Single Upsets for Communication Satellites", IEEE Aerospace Conference, Big Sky, Montana.
- [41] Nunez, M., (2011). "Predicting Solar Energetic Proton Event", Space Weather, 9, S07003.
- [42] Newkirk, G.A., (1973). "Coronal Disturbances", International Astronomical Union Symposium no 57.
- [43] Lin, R.P., (1973). "Non-Relativistic Solar Electrons", Space Science Reviews, vol 16(1-2):189-256.
- [44] Hamish, A.S., Reid and Kontar P.E., (2012). "Evolution of the Solar Flare Energetic Electrons in the Homogeneous Inner Heliosphere"
- [45] Martin, A.R., (1994). "A review of spacecraft/plasma interactions and effects on space systems", Journal of The British Interplanetary Society, 47(4):134-142.
- [46] Ramatry, R. and Murphy, R.J., (1987). "Nuclear Processes and Accelerated Particles in Solar Flares", Space Science Review, 45:213-268.
- [47] Baker, D.N., Blake, J.B., Klebesadel, R.W. and Higbie, P.R., (1986). "Highly Relativistic Electrons in the Earth's Outer Magnetosphere, Lifetimes and Temporal History", J. Geophysics, 198, 914265.
- [48] Simnett, G.M., (1972). "Relativistic Electrons from the Sun Observed by IMP-4".
- [49] Liehmon, M.W. and Chan A.A., (2007). "Unraveling the Causes of Radiation Belt Enhancements", Eos, 88(42):425.

- [50] Irwin, J.A., (1954). Astrophysics Decoding the Cosmos, Wiley, 112-114.
- [51] Khazanov, C.V., Liehmon, M.W., Fol, M.C., Newman, T.S., and Ridley, A.J., (2004). "Stormtime Particle Energization with AMIE Potentials", J. Geophysics Res.
- [52] Red Orbit, Van Allen Radiation Belt:
 http://www.redorbit.com/education/reference_library/space_1/solar_system/25
 74610/van_allen_radiation_belt/, 12 April, 2014
- [53] Stern, D.P. and Mauricio P., (2013). "The exploration of the Earth's Magnetosphere", Recollections of Space Research, Mexico, Anahuac.
- [54] Pines, A. And Dilao, R., (2007). "Chaos in the Stürmer Problem, Progress in Non-linear Differential Equations and Their Applications".
- [55] Narte News (1999). "The Effect of 10.7 cm Solar Radiation on 2.4 GHZ Digital Spread Spectrum Communications", Narte, 17(3).
- [56] Government of Canada, The History of the 10.7 cm Solar Flux: http://www.spaceweather.gc.ca/solarflux/sx-2-eng.php, 14 April, 2014
- [57] Bartels, J., Heck, N. H., Johnston, H. F., (1939). "The Three-Hour Range Index Measuring Geomagnetic Activity", Geophysics Res., 44:411-454.
- [58] NOAA Space Weather Prediction Center
- [59] Poole, I., (2002). "Understanding Solar Indices".
- [60] Southwest Research Institute, Dst Index: http://pluto.space.swri.edu/image/glossary/dst.html, 14 April, 2014
- [61] Lesf Center, Dst Index: http://lesf.org/research, 14 April, 2014
- [62] Kivelson, M. and Russell, C., (1995). "Introduction to Space Physics", 400.
- [63] Wikipedia, Geomagnetic Storm: http://en.wikipedia.org/wiki/Geomagnetic_storm, 14 April, 2014
- [64] Southwest Research Institute, Dst Index:
 http://pluto.space.swri.edu/image/glossary/geomagnetic_storm.html, 29 May, 2014
- [65] Solomon, S., Garcia, R.R. and Reid, G.C., (1991). "Response of the Middle Atmosphereto the Solar Proton Events of August-December 1989", Geophysics Res. Lett., 18:1019.
- [66] Space Weather Live, Radio Blackouts: http://spaceweatherlive.com/en/help/what-are-radio-blackouts, 29 May, 2014
- [67] Austrian Research Centre, Seibersdorf
- [68] Leach, R.D., Alexander, M.B., (1995). "Failures and Anomalies Attributed to Spacecraft Charging".
- [69] Arizona State University, Spacecraft Charging: http://holbert.faculty.asu.edu/eee560/spc-chrg.html, 29 May, 2014
- [70] Grard, R., Knott, K. and Pederson P., (1983). "Spacecraft Charging Effects", Science Reviews, 34:289-304

- [71] Leung, P. and Robinson, P.A., (1986). "Environment Induced Electrostatic Discharges as the Cause of Voyager 1 Power-on-Resets", Journal of Spacecraft and Rockets, 23(3):323-330.
- [72] Australian Government Bureau of Meteorology, Ionospheric Scintillation: http://www.ips.gov.au/Satellite/6/3, 29 May, 2014
- [73] Dyer, C. and Rodgers, D,. (1998). "Effects on Spacecraft and Aircraft electronics".
- [74] National Defense Research Institute (2014). "Benefits of a Centralized Anomaly Database and Methods for Securely Sharing Information Among Satellite Operators".
- [75] Yapici, T., (2007). Influences of Interplanetary Magnetic Field on the Variability of the Aerospace Media, Thesis, Metu.
- [76] ESA Space Environment, Space Environment Information System: http://tecees.esa.int/R_and_D/spenvis.html, 29 May, 2014
- [77] TUBITAK Uzay, RASAT: http://uzay.tubitak.gov.tr/, 14 June, 2014
- [78] Vargun, B., Seve, R., Okcan, B., Karakus, K., Kapucu, K. And Oktem R. (2011). "GEZGIN", RAST Conference, IEEE, 944-949.

CURRICULUM VITAE

PERSONAL INFORMATION

Name Surname : Mehmet KAPLAN

Date of birth and place : 02/07/1985

Foreign Languages : English

E-mail : barbarosmehmekaplan@gmail.com

EDUCATION

Degree	Department	University	Date of Graduation
Master	Physics	Yildiz Technical	Expected on
		University	August,2014
Undergraduate	Physics	Yildiz Technical University	August, 2011
High School	Pure Science Module	Vatan Anadolu Lisesi	June, 2003

PUBLISHMENTS

Conference Papers

- 1. Kaplan Mehmet, Hudaverdi Murat, "The Correlations of Space Weather and Satellite Anomalies:RASAT-extended abstract", International Conference on Recent Advances in Space Technologies (2013).
- 2. Kaplan Mehmet, Hudaverdi Murat, "The Correlations of Space Weather and Satellite Anomalies:RASAT-proceeding", International Conference on Recent Advances in Space Technologies (2013).
- 3. Kaplan Mehmet, Hudaverdi Murat, "The Correlations of Space Weather and Satellite Anomalies:RASAT-proceeding", Cospar, China (2013).

Projects

1. Tubitak Student Fellowship 2013 – I was awarded for_Tubitak 1001 Project: Galaxy Clusters, Cluster Evolutions and Supernova Remnants

AWARDS

- 1. Tubitak Student Fellowship 2013 I was awarded for_Tubitak 1001 Project: Galaxy Clusters, Cluster Evolutions and Supernova Remnants
- 2. BAP Fellowship (Scientific Research Project) Yildiz Technical University 2013, I was awarded for Master of Science Thesis.